

**Ultrafast Electronic Deactivation Dynamics
in DNA Model Systems
by Femtosecond UV Fluorescence Spectroscopy**

Dissertation
zur Erlangung des Doktorgrades
der Mathematisch-Naturwissenschaftlichen Fakultät
der Christian-Albrechts-Universität Kiel

vorgelegt von
Dipl.-Chem. Nina K. Schwalb
aus Steinfurt

Institut für Physikalische Chemie
der Christian-Albrechts-Universität zu Kiel

Kiel, im Mai 2009

Referent: Prof. Dr. F. Temps
Koreferent: Prof. Dr. J. Grotemeyer

Tag der mündlichen Prüfung: 22. Juni 2009
Zum Druck genehmigt: 22. Juni 2009

gez. Prof. Dr. L. Kipp, Dekan

Hiermit erkläre ich an Eides Statt, dass die vorliegende Abhandlung - abgesehen von der Beratung durch meinen Betreuer Herrn Prof. Dr. F. Temps - nach Inhalt und Form meine eigene Arbeit ist.

Diese Arbeit hat weder in Auszügen noch in ganzer Form einer anderen Stelle im Rahmen eines Prüfungsverfahrens vorgelegen. Sie wurde in ihrer Gesamtheit nicht veröffentlicht und auch nicht zur Veröffentlichung eingereicht.

Nina Schwalb

Abstract

In the present *Thesis*, the dynamics of key building blocks of the DNA, namely (i) free nucleobases, (ii) selected, well-defined hydrogen-bonded base pairs as well as larger H-bridged aggregates, and (iii) short single- or double-stranded DNA oligonucleotides and self-complementary DNA oligonucleotide loops have been studied in a systematic bottom-up strategy to assess their roles for the photostability of DNA. Experimental measurements were carried out by the UV femtosecond fluorescence up-conversion technique. Tunable UV pump pulses were used to monitor the excited-state decays after excitation close to the electronic origin and to significantly higher energies above.

(i) The monomeric base N^6,N^6 -dimethyladenine (DMA), which is a double aminomethylated derivative of the naturally occurring nucleobase adenine (A), has been investigated in solvents of different polarity. Although it is only slightly modified compared to its parent molecule A, in which the fluorescence decays on a sub-picosecond timescale, the fluorescence decay behavior of DMA was determined to be completely different. It exhibited multiple fluorescence time components ranging from the sub-picosecond timescale up to nanoseconds. Thus, a very complex excited state topology was found, with participation of an intramolecular charge transfer state.

(ii) The non-radiative electronic deactivation dynamics of isolated hydrogen-bonded Watson-Crick (WC) and non-WC DNA base pairs in comparison to their underlying free nucleosides have been studied in solution. Towards these ends, specially (2'),3',5'-TBDMS-protected TBDMS nucleoside derivatives have been synthesized and characterized by static FTIR spectroscopy. The guanosine-cytidine (G··C) WC base pair was found to be the most outstanding example, exhibiting a hydrogen-bond related electronic deactivation mechanism. A single, globally active ultrafast relaxation pathway has been identified. It is directly accessed after photoexcitation, independent on how much excess energy has been dumped into the molecule. This reduces the excited-state electronic lifetime of the G··C WC base pair by orders of magnitude compared to the underlying free and unpaired nucleobases. The observed effect was most pronounced for G, which points at a G-to-C relaxation mechanism. Moreover, it was shown that homopurine base pairs do benefit in a similar way on dimerization, while homopyrimidine base pairs lack this intrinsic property. In contrast, higher H-bonded aggregates with extended hydrogen-bonding networks, which constitute model systems for DNA super-structures like DNA tri- and quadruplexes, did not exhibit ultrafast photodynamics.

(iii) For a series of single- and double-stranded DNA oligonucleotides, it was found that base-pair-related hydrogen-bonding dynamics compete with π -stacking interactions. Pure and thus atypical, but highly stacked runs of homopurine oligomers display rather long-lived photodynamics. A drastic acceleration could be observed by substitution of only a few bases by the other purine base and its complementary counterpart in the oligomer duplexes. G·C-rich sequences were found to profit most on duplex formation. This hints at the importance of the G-to-C relaxation process for DNA double helices.

Zusammenfassung

In der vorliegenden *Dissertation* wurde die Dynamik von Schlüsselbausteinen der DNA, d.h. (i) freien Nukleobasen, (ii) ausgewählten, eindeutig charakterisierten Wasserstoffbrücken-gebundenen Basenpaaren als auch größeren H-gebundenen Aggregaten und (iii) kurzen einfach- und doppelsträngigen DNA-Oligonukleotiden und selbstkomplementären DNA-Oligonukleotid-Strängen in einer systematischen ‘bottom-up’-Strategie studiert, um ihre jeweiligen Rollen bezüglich der Photostabilität der DNA zu taxieren. Alle experimentellen Messungen wurden mit der Methode der Femtosekunden-UV-Fluoreszenz-Aufwärtskonvertierung durchgeführt. Über durchstimmbare UV-Pumpimpulse konnte das Fluoreszenz-Abklingverhalten nach Anregung am elektronischen Ursprung bzw. in höhere Schwingungszustände des angeregten Zustands bestimmt werden.

(i) Das Basenmonomer N^6,N^6 -Dimethyladenin (DMA), welches ein doppelt aminomethyliertes Strukturderivat der natürlichen Nukleobase Adenin (A) ist, wurde in Lösungsmitteln verschiedener Polarität untersucht. Obwohl DMA im Vergleich zu seinem Muttermolekül A, für das ein Fluoreszenz-Zeit-Verhalten auf der Sub-Picosekunden-Zeitskala beobachtet wurde, nur gering modifiziert ist, zeigte sich für DMA ein deutlich anders geartetes Fluoreszenz-Abklingverhalten, welches die Sub-Picosekunden- bis Nanosekunden-Zeitskala abdeckte. Aufgrund dessen wurde auf eine komplexe elektronische Struktur unter Beteiligung eines Ladungstransfer-Zustandes geschlossen.

(ii) Spezielle (2'),3',5'-TBDMS-geschützte Nukleosid-Derivate wurden synthetisiert und mittels statischer FTIR-Spektroskopie charakterisiert, um die strahlungslose elektronische Deaktivierungsdynamik von isolierten H-Brücken-gebundenen Watson-Crick (WC) und Nicht-WC Paaren in Lösung zu bestimmen. Hierbei zeigte besonders das Guanosin·Cytidin ($G \cdots C$) WC Basenpaar eine klare H-Brücken-bezogene Photodynamik. Es konnte ein einzelner elektronischer Deaktivierungsweg bestimmt werden, der dafür sorgt, dass die elektronische Lebensdauer um Größenordnungen kleiner ist, als in den zugrunde liegenden freien und ungepaarten Nukleobasen. Dieser Effekt war besonders stark für G ausgebildet, was auf einen G-zu-C Mechanismus schließen ließ. Dieser Relaxationspfad ist direkt nach der Photoanregung zugänglich, unabhängig davon wie viel Überschussenergie im Basenpaar platziert wurde. Es zeigte sich, dass Homopurin-Basenpaare in ähnlicher Weise von der H-Brücken-vermittelten Dimerisierung profitierten, während ein entsprechender Mechanismus in Homopyrimidin-Basenpaaren fehlte. Höhere H-gebundene Aggregate mit ausgedehnten Wasserstoffbrücken-Netzwerken, die Modellsysteme für DNA-Superstrukturen wie DNA Tri- und Quadruplexe darstellen, wiesen dagegen keine schnelle Photodynamik auf.

(iii) Für eine Reihe von einfach- und doppelsträngigen DNA-Oligonukleotiden konnte gezeigt werden, dass die H-Brücken-Dynamik mit π -Stapelwechselwirkungen konkurriert. Reine und daher atypische, aber stark gestapelte Homopurin-Oligomere zeigten eine eher langlebige Dynamik. Durch den Austausch von nur wenigen Basen durch die jeweils andere Purinbase, und ihr komplementäres Gegenstück im Fall einer Oligomer-Duplex, konnte eine starke Beschleunigung der Photodynamik beobachtet werden. Dies deutet auf die Relevanz des G-zu-C Relaxationpfades für die DNA-Doppelhelix hin.

Contents

1	Introduction	1
1.1	The Structure and Function of DNA	3
1.2	Introduction to Femtosecond Spectroscopy	8
1.3	Photodynamics of DNA	11
1.4	Scope and Contents of the Present <i>Thesis</i>	23
	References and Notes	27
2	Experimental Methods	35
2.1	Introduction to Nonlinear Optics	37
2.1.1	Optical Kerr Effect, Group Velocity Dispersion and Phase Modulation	38
2.1.2	Frequency Mixing and Conversion Processes	39
2.2	Femtosecond Fluorescence Spectroscopy by Optical Gating	41
2.2.1	Femtosecond UV Fluorescence Up-Conversion Technique	42
2.2.2	Setup of the UV Fluorescence Up-Conversion Experiment	44
2.2.3	Broadband Detection Techniques	50
2.3	Data Analysis	55
2.4	Sample Preparation and Handling	58
2.5	Stationary Spectroscopy	63
	References and Notes	67
3	Femtosecond Time-Resolved Fluorescence Spectroscopy of N^6,N^6-Dimethyladenine: New Explanation of the “Dual Fluorescence” Dynamics from Decay and Rise Time Measurements at Threshold	69
	Abstract	71
4	A Modified Four-State Model for the “Dual Fluorescence” of N^6,N^6-Dimethyladenine derived from Femtosecond Fluorescence Spectroscopy	73
	Abstract	75
5	Ultrafast Electronic Relaxation in Guanosine is Promoted by Hydrogen Bonding with Cytidine	77
	Abstract	79
	Supporting Information	81
6	Ultrashort Fluorescence Lifetimes of Hydrogen-Bonded Base Pairs of Guanosine and Cytidine in Solution	83
	Abstract	85

7	A Combined FTIR and DFT Study of Hydrogen-Bonded Complexes of Cytidine in Solution	87
	Abstract	89
	Supporting Information	91
8	On the Structure and Photostability of Cytosine Self-Assemblies with Extended Hydrogen-Bonding Networks	93
	Abstract	95
9	Spectra and Dynamics of the G-Tetrad, a Model for G-Quadruplex DNA	97
	Abstract	99
10	Base Sequence and Higher-order Structure Induce the Complex Excited-State Dynamics in DNA	101
	Abstract	103
	Supporting Information	105
11	Concluding Discussion	107
	11.1 Fluorescence Decays of DNA Monomers	109
	11.2 Fluorescence Decay Dynamics of H-Bonded DNA Base Pairs and Self-Assemblies	110
	11.3 Short DNA Single Strands and Duplexes	112
	11.4 Ongoing and Future Experimental Work	114
	11.5 Discussion of Recent Theoretical Studies	118
	References and Notes	121
	Appendix	123
	A DNA Monophosphates	125
	B Gaussian Band Analysis of the FTIR Spectra of G, C and G···C	127
	C Hydrogen Bonding Dynamics in A···T and 2AP···T Base Pairs	133
	D Control Programs	139
	Danksagung	151
	Curriculum Vitae	153

Chapter 1

Introduction

The deoxyribonucleic acid (DNA) is the carrier of the genetic information of life on Earth. Thus, it is arguable the most important and most intensely studied biomolecule. The origins of nucleic acid research go back to the late nineteenth and the beginning of the twentieth century, but it was not before the 1940s that experiments confirmed the ability of DNA to store, replicate and transfer the genomic information of an organism [1]. It took another decade of intensive research to determine its molecular structure. Finally, the discovery of the double helical structure of DNA and its exceptional biological implications laid the basis for the nowadays well established fields of structural biology, life sciences and biotechnology [2]. The development peaked in the complete decoding of the human genome in 2003 [3].

Structurally motivated aspects dominated nucleic acid research over the last 60 years [4–6]. More recently, studies of the dynamics moved into the foreground. Particular interest arose in the photophysics and the underlying photodynamics of the DNA and its constituent nucleobases [7–9]. Both were found to exhibit extraordinarily high photostabilities. On a molecular level, this manifests itself in extremely low fluorescence quantum yields and ultrashort excited-state lifetimes of the optically bright photo-excited states. The rapid development of powerful spectroscopic and computational techniques in the recent years significantly contributed to the understanding of the microscopic processes behind the so-called nonradiative electronic deactivation dynamics of DNA. Nevertheless, the relatively unexplored field of DNA biophysics is considered as a new frontier in DNA research.

The present *Thesis* deals with the ultrafast electronic deactivation dynamics of low-fluorescent DNA model systems by means of femtosecond UV fluorescence spectroscopy. In the last three years, the research on the DNA photodynamics has expanded from single DNA bases to higher DNA multimers. As the work in this *Thesis* was carried out in parallel, the obtained results contribute fundamentally to the state-of-the-art knowledge about the photodynamic behavior of DNA [9–17].

The subsequent sections of this *Introduction* are organized as follows: First, the basics of the structure and function of DNA will be summarized. Second, the principles of femtosecond spectroscopy will be described. Third, the current knowledge in the field of DNA photodynamics is reviewed, including the concept of conical intersections. Fourth, a detailed description of the scope of this *Thesis* will be given.

The subsequent chapters will then present the particular results of the different experiments performed within this *Thesis*.

1.1 The Structure and Function of DNA

DNA is a chain-like polymer. It consists of a deoxyribose and monophosphate containing subunit, which makes up the polymer backbone. Each subunit is linked to one of the four DNA bases. These nucleobases are nitrogen containing heteroaromatic purine or pyrimidine cycles. The two purine bases adenine (Ade) and guanine (Gua) as well as the

pyrimidine bases cytosine (Cyt) and thymine (Thy) are found in DNA, whereas the latter is exchanged by uracil (Ura) in the closely related ribonucleic acid (RNA). A free nucleobase attached to the deoxyribose moiety is a nucleoside and the respective names change to adenosine (Ado), guanosine (Guo), cytidine (Cyd) and thymidine (Thd). Nucleotides are made up by a free nucleoside X and the phosphate group, giving the deoxyribose monophosphates XMP. For simplification, adenine containing units are abbreviated in the following by A, those with guanine as G, cytosine as C and thymine as T. The chemical structures of the respective compounds are given in Fig. 1.1. The nucleobase is always attached at the 1' position of the sugar. The linkage of the phosphate to the deoxyribose moiety occurs at the 5' terminal. If the nucleobase is incorporated in DNA, the next nucleobase is attached via the deoxyribose-phosphate backbone in 3' position.

Aside from the covalent linkage of nucleobases within one single strand by the deoxyribose-phosphate backbone, a second strand can be attached through non-covalent hydrogen bonds between two nucleobase in the so-called complementary Watson-Crick (WC) architecture. This pattern entails the pairing of G with C through three hydrogen bonds and the combination of A with T (or U in RNA, respectively) by two hydrogen bonds. Both strands run in opposite directions ($3' \rightarrow 5'$ and $5' \rightarrow 3'$). Typically, the complementary strands are organized in a double helical configuration, in which the nucleobase pairs represent the core of the helix, while the charged phosphate groups of the backbone point to the outside. The standard DNA shape is the close-packed B form. Other important double helical motifs, like the A- and Z-form, have been found as well. Fig. 1.2 gives an overview of the structures of the three helical motifs (I-III) and their most important helical parameters. Those have to be considered as average parameters, derived from the crystal structures of different DNA sequences.

B-DNA (Fig. 1.2a) contains $\approx 92\%$ water and exhibits a right-handed sense with a C-2' endo sugar pucker and the *anti*-conformation of the glycosidic bond. The sugar pucker describes the major displacement of the deoxyribose moiety. In the C-2' endo-configuration, which is given in Fig. 1.2 IVa, the O-3' atom is in axial position and thus, the C-2' atom is equatorial (\equiv endo). The molecular plane of the nucleobases is mostly perpendicular oriented to the deoxyribose moieties. In the *anti*-conformation of purine (pur) bases, the H-8 atom is centered above the sugar (see Fig. 1.2 IVc), whereas pyrimidine (pyr) bases have the H-6 atom above the sugar. The helical repeat in B-DNA is $hr_B = 10.5$ base pairs, which corresponds to a internucleobase distance of $d_B = 0.33 - 0.34$ nm and a relative twisting angle of $\theta_B \approx 36^\circ$ per base pair (bp). The relative tilting angle between the adjacent nucleobases is given by $\gamma_B \approx 6^\circ$. The relative angle between the helical axis and the base pairs is $\alpha_B \approx 90^\circ$. The B-DNA helical diameter is $r_B = 2.37$ nm.

The A-DNA form (Fig. 1.2 II) can be derived from the B-form by dehydration or by the addition of salt, ethanol or trifluoroethanol [18–21]. It has, as well, a right-handed helical sense, but contains only $\approx 75\%$ water. The sugar pucker is changed to C-3' endo, while all glycosides remain in the *anti*-conformation. In the C-3' endo-configuration, which is

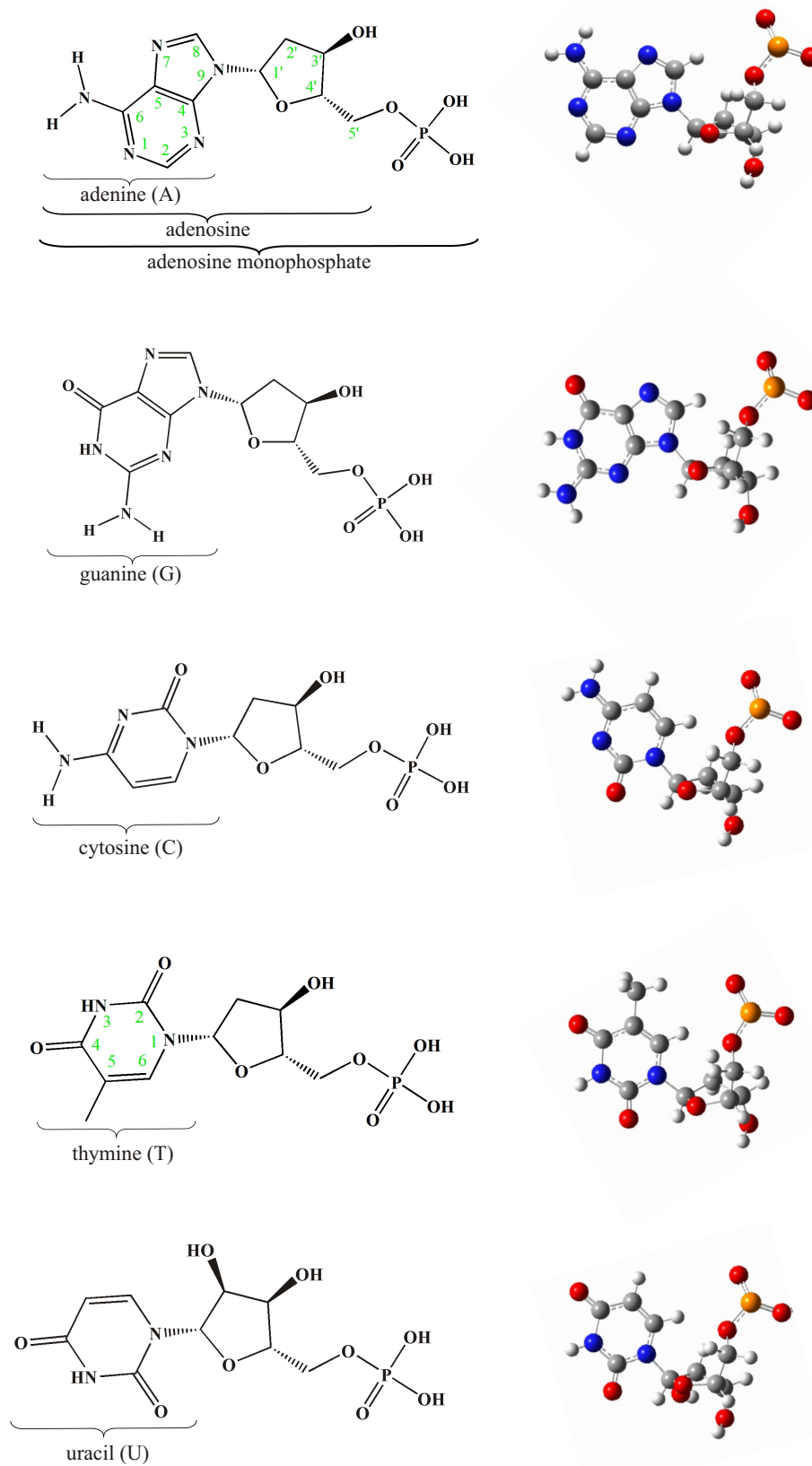


Figure 1.1: Structures of the DNA/RNA nucleobases, nucleosides and nucleotides.

given in Fig. 1.2 IVb), the O-3' atom is in equatorial position and thus, the C-3' atom is axial (\equiv exo). This entails a considerable change of the helical geometry: A-DNA exhibits $hr_A = 11$ base pairs per helical turn, which gives an internuclear distance of $d_A = 0.23$ nm. The relative inter-helical angles are now given by $\alpha_A \approx 74^\circ$, $\theta_A \approx 33^\circ$ and $\gamma_A \approx 20^\circ$. It has a comparatively high helical diameter of $d_A = 2.56$ nm and therefore, A-DNA displays a central helical hole.

The Z-helix is likewise an anti-parallel oriented, but left-handed duplex, which contains only $\approx 66\%$ water. It is rather rare, but best represented by an alternating [d(G)-d(C)] sequence. Its name originates from its zig-zag backbone, which is caused by the alternating conformation of the deoxyribose moiety. It periodically changes between the *syn*-conformation for the incorporated dG and the *anti*-conformation for dC. In the *syn*-conformation of pur bases, the N-3 atom is centered above the sugar and the pyr bases have the O-2 atom above the sugar (see Fig. 1.2 IVd). Additionally, the dG residues exhibit a C-3' endo sugar pucker, while the sugar pucker of dC is C-2' endo. The helical repeat of Z-DNA is $hr_Z = 12$ bases and the inter-nucleobase distance has a value of $d_Z = 0.37$ nm. Furthermore, $\alpha_Z \approx 80^\circ$, $\theta_Z \approx 60^\circ$ and γ_Z is given by $\approx 7^\circ$. The helical diameter was found to be $r_Z = 0.9$ nm.

The specific WC pairing of the nucleobases via hydrogen bonds in the helical center is essential for the storing and copying processes of the genomic information. On cell division, both daughter cells need to obtain the same cellular and genetic equipment. DNA replication is the fundamental process to duplicate the inheritable material. The replication procedure is initiated at the replication origin. Here, a species-specific A,T-rich sequence is recognized by a protein complex. Then, the enzyme DNA topoisomerase unwinds the helix and the DNA helicase separates the two annealed DNA strands. This appears as the replication 'fork' of the helix. The replication process is semi-conservative, which means that both unwound ends serve as templates. The leading strand is copied in the 5'→3' direction. The duplication process starts after a primer has been attached to the strand by a RNA polymerase. It provides a free 3'-OH group. This is used by the DNA polymerase III to continuously synthesize the copied strand in the direction of the replication fork. DNA polymerase III cannot operate on the lagging strand in the 3'→5' direction. Instead, the strand is synthesized in short segments with 5'→3' direction. Each has its own RNA primer to initiate the DNA polymerase III. The numerous RNA fragments are removed by another DNA polymerase and DNA ligase connects the single, so-called Okasaki segments of the new strand by adding suitable deoxynucleotides. The termination of the replication process occurs automatically: The DNA polymerase III stops, when the end of a linear chromosome, the telomere, is reached. It fails to fully synthesize the telomeric end and thus, telomere shortening occurs. The loss of DNA on cell divisions limits the number of division cycles and the lifetime of the cell, as the loss of the telomeric ends leads to apoptosis. Finally, the two synthesized double strands are wound back into the helical topology by DNA topoisomerase.

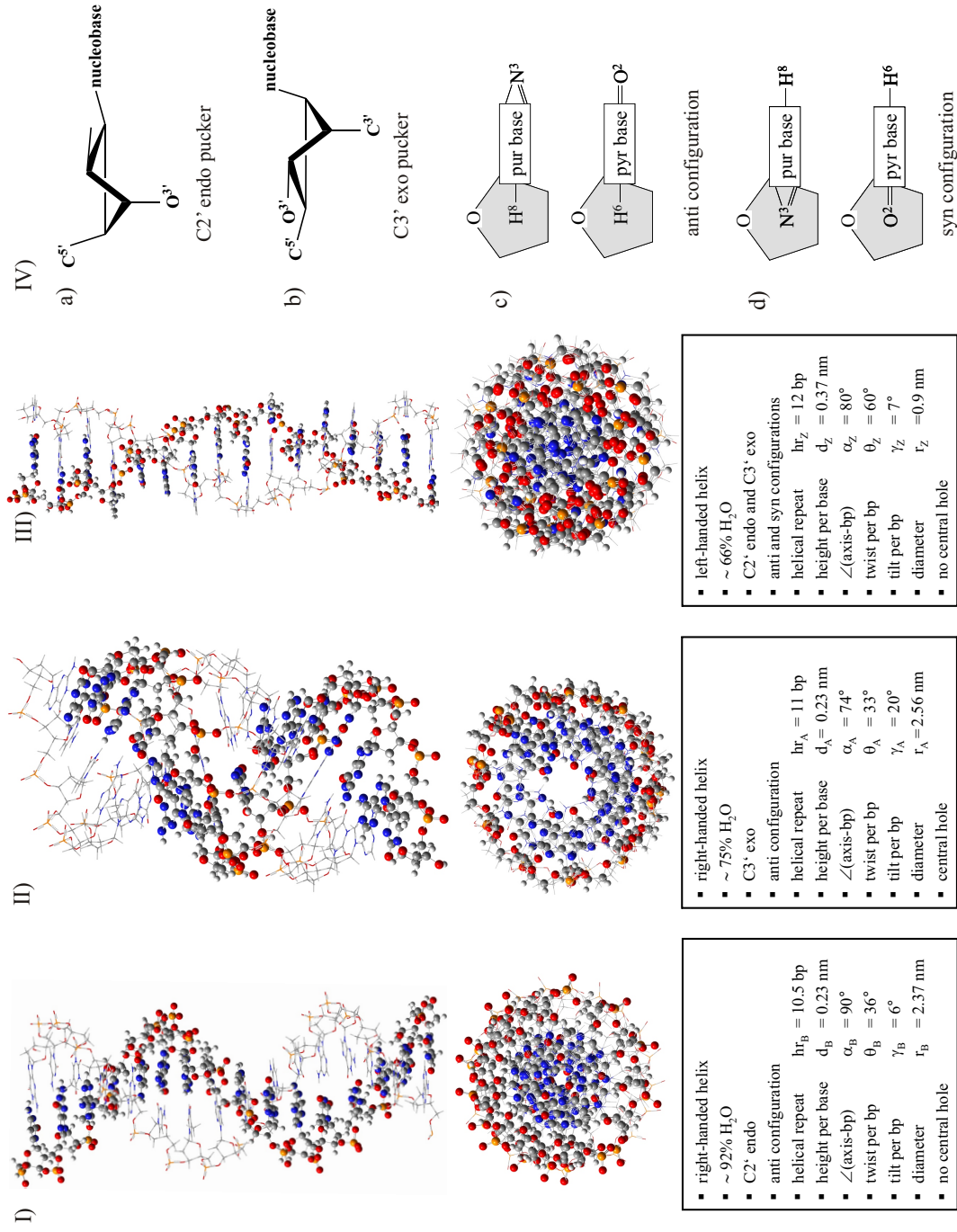


Figure 1.2: Standard secondary structures of DNA in side and top view. The respective average helical parameters are given below: (I) B-DNA, (II) A-DNA, (III) Z-DNA. Column (IV) gives a detailed view of the conformational shapes of deoxyribose units (a, b) and shows the possible relative orientation of the nucleobase vs. the deoxyribose moiety (c, d)

The genetic information of the DNA can be made available by the process of gene expression. This transfers the genomic code into a physiologically active gene product, e.g., into a protein, which is relevant to the cell's metabolism and functionality. The underlying building blocks of proteins are the amino acids. A nucleobase triplet (\equiv codon) is the decoding fragment for one amino acid. The inherent information ('message') of the triplet is copied into a codon of a RNA sequence, the so-called messenger RNA (mRNA). It transports the information from the DNA to the cell's ribosomes. Here, the codon is translated by the transfer RNA (tRNA), which carries the respective anti-codon. The tRNA is attached to one specific type of amino acids at its 3' end. In the ribosome, the amino acids are combined to the respective protein sequence under release of the tRNA residue. The correct transcription and translation procedure is, like the replication process, ensured through the specific recognition process, which relies on the complementary WC base pairing motif.

Other, non-standard, hydrogen-bonded base pairs have been identified as well. Hairpin-looped secondary structures of RNA have been found to include reverse-Watson-Crick and (reverse-)wobble or sugar-edge binding motifs. (Reverse-)Hoogsteen base pairs are essential for the formation of the well-known triplex and quadruplex structures of DNA (and RNA). In triplex formation, a third single DNA strand binds to the Watson-Crick duplex. It occurs in sequences of high homopurine and -pyrimidine tracts. As this results in a sequence- and site-specific recognition of the target duplex, DNA triplexes have been addressed as therapeutical agents. G-rich sequences can form parallel-stranded quadruplex structures. This structure has

been found at eukaryotic telomeres and centromeres. Both units are essential for the stability of DNA and participate in cell replication, cell division and mitosis [22–24]. It has been shown that the cyclic G tetrad motif is prone to intercalate specific substances. Hence, they can be used as nucleic acid aptamers. Aptamers can recognize, bind and release specific target molecules and are thus useful in biotechnological and therapeutic applications. A typical aptamer structure is given in Fig. 1.3.

1.2 Introduction to Femtosecond Spectroscopy

The field of chemical kinetics and reaction dynamics underwent a remarkable development in the last 100 years. Initially, it was only possible to identify macroscopic characteristics

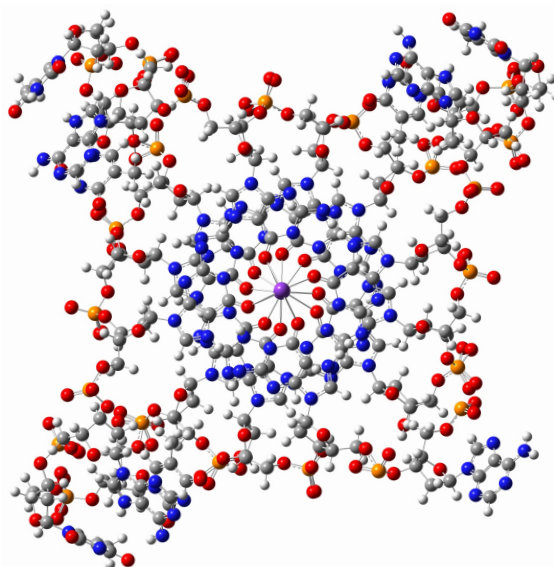


Figure 1.3: Parallel-stranded G quadruplex structure formed by human telomeric DNA. Image created from NDB UD0017.

of a reaction system. Here, research goes back to the Arrhenius equation

$$k = A \cdot \exp \left[\frac{-E_A}{RT} \right], \quad (1.1)$$

which gives the rate of a reaction in dependence of the temperature [25]. In the 1930s, Eyring and Polanyi were the first to succeed in a microscopic description by the development of the **Transition State Theory** (TST) [26, 27], in which the bimolecular reaction rate is given by

$$k = \frac{k_B T}{h} \frac{Q^\ddagger}{Q_A \cdot Q_B} \cdot \exp \left[\frac{-\Delta E_0^\ddagger}{k_B T} \right]. \quad (1.2)$$

Each chemical reaction requires a specific threshold energy ΔE_0^\ddagger and, if this is overcome, the educts transform into product states along the minimum energy path (MEP) by crossing a characteristic transition state. To the present day, experimentalists try to shed light on the initiating events leading to the transition state. Early studies have been done by flash photolysis by Norrish and Porter [28]. Eigen introduced the temperature-jump method to monitor proton transfer reaction. Molecular beam experiments, performed by Herschbach, Lee and Polanyi, allowed an indirect estimation of some characteristic features of the transition state [29–31]. All received Nobel Prizes for their pioneering studies.

But, since the motion of a single molecular unit or the transfer of single atoms, i.e., protons along a hydrogen bond, is of interest, the timescale to elucidate the processes at the transition state ranges from several femtoseconds to a few picoseconds. This is the timescale of the ‘making and breaking of bonds’. Such ultrafast events can be made visible by applying a suitable, stroboscope-like technique, which sets a certain acquisition starting point and then takes snapshots at discrete time intervals with the requested time resolution. In consequence, the sampling event must be even faster than the molecular events, which are to be investigated.

Femtosecond spectroscopy became technically feasible not before the invention of suitable lasers in the 1970s – 1980s, which provided pulses of sub- 10^{-12} ps duration [32–35]. Pioneering work has been performed by A. H. Zewail, who is considered as the originator of the field of femtochemistry and received the Nobel Prize in 1999 [36–40]. He and co-workers successfully applied the so-called pump-probe technique to detect ultrafast molecular events in real time. A schematic view of the experimental pump-probe setup is given Fig. 1.4a. The intensity-time profiles of the laser pulses used in this technique and the intensity-time profile of the detected signal are shown in Fig. 1.4b-d: In the pump-probe experiment, an ultrafast, femtosecond laser pulse (shown in blue in Fig. 1.4) is used to photo-excite the sample molecules (b). The resulting molecular response, which is indicated by the solid line in Fig. 1.4b, is then detected (probed) by a second, time-delayed femtosecond pulse (given in dark red). The probe sequence is sketched in Fig. 1.4c. The time lag of the second pulse is achieved through a (computer-controlled) delay stage, defined by the relation between distance and time. Thus, the molecular signal is monitored in discrete delay time steps Δt ,

relative to the initiating pump pulse. The resulting sampling points are given as circles in Fig. 1.4d.

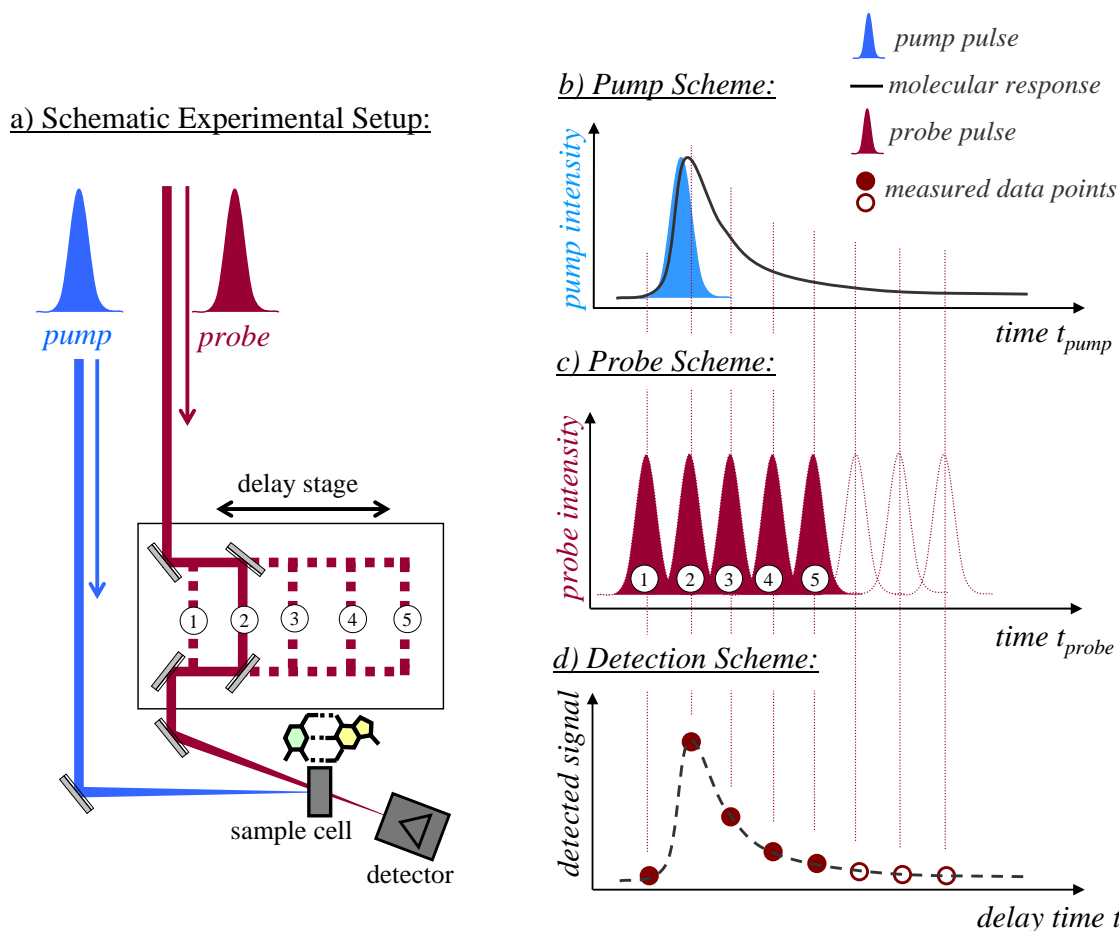


Figure 1.4: Pump-probe principle: (a) Schematic experimental setup: A femtosecond pump pulse (blue) is focused into the sample cell and excites the sample molecules. The resulting molecular signal is detected in discrete time steps via a second, time-delayed femtosecond probe pulse (red). (b) Intensity-time profile of the exciting pulse (blue) and the resulting molecular response (solid black line). (c) Intensity-time profile of the probe pulse sequence. For simplification, only the first five delay steps are correlated to the specific displacements of the delay stage in (a). (d) Intensity-time profile of the detected signal: The dashed lines indicates the molecular response, which is monitored in discrete sampling intervals. The measured data points are given as circles. Solid circles belong to probe pulses, which can be correlated to specific movements of the delay stage given in (a). Open circles have, for simplification, no counterpart in (a).

The pump-probe principle can be applied in different modes. The most popular method is the transient absorption technique, which is used in all spectral regions, ranging from the UV to the IR [35, 41, 42]. It can be easily extended into a 2D mode, which is similar to 2D static NMR spectroscopy [42, 43]. Pump-probe photo-ionization techniques (transient mass spectrometry or ion/electron imaging) and femtosecond fluorescence spectroscopy are limited to the UV and VIS [35, 41]. Other techniques, including multiple light waves, are Coherent Anti-Stokes Raman scattering (CARS) and (degenerate) four-wave mixing ((D)FWM) spectroscopy. Very recently, the pump-probe scheme was extended to x-ray and surface or interface specific spectroscopy [44, 45].

1.3 Photodynamics of DNA

Excited-state femtosecond spectroscopy is the required experimental technique for elucidating the photodynamics and the underlying photophysical processes of the DNA. The DNA bases are chromophores and have high cross-sections for the absorption of short-wavelength UV light and thus, the DNA is highly photosensitive. UV irradiation deposits a large amount of excess energy in the photo-excited molecules, which can initiate structural rearrangements, the breaking of bonds or other photo-induced reactions. Consequently, serious photodamage like UV-induced mutagenesis can result, which may lead to misdirected gene expression, cell mutations, cell death or, in the worst case, to an uncontrolled growth of cells and malignant tumors (cancer).

Nature has developed a series of cellular DNA repairing mechanisms, but these become active only after photodamage has occurred and after corrupted DNA segments have been recognized by the respective repairing enzymes [46]. Although the amount of UV light, which reaches the Earth's surface is substantially reduced by scattering in the upper atmosphere or via absorption by ozone, a non-negligible amount of UV-A and UV-B radiation can reach vulnerable, deeper parts of the skin. Obviously, the cellular repair mechanism can not account alone for the integrity of the DNA, as it would be dramatically overburdened.

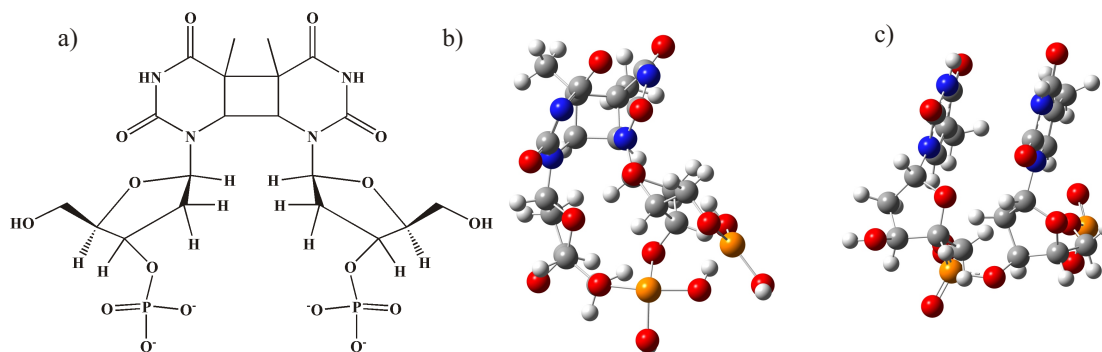


Figure 1.5: Cyclobutane pyrimidine dimer (CPD) formation in T. The chemical structure of the T-CPD is given in a). A comparison of the T-CPD structure (b) vs. the intact T dinucleotide (c) is given on the right.

DNA photolesions have been discussed for years [47]. The formation of cyclobutane pyrimidine dimers (CPD) by two nearby pyr bases can be considered as one of the most frequent photoproducts. Cycloaddition leads to covalent linkage between the pyrimidine nucleobases due to the C=C double bonds, as illustrated in Fig. 1.5. Another less frequently occurring, but more mutagenic pyrimidine photolesion is the 6,4-pyrimidine-pyrimidone photoproduct [48]. Moreover, it has been discussed, whether 8-oxo-7,8-dihydroguanine formation, which is generated from G through hydroxy radical attack, is catalyzed by UV irradiation [49].

The bulk of absorbed UV photons do not induce photolesions. For T, the respective CPD quantum yield is of the order of $\approx 10^{-2}$. Thus, an upper limit for the extent of UV-caused

mutations is $\lesssim 1\%$ [50–55]. Consequently, DNA must exhibit an additional, intrinsic photophysical protecting mechanism, which leads to a very efficient, radiationless dissipation of the excess energy supplied by absorbed UV photons, before profound photodamage takes place. The photophysical and photochemical processes behind these electronic deactivation mechanisms are a matter of substantial interest, because they can allow for extremely short excited-state lifetimes, which minimize the risk of photodamage in the high-energy excited states. This is reflected by the very low fluorescence quantum yields, which is of the order of 10^{-4} , and the rapid nonradiative ground state recovery of the DNA and its building blocks.

The driving forces behind the electronic deactivation mechanisms are so-called non-adiabatic couplings at conical intersections. This concept will be explained in the following subsection. Subsequently, a review of the state-of-the-art research on the photodynamics of DNA model systems will be given. It will cover experimental and theoretical results on nucleobase monomers, hydrogen-bonded complexes, π -stacked aggregates, short DNA oligonucleotides (sequence length 2 – 20 bases), and polymers made up by ≥ 200 nucleobases.

1.3.1 The Concept of Conical Intersections

The concept of conical intersections (CIs) has changed the field of photodynamics drastically within the last 5 – 15 years [56–59]. CIs result from non-adiabatic vibronic coupling terms, which are neglected in the standard, adiabatic Born-Oppenheimer approach of the description of electronic potential energy hypersurfaces (PEHS). In the Born-Oppenheimer picture, which is given in Fig. 1.6a, two electronic surfaces must be far from each other. After photo-excitation, which is indicated by the vertical dashed arrow in Fig. 1.6a, a wavepacket is prepared in the excited state E(2). The resulting excited-state dynamics in E(2) are completely separated from E(1), as long as the states E(2) and E(1) do not interact.

Non-adiabatic coupling terms must necessarily be taken into account if two potential energy surfaces become close to each other. They describe, how the two electronic states E(1) and E(2) are coupled by the nuclear motion. The coupling requests a number of symmetry-lifting nuclear degrees of freedom. These are not given in diatomic molecules. Consequently, the two close-coming electronic states of a diatomic molecule will always be separated by a certain amount of energy along the MEP, they will always avoid to cross [60–62]. Fig. 1.6b sketches the excited state topology for a diatomic molecule: In the vicinity of the expected crossing (dashed lines), the two states E(1) and E(2) repel each other and avoid the crossing. The wavepacket, generated through photo-excitation in the upper state E(2) can switch to the lower state E(1). This can be described in the picture of Landau-Zener [63]. However, this picture does not consider molecular dynamics and a description of ultrafast processes remains elusive.

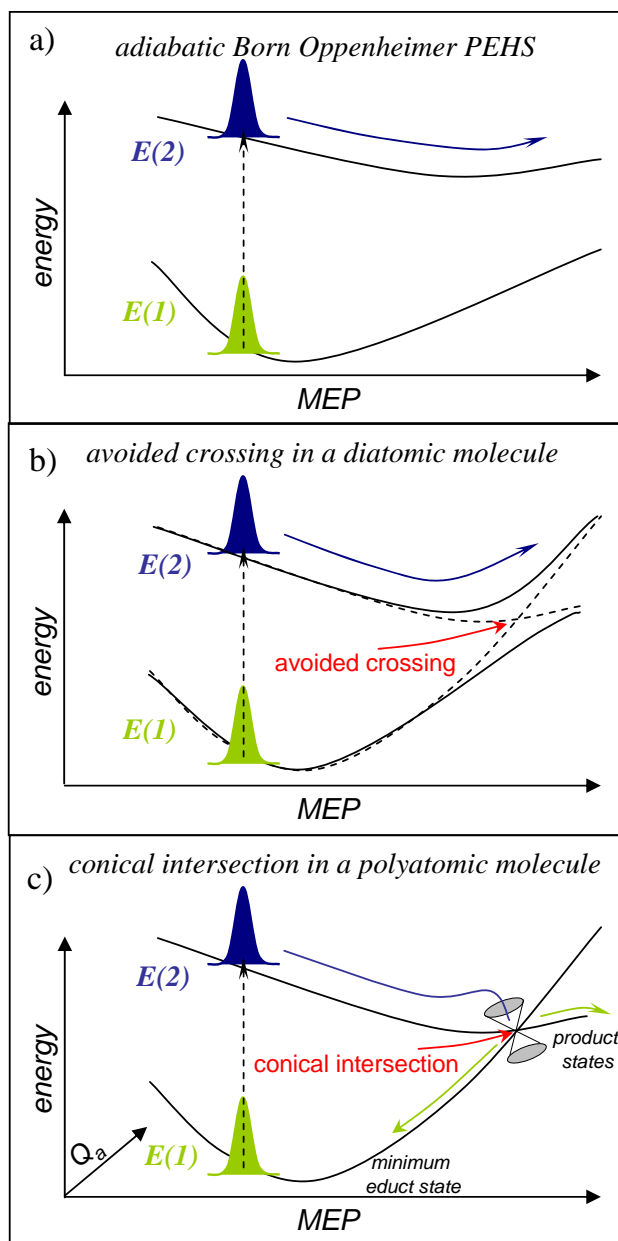


Figure 1.6: Concept of conical intersections. a) Sketch of the 'standard' adiabatic Born-Oppenheimer description for two well-separated electronic states E(1) and E(2). b) The two electronic states E(1) and (2) of a diatomic molecule do intersect in the diabatic picture (dashed line), but show an avoided crossing in the non-adiabatic picture (solid lines) due to a non-negligible amount of energy along the minimum energy path (MEP), which separates both. c) The two nearby electronic states E(1) and E(2) of a polyatomic molecule have a conical intersection (CI) along the MEP in the non-adiabatic picture, which is mediated by a vibrational mode Q_a . In all cases, photo-excitation is indicated by a vertical dashed arrow. Dynamics in the upper electronic state E(2) are indicated by a dark blue 'wavepacket', those in the lower state are given in green.

The non-crossing rule does not apply to polyatomic molecules. Crossing along two particular coordinates in hyperspace can occur and gives a $(s-1)$ -dimensional seam of intersection (Fig. 1.6c). A nuclear motion (\equiv vibrational mode) of suitable symmetry (e.g., Q_a) can lift the degeneracy of the two states except at one particular point along the seam. This

leads to a $(s - 2)$ -dimensional crossing hyperpoint. It appears as a double cone topology, as given in Fig. 1.6c. The upper cone serves as a photochemical funnel and excited-state population can easily switch from E(2) to E(1). As one specific mediating vibrational mode is required, electronic relaxation via a CI is referred to as mode-specific deactivation.

1.3.2 Photodynamics of Nucleobase Monomers

Indirect hints for the outstanding photostability of the monomeric nucleobases have been posted quite early from static fluorescence spectroscopy [64]. The fluorescence quantum yields of the nucleobases have been determined to be of the order of $\Phi \approx 10^{-4}$ or even below. This indicated that the excited-state lifetimes of the emitting state must be of the order of several hundred femtoseconds. Hence, DNA chromophores have been considered to be ‘non-radiative’ species. Early results obtained by transient spectroscopy with picosecond time-resolution confirmed this assumption [65–67]. However, the picosecond time resolution later proved to be insufficient. Nucleobase monomers have been investigated by means of femtosecond spectroscopy only since about 10 years. A review has been published by Crespo-Hernández *et al.* [7].

Generally, all nucleobases exhibit at least three close-lying singlet excited states. Because of their nature, triplet states are not relevant to the ultrafast photodynamics of the DNA bases, but may play roles for the formation of some photoproducts on longer timescales. Two of the singlet states are closely spaced optically bright $\pi\pi^*$ transitions, named L_a and L_b in Platt’s nomenclature. At least one forbidden $n\pi^*$ state lies closeby.

Ultrafast non-adiabatic internal conversion processes have been determined experimentally and theoretically and have been found either to mediate between those states or to lead to a direct recovery of the ground states on the femto- to picosecond timescales [7, 68–83]. Additionally, intramolecular charge transfer states, mainly related to the N atoms of the heterocycles, might be populated and might act as intermediates in the excited-state decay dynamics of the monomers. As will be shown in this *Thesis*, they can give rise to rather long-lived (ps - ns) excited-state decay components. Quasi-dissociative channels involving $\pi\sigma^*$ states, are discussed as well [68, 76–79, 84–86]. They have been found to be active in pyrrole, which can be considered as a model system for DNA heterocycles [84, 87–89]. Nevertheless, it was argued by others that these states are not reachable in DNA nucleobases in non-gas-phase environments [76–79, 85, 86].

The different electronic relaxation pathways in the purine and pyrimidine bases have now been elucidated by numerous experimental and theoretical studies.

1.3.2.1 Purine Bases

The purine base A is the most intensely studied and, thus, the best understood DNA base. It can exist in two different tautomeric forms. The naturally occurring and hence

‘canonical’ form is *9H-A*, a minor tautomer is *7H-A*. The origins of the $\pi\pi^*(L_b)$ states of both tautomers, as well as some vibronic levels of the $n\pi^*$ state have been identified experimentally in molecular beam experiments [90–96]. The electronic lifetimes of these states after excitation close to the origin are found to be of the order of tens of picoseconds. The well-resolved vibronic bands of the $\pi\pi^*(L_b)$ and $n\pi^*$ states were followed by a broad, unstructured absorption band, when higher excitation energies were applied. Here, a much faster excited-state decay was observed in femtosecond multiphoton ionization experiments, which disclosed a biexponential decay behavior with electronic lifetimes of ≤ 0.3 ps [91, 97, 98]. Partly, this has been assigned to the $\pi\pi^*(L_a)$ state, while others claimed the $\pi\sigma^*$ state to be responsible [99–103].

Femtosecond experiments in the condensed phase have been carried out in water by means of transient absorption and fluorescence up-conversion measurements [104–111]. In water, the equilibrium between *9H-* and *7H-A* is no longer dominated only by the former. Thus, the observed excited-state decay was found to have contributions from an initial fast component (τ_1) of the order of several hundred femtoseconds, which was attributed to *9H-A*, while a long-lived component (τ_2) was found to describe the deactivation of the *7H-A* tautomer. A systematic exploration of the excited-state decay lifetime of A in dependence on the excitation energy and in different solvents has been carried out in our work group and revealed a slight elongation of the initial fast component, when the excess energy available after photo-excitation was low [110].

The ultrashort lifetime of τ_1 is commonly attributed to an excited-state decay from the $\pi\pi^*(L_a)$ state, which carries the higher oscillator strength. The value of τ_2 , on the other hand, were ascribed to the $\pi\pi^*(L_b)$ state of *7H-A*. This assumption was supported by high-level ab initio calculations [68–70, 75, 76, 78]. Several groups have determined the minimum energy pathways of the competing radiationless decay pathways starting from the spectroscopically prepared Frank-Condon (FC) region of the optically bright $\pi\pi^*(L_a)$ PEHS. Fig. 1.7 sketches the PEHS of *9H-A*, which can be considered to exemplarily represent the PEHS topology of the purine bases. The relative ordering of states in the FC region determined the $\pi\pi^*(L_a)$ state to be the third highest *in vacuo*, followed by the $\pi\pi^*(L_b)$ and $n\pi^*$ states. Arguably, the $\pi\pi^*(L_a)$ state is stabilized in the condensed phase and can be located much closer to the two other states. Photo-excitation prepares the optically bright $\pi\pi^*(L_a)$ state, because it carries the bulk of the oscillator strength. Possibly, the $\pi\pi^*(L_b)$ state comes into play at the origin of the strong first UV absorption band.

The major relaxation route for the *9H* tautomer is along the gradient of the PEHS, which was found to have strongly repulsive character, to a direct CI with the ground state, accessible without any barrier [75, 78]. This MEP exhibits no excited-state minimum, although it crosses the $\pi\pi^*(L_b)$ and $n\pi^*$ states. The latter states provide for only minor, secondary relaxation pathways. In contrast, the character of the $\pi\pi^*(L_a)$ state of *7H-A* is not repulsive, but it exhibits an expanded, plateau-like minimum, which was found to be nearly isoenergetic with the $\pi\pi^*(L_b)$ and $n\pi^*$ states [76, 78]. Internal conversion can

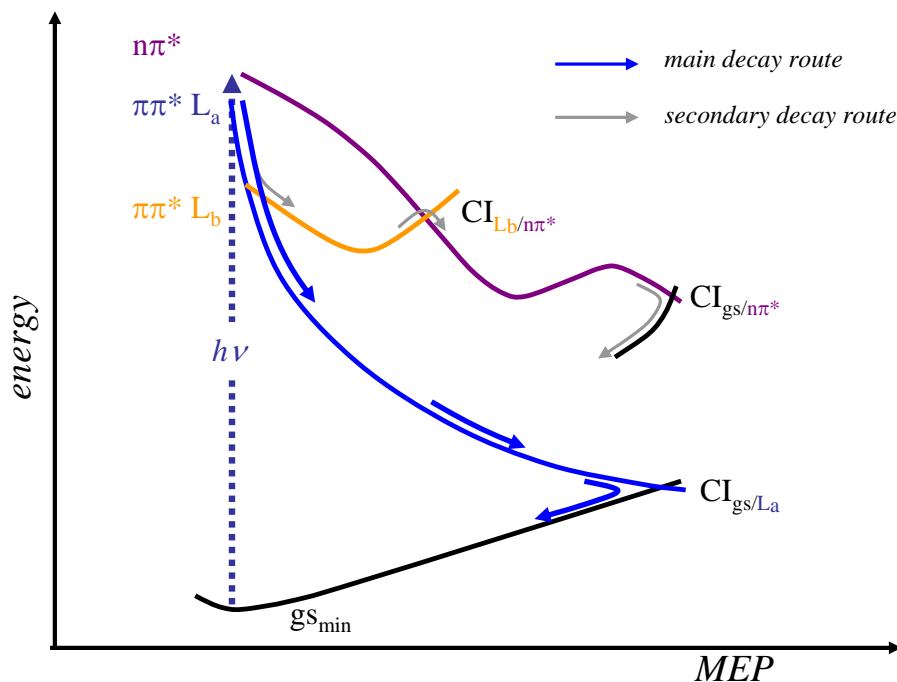


Figure 1.7: Electronic deactivation routes in *9H-A*: Photo-excitation prepares primarily the $\pi\pi^*(L_a)$ state. From the FC region of the $\pi\pi^*(L_a)$ state, a major relaxation route along the gradient of the $\pi\pi^*(L_a)$ PEHS leads to a direct CI with the ground state (gs). This pathway is barrierless. A minor, secondary pathway involves the nearby $\pi\pi^*(L_b)$ and $n\pi^*$ states, which can be populated through internal conversion processes. Other CIs deactivate the molecule from there.

thus easily lead to an immediate population of those states, especially of the $\pi\pi^*(L_b)$ state. Other, obviously less efficient, CIs can deactivate the molecules from there either directly to S_0 or indirectly by involving the $n\pi^*$ state as an intermediate. Finally, it must be noted that the excited-state dynamics observed in the gas phase or in the polar solvent water are sensitive to the relative ordering of the excited states: The dielectric environment induced by water stabilizes excited states with rather high dipole moments ($\pi\pi^*(L_a)$), but destabilizes nonpolar states ($n\pi^*$). This of course applies, *vice versa*, for the gas phase.

Closely related to the findings on A are those for the other purine base G, although theoretical studies on this base are not as numerous and are still conflicting [77, 79]. Although G exhibits two significantly separated absorption bands, which stem from the $\pi\pi^*(L_a)$ and $\pi\pi^*(L_b)$ transitions, the question whether these two show different dynamics has not yet been addressed. Only recently, we have studied the pump-wavelength dependent excited-state lifetimes of G in nonpolar and aprotic environments [13]. A strong dependence on the available excess energy was observed. The reader is referred to *Chapters 5* and *6* for these results. Earlier time-resolved experiments were performed at a single, fixed excitation wavelength of $\lambda_{pump} = 267$ nm, either in the gas phase using the multiphoton ionization technique or in aqueous solution by femtosecond transient absorption and fluorescence spectroscopy [7, 93, 94, 104–108]. Like A, G shows H tautomerism. A number of amino-imino and keto-hydroxy tautomers have been investigated by UV/UV and IR/UV double resonance spectroscopy [112].

1.3.2.2 Pyrimidine Bases

The biexponential excited-state decays of the pyrimidine bases C, T and U after excitation high above their electronic origins have been revealed by gas phase and solution phase techniques with femtosecond time resolution [73, 104–108, 113–117]. Due to ultrafast conversion processes inside T and U, only C gave well-resolved vibronic bands in molecular beam experiments [94]. Especially C and its derivatives have been the subjects, as pyrimidine representatives, of a number of combined experimental and theoretical studies. Fig. 1.8 pictures the relaxation routes of C, which were found to be active after photo-excitation. From the FC region of the spectroscopically prepared $\pi\pi^*$ state, the wavepacket can directly evolve back to S_0 by a direct CI. It was found that this deactivation pathway involves the optically dark, long-lived $n\pi^*$ state(s), which is populated during the relaxation process by a ‘threefold’ degenerate CI. This leads to a bifurcation of the excited-state population [72, 73, 80–83, 114, 118, 119]. First pump-wavelength dependent studies on the pyrimidine bases C and T have been performed in the context of this *Thesis* and details can be found in *Chapter 6* [13] as well as in the *Appendix*. No significant dependence was observable, which opposes the findings for the purine bases.

The pyrimidine bases have received further attention mainly due to the availability of triplet states in aprotic solvents [82, 119–121]. These have been found to be precursors for the formation of cyclobutane dimers, which represent the prevalent photolesion of DNA [50–55].

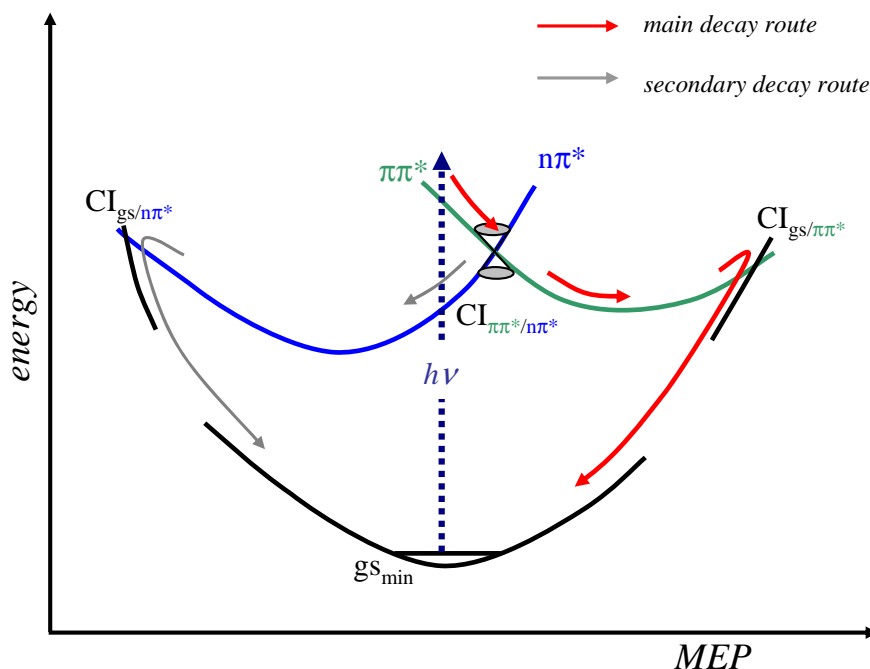


Figure 1.8: Electronic deactivation routes in C: Photo-excitation prepares the optically bright $\pi\pi^*$ state. Primarily, relaxation occurs through a direct CI of the $\pi\pi^*$ state with S_0 . En route, the $n\pi^*$ state is crossed. It is significantly populated through a ‘threefold’ degenerate CI, which leads to a bifurcation of the excited population. Dynamic processes resulting from the $n\pi^*$ state are rather slow.

1.3.2.3 Important Structural Isomers of the Natural DNA Bases

A well-known structural isomers of the nucleobase A (6-aminopurine) is its derivative 2-aminopurine (2AP). It is used as DNA fluorescence marker, because its excited-state lifetime is of the order of ≈ 2 ns and the corresponding fluorescence quantum yield is ≈ 0.66 [107, 122–126]. In its canonical form, it can pair with T in a wobble base pairs motif, whereas it pairs with C in the imino tautomeric form. It is commonly used in time-resolved spectroscopy to elucidate solvation dynamics or environmental effects, as its fluorescence intensity, maximum fluorescence wavelength, and shape of the fluorescence envelope are sensitive to changes in the local conformation and solvation shell [123, 127–132]. Thus, 2AP has been used to monitor nucleobase stacking interactions, which will be discussed in some detail below.

Alkylation of the heterocycles has been found in majority to have only a small effect on the excited-state dynamics of the DNA bases [7]. The macroscopic effect of methylation is of tremendous biological relevance: Methylated DNA sequences control significant processes of gene recognition, regulation and genetic imprinting. Distinct methylation patterns allow cells to identify foreign gene sequences, to distinguish between the master copy and the replicated strand during DNA synthesis, and to activate and inactivate certain DNA domains in order to regulate gene expression [133]. This leads to crucial medical importance, as methylated DNA bases are accumulated in tumor cells. Environmental conditions can change the cell’s methylation archetype dramatically, which consecutively leads to serious (for example photochemically induced) DNA damage. Some selected methylated nucleobases might therefore show different responses to photo-activation and other relaxation mechanisms than unmethylated nucleobases do.

An outstanding example is the A derivative N^6, N^6 dimethyladenine (DMA), a doubly methylated nucleobase, which is naturally occurring in RNA. DMA was found to be a molecule that exhibits so-called ‘dual fluorescence’ [134–137]. In addition to the A-like UV fluorescence, it shows a second red-shifted fluorescence band with a Stokes shift of more than $15\,000\text{ cm}^{-1}$. The red-emitting region of the PES can only be reached after excitation in the UV and, thus, an excited-state transformation, which possibly involves an excited-state charge transfer (CT) reaction accompanied by a substantial conformational rearrangement. First femtosecond fluorescence experiments in aqueous solution were performed in our work group [137] and revealed that the excited state dynamics extracted from the UV emission band show a behavior similar to the parent molecule A, but the dynamics in the red-shifted part were found to be much longer-lived. This study was completed only recently by complementary work on DMA in water as well as in dioxane in a wide excitation (λ_{pump}) and fluorescence (λ_{fl}) wavelength range (*Chapters 3 and 4*). Global fits to the measured fluorescence decay curves revealed, practically independent of λ_{pump} , that molecular relaxation processes occurred on five well-defined time scales, ranging from the sub-100 fs region up to ≥ 1 ns at the longest λ_{fl} , in total contrast to the parent molecule A [11, 12].

1.3.3 Nucleobase Aggregates

1.3.3.1 Hydrogen-Bonded Nucleobase Pairs

Practically all data available on single hydrogen-bonded DNA base pairs stem from gas phase experiments [94, 138–145], which have mostly been carried out on the G···C base pair. Interestingly, the measured experimental spectra lack fingerprints of the naturally occurring WC binding motif [94, 138–141]. Abo-Riziq *et al.* observed spectrally well-resolved features in IR/UV hole-burning experiments on G and C containing sample mixtures, assigned them to non-WC base pairs, and deduced that the electronic relaxation is rather slow. Very weak and unstructured broad bands were assumed to originate from the WC structure and it was concluded that rapid internal conversion accounts for their spectral envelopes [141].

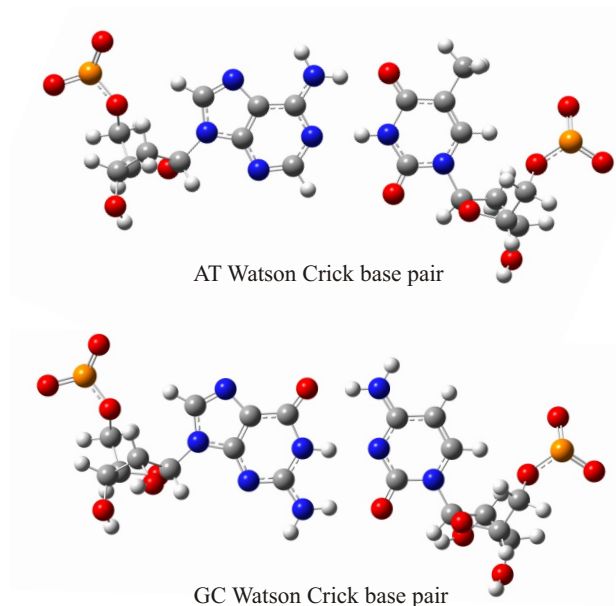


Figure 1.9: Complementary Watson-Crick (WC) nucleobase pairs. Top: A···T Watson-Crick base pair. Bottom: G···C Watson-Crick base pair.

Combined time-resolved and theoretical studies on a 2AP model cluster as well as on A and T containing dimers were performed in the molecular beam by femtosecond mass spectrometry [142–145]. An enhanced excited-state decay was found for the model system. It was suggested from theory that suitable CIs connect the locally excited $\pi\pi^*$ state with the electronic ground state via a $\pi\pi^*$ CT state, which is substantially stabilized by an accompanying single proton transfer [142]. This coupled electron-proton transfer mechanism was later assigned to the G···C and A···T WC base pairs [141, 146–151]. Gas phase calculations on the G···C WC base pair revealed the possibility of a double proton transfer, which was not observed on calculations in water or on the base pair embedded in DNA [149]. Double proton transfer was found to play a role in the 7-azaindole dimer, another model system for DNA base pairs [152–154].

Until recently, no experimental data were available on the electronic deactivation of single hydrogen-bonded DNA base pairs in solution. Such motifs are unstable in aqueous solution, where they prefer to form nucleobase stacks. Thus, specially protected nucleobases were synthesized, which enforce the formation of well-defined hydrogen-bonded DNA base pairs in aprotic solution [155–158]. The publications listed in *Chapters 5* and *6* delivered the first experimental approach to investigate the hydrogen-bonded G···C WC base pair in the bulk phase [10, 13]. Experiments were carried out in chloroform (CHCl₃), an aprotic and only slightly polar solvent. CHCl₃ on the one hand fulfills the above requirements and additionally mimics the surrounding of a nucleobase pair in DNA, as the dielectric constant of CHCl₃ matches that inside DNA quite well [159]. The obtained results give the first direct evidence for the acceleration of the excited-state decay on base pair formation of G with C and confirm the theoretically proposed coupled electron-proton transfer process. Higher hydrogen-bonded aggregates of C and G have been studied as well (*Chapters 8* and *9*, [14, 15]). Related preliminary experiments have been carried out also on the A···T and 2AP···T base pairs [17].

1.3.3.2 Nucleobase Stacks

Data on minimal model systems of nucleobase stacks were obtained from experiments on very short single stranded DNA oligomers and non-covalently bounded dimeric π -stacked assemblies on 2AP-enclosing di- and trimers, which were carried out to elucidate CT processes in DNA building blocks [107, 123–132]. The excited-state behavior of mostly A-containing diribonucleoside monophosphates have been studied very recently by means of femtosecond transient absorption spectroscopy [160]. Long-lived excited-state lifetimes of the order of $\approx 2 - 100$ ps have been observed and have been attributed to interbase CT states, resulting from electron transfer between two π -stacked nucleobase neighbors. It was assumed that the observed long-lived decay rates are correlated with the energy of the charge separated (\equiv exciplex/excimer) states, which were estimated from the gas phase ionization potentials and electron affinities of the involved bases.

1.3.4 DNA Oligomers and Polymers

Femtosecond fluorescence and transient absorption measurements have been carried out on short DNA oligo- and polymers, which were synthesized from 8 to ≥ 200 nucleobases. Tracts of pure A or T repeats and alternating A and T containing sequences dominate the available data [9, 111, 161–167], whereas studies on a pure C homopolymer or on alternating d(GC) containing oligo- and polymers are fragmentary [9, 168–170]. It was a general observation that the ground state recovery in DNA multimers is significantly slower than in monomeric nucleobases. Multiple excited-state decays were observed, which ranged from monomer-like timescales (sub-picosecond) to drastically elongated contributions of the order of hundreds of picoseconds and even nanoseconds [9, 162–166]. The latter significantly

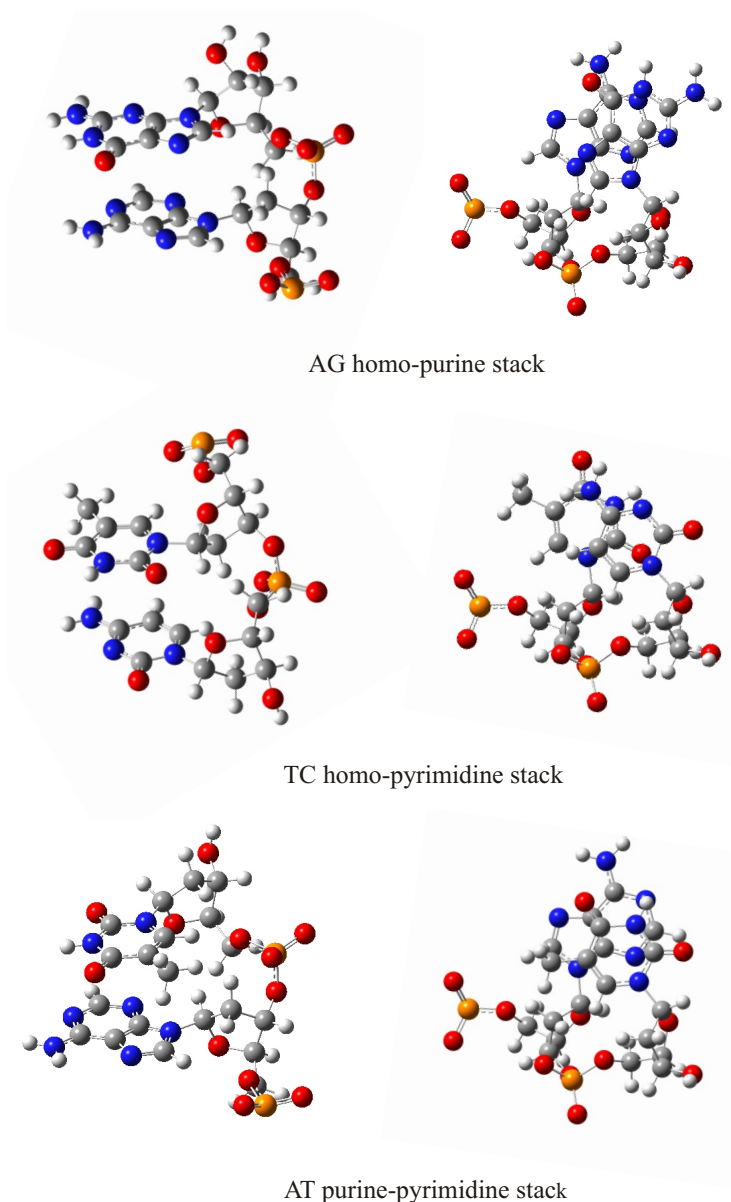


Figure 1.10: Side (left) and top views (right) of nucleobase stacks in B-DNA conformation. Strong stacking can be observed in the purine containing assemblies, as the heterocycles are practically arranged face-to-face, while pure pyrimidine stacks (middle) do not show significant overlap of the ring systems.

($\geq 34 - 41\%$) contribute to signals in femtosecond transient absorption spectroscopy and thus, were attributed to dark, charge-separated exciplex or excimer states, similar to those obtained in π -stacked dinucleotides [160, 166]. The former ultrafast decay components have been explained on the one hand by dynamic disorder within the investigated strands, which might lead to base flip-outs [166]. Besides, exciton theory was used to describe the observed fast timescales [163–165, 171, 172].

The first substantial systematic study of short single- and double-stranded DNA oligomers with a length of 20 nucleobases was published a short time ago in the context of this *Thesis* (*Chapter 10*, [9]). The strategy was to investigate the fluorescence decay times of ‘pure’ and

thus atypical homopurine and homopyrimidine runs in comparison to highly mixed base sequences. Pure A or T-containing single strands and their respective d(A)·d(T) duplexes were used as references and, successively, every fifth, third or second base was substituted by d(G) or d(C), respectively, so that finally the pure d(G)·d(C) structure was studied. These experiments unraveled the strong sequence dependent photostability of DNA single and double strands and further highlighted an additional, strong dependence of the excited-state decay on higher-order structure effects. The discovery that the contributions of nucleobase stacking dynamics or hydrogen-bonding dynamics do have variable influences on the relaxation dynamics in dependence of the base sequence can be considered as a benchmark for further time-resolved studies on the photostability of DNA.

A connection between DNA and exciton theory has been established quite early in terms of cooperative structural effects [5], but it was not until today that dynamic exciton theory is used to describe photo-induced processes in the DNA. The advances are due to the developments in ultrafast spectroscopy and to the progress in computational techniques. Applying exciton theory relies on the close similarity of the highly ordered tubular-like secondary structure of DNA to semiconducting carbon nanotubes or columnar liquid crystals [173, 174].

Early approaches have been made by using a Frenkel exciton description, in which the excited states of the full system are constructed as linear combinations of the local, monomeric excited states, considering excitation as a coherent hopping process between neighboring bases [175–179]. Towards these ends, the excited states of DNA can be derived from an eigenvalue problem, in which diagonal entries in the Hamiltonian matrix represent the monomer-associated eigenstates of the system and the off-diagonal elements correspond to the respective electronic coupling terms. It has been found that the optically bright $\pi\pi^*$ electronic transitions of DNA nucleobases manifest a long-range Coulomb coupling, which is not restricted to the nearest-neighbors, but appears as an intra-chain, face-to-face and cross-coupling between the complementary DNA strands [171, 172, 180–189]. The extent of delocalization was estimated to range between 2 – 6 nucleobases and it was discussed, whether this number is reduced through relaxation [184]. Consequently, the lowest energy UV absorption band of DNA is supposed to be made up by exciton states, in which the oscillator strength is distributed over a small number of eigenstates. It was determined that the highest oscillator strength is carried by the upper excitonic states, which causes a very slight blue-shift of a few nanometers of the absorption wavelength maximum, but no pronounced absorption band splitting was observable [171, 172, 180, 184, 185].

Considerable debate has been carried out, whether Frenkel exciton theory alone is sufficient to describe the electronic coupling in DNA or whether CT processes are likely to be involved [162, 190]. Charge separation in DNA results from the redox potentials of the nucleobase chromophores and as these do not differ dramatically, orbital overlap of adjacent nucleobases is needed. Thus, charge separation is restricted to the nearest neighbors in the DNA and the delocalization length is not more than two nucleobases. These CT states

do carry rather low oscillator strength and are not responsible for the bright absorption of the DNA chromophores. CT states relevant to DNA have been calculated for nucleobase dimers and oligomers very recently [181, 184–187, 189, 191].

1.4 Scope and Contents of the Present *Thesis*

Within the scope of this *Thesis*, a number of results were obtained, which contribute fundamentally to the state-of-the-art knowledge about the photodynamic behavior of DNA and its building blocks. A comprehensive experimental program was initiated to systematically study the photophysical and photochemical dynamics of the important structural subunits of DNA following a successful bottom-up strategy.

The excited-state lifetimes and corresponding relaxation pathways of selected isolated nucleobase derivatives, of single hydrogen-bonded DNA base pairs and of specific short single- and double-stranded DNA oligomers with different base sequences and lengths, ranging between 3 – 20 nucleobases, were studied. All investigations were carried out with the femtosecond UV fluorescence up-conversion technique, which directly monitors the depopulation of the optically bright excited states. Because of the high sensitivity of the setup, even optically dark states, which carry low oscillator strength and which might be involved as intermediate excited states, became observable, at least in a region where these states are coupled to the nearby bright states.

A detailed description of the femtosecond UV fluorescence up-conversion method is given in *Chapter 2*. Additionally, a number of static spectroscopic methods like UV absorption, fluorescence, circular dichroism and FTIR spectroscopy were used to characterize the investigated sample systems.

Chapters 3 to *11* represent the ‘Results and Discussion’ part of the present *Thesis*, which is given by the scientific papers published so far. Unpublished supporting material can be found in the *Appendix*. The ‘Results and Discussion’ part is organized as follows:

Chapters 3 and *4* deal with N^6,N^6 -dimethyladenine (DMA), which is a structural isomer of the naturally occurring nucleobase A [11, 12]. It differs from its parent molecule only by a double methylation of the exocyclic amino group. Although this is just a slight modification, it has a tremendous effect on the excited-state dynamics. Namely, DMA is a molecule that shows so-called dual fluorescence: Aside from the A-like UV fluorescence band around $\lambda_{fl} \approx 330$ nm, a second solvent-dependent red-shifted band, centered around $\lambda_{fl} \approx 450 - 550$ nm, is observed. The position of this band depends on the solvent. The excited-state dynamics of DMA has been investigated for a number of different excitation (λ_{pump}) and fluorescence wavelengths (λ_{fl}) and a modified four-state model has been established to explain the observed photodynamics. Dynamic processes, monitored in the UV region of the fluorescence spectrum, were found to take place on a timescale of several hundred femtoseconds, whereas processes observable in the red turned out to be dominated by long-lived fluorescence decay components of up to 1.4 ns.

Chapters 5 to 9 are concerned with the first-time experimental investigations of hydrogen-bonded WC and non-WC base pairs and higher H-bonded aggregates in solution [10, 13–15]. Commercially available nucleobases, which are exclusively soluble in water or short-chain alcohols, do normally not form such motifs in the respective solutions. Thus, a special sample design was required. Towards these ends, hydrophobic (2'),3',5'-*tert*-butyldimethylsilyl-(deoxy)nucleosides were synthesized, which form well-defined hydrogen-bonded nucleobase pairs in aprotic solvents like chloroform. Furthermore, higher H-bonded aggregates were observed in *n*-hexane. The dynamics, structures and association equilibria of the respective assemblies were elucidated via a number of different experiments.

The time-resolved results obtained in the first femtosecond UV fluorescence up-conversion experiment, which are given in *Chapter 5*, unambiguously demonstrated that the excited-state relaxation is dramatically accelerated on complementary hydrogen bonding in the G···C WC base pair. Moreover, the results obtained from a second round of measurements, which are described in *Chapter 6*, indicated a global deactivation pathway, which is accessible after excitation close to the electronic origin and high above. The fluorescence decay observed for the G···C WC base pair was compared to the underlying free G and C, and to their homodimers formed at suitable concentrations by self-association. Thus, these studies provide additional information on the pump-wavelength dependent deactivation mechanisms in these compounds, which have even been missing for the monomers so far. *Chapter 7* refers to the published part of the characterization procedure of the synthesized nucleosides and their dimers, including experimental and theoretical approaches [157]. The corresponding so far unpublished proceedings can be found in the *Appendix*.

Higher hydrogen-bonded aggregates of C and G, which represent model systems of DNA triplexes and quadruplexes, are investigated in *Chapters 8 and 9*. Here, the outstanding complex was a hydrogen-bonded G tetrad, which is the basic subunit of the well-known G quadruplex DNA structure, found in telomeres and centromeres. A reverse-Hoogsteen pairing motif leads to the cyclic G structure. Interestingly, the excited-state lifetime of this structure was almost two orders of magnitude longer than in the G dimer.

First results on similar experiments carried out on the A···T and 2AP···T base pairs can be found in the *Appendix*.

Studies on DNA oligomers are summarized in *Chapter 10*. A benchmarking study on the sequence dependent photostability of short DNA single strands, made up by homopurines or homopyrimidines, respectively, and of the corresponding DNA duplexes was performed on a series of DNA 10mers to 20mers with varying base sequences. As stated above, the electronic structure of these DNA mimics is not as simple as in the free nucleobases, as it is overruled by the higher-order structure of DNA. In general, two sequence-dependent impacts were pointed out: (i) Highly mixed base sequences ensured short excited-state lifetimes, whereas extraordinarily long electronic lifetimes were obtained for 'pure', atypical sequences (primary structure effect). (ii) It was found that hydrogen-bonding dynamics compete with π -stacking interactions (secondary structure effect). The relaxation in

d(A)···d(T) repeats was found to be mainly controlled by stacking, but a coupled electron-proton-transfer seems to account significantly for the relaxation dynamics in d(G)···d(C)-rich sequences, especially in alternating runs.

In order to determine the effects of base stacking and base pair formation in a molecule of manageable size, which is amenable for theoretical studies, a short self-complementary oligonucleotide loop was investigated in ongoing studies (see *Chapter 11*, [16]). It was made up by a triple run of G at the 5' end, which was separated from a repeat of three complementary C at the 3' extension by a suitable, photochemically inert linker. Duplex formation was affirmed via stationary UV absorption and CD spectroscopy as well as in multi-dimensional NMR experiments. As the observed dynamics reproduce those observed for larger 'standard' DNA double helices (i.e., the dG₁₀·dC₁₀ duplex, see *Chapter 10*, [9]), the investigated self-complementary oligomer loop might serve as a model system for the photodynamics of DNA.

The relevance of the findings on the investigated sample systems is discussed in more detail and in a broader context in the concluding discussion in *Chapter 11*.

References and Notes

- [1] O. T. Avery, C. M. MacLeod, M. MacCarty, *J. Exp. Med.* **79**, 137 (1944).
- [2] J. D. Watson, F. H. C. Crick, *Nature* **171**, 737 (1953).
- [3] M. T. Ross *et al.*, *Nature* **441**, 315 (2005).
- [4] W. Saenger, *Principles of Nucleic Acid Structure* (Springer, New York, 1983).
- [5] V. A. Bloomfield, D. M. Crothers, I. Tinoco, *Nucleic Acids: Structures, Properties and Functions* (University Science Books, Sausalito, 2000).
- [6] G. M. Blackburn, M. J. Gait, D. Loakes, D. M. Williams, eds., *Nucleic Acids in Chemistry and Biology* (The Royal Society of Chemistry, Cambridge, 2006).
- [7] C. E. Crespo-Hernández, B. Cohen, P. M. Hare, B. Kohler, *Chem. Rev.* **104**, 1977 (2004).
- [8] D. Markovitsi *et al.*, *Nature* **441**, E7 (2006).
- [9] N. K. Schwalb, F. Temps, *Science* **322**, 243 (2008).
- [10] N. K. Schwalb, F. Temps, *J. Am. Chem. Soc.* **129**, 9272 (2007).
- [11] N. K. Schwalb, F. Temps, *Springer Series of Chemical Physics, in press* **113** (2009).
- [12] N. K. Schwalb, F. Temps, *J. Phys. Chem. A, accepted and in press* (2009).
- [13] N. K. Schwalb, F. Temps, *J. Phys. Chem. A, submitted* (2009).
- [14] N. K. Schwalb, F. Temps, *Angew. Chem., submitted* (2009).
- [15] N. K. Schwalb, F. Temps, *J. Photochem. Photobiol. A, submitted* (2009).
- [16] N. K. Schwalb, J. Kleber, F. Sönnichsen, F. Temps, *Phys. Chem. Chem. Phys., manuscript in preparation* (2009).
- [17] N. K. Schwalb, F. Temps, *unpublished results* (2009).
- [18] R. Stefl *et al.*, *J. Mol. Bio.* **307**, 513 (2001).
- [19] J. Kypr, M. Fialová, J. Chládková, M. Tumorová, M. Vorlicková, *Eur. Biophys. J.* **30**, 555 (2001).
- [20] L. Trantirek *et al.*, *J. Mol. Biol.* **297**, 907 (2000).
- [21] J. Kypr, M. Vorlicková, *Biopolymers* **67**, 275 (2002).
- [22] B. McClintock, *Science* **226**, 792 (1984).
- [23] M. Mills *et al.*, *Current Medicinal Chemistry - Anti-Cancer Agents* **2**, 627 (2002).
- [24] G. Witzany, *Biosemitotics* **1**, 191 (2008).
- [25] S. Arrhenius, *Z. Physik. Chem.* **4**, 226 (1889).
- [26] M. G. Evans, M. Polanyi, *Trans. Faraday Soc.* **31**, 875 (1935).
- [27] H. Eyring, *J. Chem. Phys.* **3**, 107 (1935).

- [28] R. G. W. Norrish, G. Porter, *Nature* **164**, 658 (1949).
- [29] D. R. Herschbach, *Angew. Chem.* **99**, 1251 (1987).
- [30] Y. T. Lee, *Angew. Chem.* **99**, 967 (1987).
- [31] J. C. Polanyi, *Angew. Chem.* **99**, 981 (1987).
- [32] H. Weber, G. Herziger, *Laser - Grundlagen und Anwendungen* (Physik Verlag, Weinheim, 1972), first edn.
- [33] P. M. W. French, *Rep. Prog. Phys.* **58**, 169 (1995).
- [34] S. L. Shapiro, *Ultrashort Light Pulses* (Springer-Verlag, Berlin, Heidelberg, New York, 1977).
- [35] C. Rullière, *Femtosecond Laser Pulses, Principles and Experiments* (Springer-Verlag, Berlin, Heidelberg, New York, 1998).
- [36] M. Dantus, M. J. Rosker, A. H. Zewail, *J. Chem. Phys.* **87**, 2395 (1987).
- [37] A. H. Zewail, *Femtochemistry: Ultrafast Dynamics of the Chemical Bond* (World Scientific, 1994).
- [38] J. Manz, *Femtosecond Chemistry* (VCH Verlagsgesellschaft, Weinheim, 1995).
- [39] A. H. Zewail, *J. Phys. Chem. A* **104**, 1089 (2000).
- [40] F. C. De Schryver, S. De Feyter, G. Schweitzer, *Femtochemistry* (VCH Verlagsgesellschaft, Weinheim, 2001).
- [41] S. Mukamel, *Principles of Nonlinear Optics and Spectroscopy* (Oxford University Press, New York, 1995).
- [42] E. T. J. Nibbering, T. Elsaesser, *Chem. Rev.* **104**, 1887 (2004).
- [43] M. Cho, *Chem. Rev.* **108**, 1331 (2008).
- [44] A. Cavalleri, R. W. Schoenlein, *Topics in Applied Physics: Ultrafast Dynamical Processes in Semiconductors* **92**, 309 (2004).
- [45] M. Himmelhaus, F. Eisert, M. Buck, M. Grunze, *J. Phys. Chem. B* **104**, 576 (2000).
- [46] D. L. Nelson, M. M. Cox, *Lehninger Biochemie* (Springer Verlag Berlin, Heidelberg, 2001).
- [47] R. P. Sinha, D.-P. Hader, *Photochem. & Photobiol. Sciences* **1**, 225 (2002).
- [48] C. Mathews, K. V. Holde, *Biochemistry* (Benjamin Cummings Publication, San Francisco, 1990).
- [49] J.-L. Ravanat, T. Douki, J. Cadet, *J. Photochem. Photobiol. B* **63**, 88 (2001).
- [50] J. Blais, T. Douki, P. Vigny, J. Cadet, *Photochem. Photobiol.* **59**, 402 (1994).
- [51] L. Blancafort, A. Migani, *J. Am. Chem. Soc.* **129**, 14550 (2007).
- [52] W. J. Schreier *et al.*, *Science* **315**, 625 (2007).
- [53] M. Boggio-Pasqua, G. Groenhof, L. V. Schaefer, H. Grubmüller, M. A. Robb, *J. Am. Chem. Soc.* **129**, 10996 (2007).

- [54] M. R. Holman, T. Ito, S. E. Rokita, *J. Am. Chem. Soc.* **129**, 6 (2007).
- [55] S. Marguet, D. Markovitsi, *J. Am. Chem. Soc.* **127**, 5780 (2005).
- [56] M. V. Berry, M. Wilkinson, *Proc. R. Soc. Lond. A* **392**, 15 (1984).
- [57] M. Klessinger, J. Michl, *Excited States and Photochemistry of Organic Molecules* (VCH Verlagsgesellschaft, Weinheim, 1995).
- [58] D. R. Yarkony, *Rev. Mod. Phys.* **68**, 985 (1996).
- [59] W. Domcke, D. R. Yarkony, H. Koeppele, eds., *Conical Intersections: Electronic Structure, Dynamics & Spectroscopy* (World Scientific, Singapore, 2004).
- [60] F. Hund, *Z. Physik* **40**, 742 (1927).
- [61] J. von Neumann, E. P. Wigner, *Z. Physik* **30**, 467 (1929).
- [62] L. D. Landau, E. M. Lifshitz, J. B. Sykes, *Quantum Mechanics: Non-Relativistic Theory* (Mir Editions, 1981).
- [63] J. T. Yardley, *Introduction to Molecular Energy Transfer* (Academic Press, 1980).
- [64] P. R. Callis, *Annu. Rev. Phys. Chem.* **34**, 329 (1983).
- [65] A. A. Oraevsky, A. V. Sharkov, D. N. Nikogosyan, *Chem. Phys. Lett.* **83**, 276 (1981).
- [66] T. Häupl, C. Windolph, T. Jochum, O. Brede, R. Hermann, *Chem. Phys. Lett.* **280**, 520 (1997).
- [67] A. Reuther, H. Iglev, R. Laenen, A. Lauberau, *Chem. Phys. Lett.* **325**, 360 (2000).
- [68] A. L. Sobolewski, W. Domcke, *Eur. Phys. J. D* **20**, 369 (2002).
- [69] S. Perun, A. L. Sobolewski, W. Domcke, *Chem. Phys.* **313**, 107 (2005).
- [70] S. Perun, A. L. Sobolewski, W. Domcke, *J. Am. Chem. Soc.* **127**, 6257 (2005).
- [71] S. Perun, A. L. Sobolewski, W. Domcke, *J. Phys. Chem. A* **110**, 13238 (2006).
- [72] L. Blancafort, M. A. Robb, *J. Phys. Chem. A* **108**, 10609 (2004).
- [73] L. Blancafort, B. Cohen, P. M. Hare, B. Kohler, M. A. Robb, *J. Phys. Chem. A* **109**, 4431 (2005).
- [74] L. Blancafort, *J. Am. Chem. Soc.* **128**, 210 (2006).
- [75] C. M. Marian, *J. Chem. Phys.* **122**, 104314 (2005).
- [76] C. M. Marian, *J. Phys. Chem. A* **111**, 1545 (2007).
- [77] C. M. Marian, M. Kleinschmidt, J. Tatchen, *Chem. Phys.* **347**, 346 (2008).
- [78] L. Serrano-Andrés, M. Merchán, A. C. Borin, *Chem. Eur. J.* **12**, 6559 (2006).
- [79] L. Serrano-Andrés, M. Merchán, A. C. Borin, *J. Am. Chem. Soc.* **130**, 2473 (2008).
- [80] K. A. Kistler, S. Matsika, *J. Phys. Chem. A* **111**, 2650 (2007).
- [81] K. A. Kistler, S. Matsika, *J. Phys. Chem. A* **111**, 8708 (2007).

- [82] S. Matsika, *J. Phys. Chem. A* **108**, 7584 (2004).
- [83] S. Matsika, *J. Phys. Chem. A* **109**, 7358 (2005).
- [84] A. L. Sobolewski, W. Domcke, *Chem. Phys.* **259**, 181 (2000).
- [85] H. Chen, S. Li, *J. Phys. Chem. A* **109**, 8443 (2005).
- [86] H. Chen, S. Lu, *J. Chem. Phys.* **124**, 154315 (2006).
- [87] A. L. Sobolewski, W. Domcke, C. Dedonder-Lardeux, C. Jouvet, *Phys. Chem. Chem. Phys.* **4**, 1093 (2002).
- [88] J. Wei, A. Kuczmann, J. Riedel, F. Renth, F. Temps, *Phys. Chem. Chem. Phys.* **5**, 315 (2003).
- [89] J. Wei, J. Riedel, A. Kuczmann, F. Renth, F. Temps, *Faraday Discuss.* **127**, 267 (2004).
- [90] N. J. Kim *et al.*, *J. Chem. Phys.* **113**, 10051 (2000).
- [91] D. C. Lührs, J. Viallon, I. Fischer, *Phys. Chem. Chem. Phys.* **3**, 1827 (2001).
- [92] C. Plützer, E. Nir, M. S. de Vries, K. Kleinermanns, *Phys. Chem. Chem. Phys.* **3**, 5466 (2001).
- [93] E. Nir, K. Kleinermanns, L. Grace, M. S. de Vries, *J. Phys. Chem. A* **105**, 5106 (2001).
- [94] E. Nir, C. Plützer, K. Kleinermanns, M. de Vries, *Eur. Phys. J. D* **2002**, 317 (2002).
- [95] C. Plützer, K. Kleinermanns, *Phys. Chem. Chem. Phys.* **4**, 4877 (2002).
- [96] N. J. Kim, H. Kang, Y. D. Park, S. K. Kim, *Phys. Chem. Chem. Phys.* **6**, 2802 (2004).
- [97] I. Hünig *et al.*, *Chem. Phys. Chem.* **5**, 1427 (2004).
- [98] Y. Lee, M. Schmidt, K. Kleinermanns, B. Kim, *J. Phys. Chem. A* **110**, 11819 (2006).
- [99] S. Ullrich, T. Schulz, M. Z. Zgierski, A. Stolow, *J. Am. Chem. Soc.* **126**, 2262 (2004).
- [100] S. Ullrich, T. Schulz, M. Z. Zgierski, A. Stolow, *Phys. Chem. Chem. Phys.* **6**, 2796 (2004).
- [101] H. Satzger, D. Townsend, A. Stolow, *Chem. Phys. Lett.* **430**, 144 (2006).
- [102] H. Satzger *et al.*, *Proc. Nat. Acad. Sci. USA* **103**, 10196 (2006).
- [103] C. Canuel *et al.*, *J. Chem. Phys.* **122**, 074316 (2005).
- [104] J.-M. Pecourt, J. Peon, B. Kohler, *J. Am. Chem. Soc.* **122**, 9348 (2000).
- [105] J.-M. Pecourt, J. Peon, B. Kohler, *J. Am. Chem. Soc.* **123**, 10370 (2001).
- [106] B. Cohen, P. M. Hare, B. Kohler, *J. Am. Chem. Soc.* **125**, 13594 (2003).
- [107] J. Peon, A. H. Zewail, *Chem. Phys. Lett.* **348**, 255 (2001).
- [108] D. Onidas, D. Markovitsi, S. Marguet, T. Gustavsson, *J. Phys. Chem. B* **106**, 11367 (2002).
- [109] T. Gustavsson, A. Sharonov, D. Onidas, D. Markovitsi, *Chem. Phys. Lett.* **356**, 49 (2002).
- [110] T. Pancur, N. K. Schwalb, F. Renth, F. Temps, *Chem. Phys.* **313**, 199 (2005).

- [111] W.-M. Kwok, C. Ma, D. L. Phillips, *J. Am. Chem. Soc.* **128**, 11894 (2006).
- [112] E. Nir, C. Janzen, P. Imhof, K. Kleinermanns, M. S. de Vries, *J. Chem. Phys.* **115**, 4604 (2001).
- [113] T. Gustavsson, A. Sharonov, D. Markovitsi, *Chem. Phys. Lett.* **351**, 195 (2002).
- [114] R. J. Malone, A. M. Miller, B. Kohler, *Photochem. Photobiol.* **77**, 158 (2003).
- [115] A. Sharonov, T. Gustavsson, V. Carre, E. Renault, D. Markovitsi, *Chem. Phys. Lett.* **380**, 173 (2003).
- [116] T. Gustavsson, N. Sarkar, E. Lazzarotto, D. Markovitsi, R. Improta, *Chem. Phys. Lett.* **429**, 551 (2006).
- [117] T. Gustavsson *et al.*, *J. Am. Chem. Soc.* **128**, 607 (2006).
- [118] L. Blancafort, A. Migani, *J. Photochem. Photobiol. A* **190**, 283 (2007).
- [119] P. M. Hare, C. E. Crespo-Hernández, B. Kohler, *Proc. Nat. Acad. Sci. USA* **104**, 435 (2007).
- [120] C. M. Marian, F. Schneider, M. Kleinschmidt, J. Tatchen, *Eur. Phys. J. D* **20**, 357 (2002).
- [121] P. M. Hare, C. E. Crespo-Hernandez, B. Kohler, *J. Phys. Chem. B* **110**, 18641 (2006).
- [122] D. C. Ward, E. Reich, L. Stryer, *J. Biol. Chem.* **244**, 1228 (1969).
- [123] S. K. Pal, J. Peon, A. H. Zewail, *Chem. Phys. Lett.* **363**, 57 (2002).
- [124] R. K. Neely, A. C. Jones, *J. Am. Chem. Soc.* **128**, 15952 (2006).
- [125] O. J. G. Somsen, V. A. Hoek, H. Amerongen, *Chem. Phys. Lett.* **402**, 61 (2005).
- [126] J. M. Jean, K. B. Hall, *Biochemistry* **43**, 10277 (2004).
- [127] C. Wan *et al.*, *Proc. Nat. Acad. Sci. USA* **96**, 6014 (1999).
- [128] S. O. Kelley, J. K. Barton, *Science* **283**, 375 (1999).
- [129] C. Wan, T. Fiebig, O. Schiemann, J. K. Barton, A. H. Zewail, *Proc. Natl. Acad. Sci. USA* **97**, 14052 (2000).
- [130] J. M. Jean, B. P. Krueger, *J. Phys. Chem. B* **110**, 2899 (2006).
- [131] E. Y. M. Bonnist, A. C. Jones, *Chem. Phys. Chem.* **9**, 1121 (2008).
- [132] N. N. Degtyareva, M. J. Reddish, B. Sengupta, J. T. Petty, *Biochemistry* **48**, 2340 (2009).
- [133] R. Jaenisch, A. Bird, *Nature Genetics* **33**, 245 (2003).
- [134] B. Albinsson, *J. Am. Chem. Soc.* **119**, 6369 (1997).
- [135] J. Andreásson, A. Holmén, B. Albinsson, *J. Phys. Chem. B* **103**, 9782 (1999).
- [136] A. B. J. Parusel, W. Rettig, K. Rotkiewicz, *J. Phys. Chem. A* **106**, 2293 (2002).
- [137] N. K. Schwalb, F. Temps, *Phys. Chem. Chem. Phys.* **8**, 5229 (2006).
- [138] E. Nir, K. Kleinermanns, M. S. de Vries, *Nature* **408**, 949 (2000).

- [139] E. Nir, C. Janzen, P. Imhof, K. Kleineremanns, M. S. de Vries, *Phys. Chem. Chem. Phys.* **4**, 740 (2002).
- [140] E. Nir, C. Janzen, P. Imhof, K. Kleineremanns, M. S. de Vries, *Phys. Chem. Chem. Phys.* **4**, 732 (2002).
- [141] A. Abo-Riziq *et al.*, *Proc. Nat. Acad. Sci. USA* **10**, 20 (2005).
- [142] T. Schultz *et al.*, *Science* **306**, 1765 (2004).
- [143] E. Samoylova *et al.*, *J. Am. Chem. Soc.* **127**, 1782 (2005).
- [144] E. Samoylova *et al.*, *J. Am. Chem. Soc.* **128**, 15652 (2006).
- [145] A. Samoylova, T. Schultz, I. V. Hertel, W. Radloff, *Chem. Phys.* **347**, 376 (2008).
- [146] A. L. Sobolewski, W. Domcke, *Phys. Chem. Chem. Phys.* **6**, 2763 (2004).
- [147] A. L. Sobolewski, W. Domcke, C. Hättig, *Proc. Nat. Acad. Sci. USA* **102**, 17903 (2005).
- [148] S. Perun, A. Sobolewski, W. Domcke, *J. Phys. Chem. A* **110**, 9031 (2006).
- [149] G. Groenhof *et al.*, *J. Am. Chem. Soc.* **129**, 6812 (2007).
- [150] P. R. L. Markwick, N. L. Doltsinis, J. Schlitter, *J. Chem. Phys.* **126**, 045104 (2007).
- [151] P. R. L. Markwick, N. L. Doltsinis, *J. Chem. Phys.* **126**, 175102 (2007).
- [152] T. Fiebig *et al.*, *J. Chem Phys. A* **103**, 7419 (1999).
- [153] O.-H. Kwon, A. H. Zewail, *Proc. Nat. Am. Soc.* **104**, 8703–8708 (2007).
- [154] H. Sekiya, K. Sakota, *J. Photochem. Photobiol. C* **9**, 81–91 (2008).
- [155] P. Carmona, M. Molina, A. Lasagabaster, R. Excochar, A. B. Altabef, *J. Phys. Chem.* **97**, 9519 (1993).
- [156] L. Biemann, T. Häber, D. Maydt, K. Schaper, K. Kleineremanns, *J. Chem. Phys.* **128**, 195103 (2008).
- [157] T. Michalak, N. K. Schwalb, J. Gripp, F. Temps, *Spectrochim. Acta A* (submitted, 2009).
- [158] T. Michalak, N. K. Schwalb, J. Gripp, F. Temps, *manuscript in preparation* (2009).
- [159] K. Siriwong, A. A. Voityuk, M. D. Newton, N. Rösch, *J. Phys. Chem. B* **107**, 2595 (2003).
- [160] T. Takaya, C. Su, K. de La Harpe, C. E. Crespo-Hernández, B. Kohler, *Proc. Nat. Acad. Sci. USA* **105**, 10285 (2008).
- [161] C. E. Crespo-Hernández, B. Kohler, *J. Phys. Chem. B* **108**, 11182 (2004).
- [162] I. Buchvarov, Q. Wang, M. Raytchev, A. Trifonov, T. Fiebig, *Proc. Nat. Acad. Sci. USA* **104**, 4794 (2007).
- [163] D. Markovitsi, D. Onidas, T. Gustavsson, F. Talbot, E. Lazzarotto, *J. Am. Chem. Soc.* **127**, 17130 (2005).
- [164] D. Onidas, T. Gustavsson, E. Lazzarotto, D. Markovitsi, *J. Phys. Chem. B* **111**, 9644 (2007).

- [165] D. Onidas, T. Gustavsson, E. Lazzarotto, D. Markovitsi, *Phys. Chem. Chem. Phys.* **9**, 5143 (2007).
- [166] C. E. Crespo-Hernández, B. Cohen, B. Kohler, *Nature* **436**, 1141 (2005).
- [167] C. T. Middleton *et al.*, *Annu. Rev. Phys. Chem.* **60**, 217 (2009).
- [168] B. Cohen, M. H. Larsen, B. Kohler, *Chem. Phys.* **350**, 165 (2008).
- [169] F.-A. Miannay, A. Bányász, T. Gustavsson, D. Markovitsi, *J. Am. Chem. Soc.* **129**, 14574 (2007).
- [170] C. E. Crespo-Hernández, K. de La Harpe, B. Kohler, *J. Am. Chem. Soc.* **130**, 10844 (2008).
- [171] B. Bouvier, T. Gustavsson, D. Markovitsi, P. Millié, *Chem. Phys.* **275**, 75 (2002).
- [172] B. Bouvier *et al.*, *J. Phys. Chem. B* **107**, 13512 (2003).
- [173] D. Markovitsi *et al.*, *Chem. Phys. Lett.* **306**, 163 (1999).
- [174] T. Ando, S. Uryu, *Current Topics in Solid State Physics* **6**, 173 (2009).
- [175] G. D. Scholes, K. P. Ghiggino, *J. Phys. Chem.* **98**, 4580 (1994).
- [176] G. D. Scholes, *J. Phys. Chem.* **100**, 18731 (1996).
- [177] R. D. Harcourt, K. P. Ghiggino, G. D. Scholes, S. Speiser, *J. Chem. Phys.* **105**, 1897 (1996).
- [178] A. H. Clayton, G. D. Scholes, K. P. Ghiggino, M. N. Paddon-Row, *J. Chem. Phys.* **100**, 10912 (1996).
- [179] G. D. Scholes, R. D. Harcourt, *J. Chem. Phys.* **104**, 5054 (1996).
- [180] E. Emanuele, D. Markovitsi, P. Millié, K. Zakrewska, *Chem. Phys. Chem.* **6**, 1387 (2005).
- [181] E. R. Bittner, *J. Chem. Phys.* **125**, 094909 (2006).
- [182] A. Czader, E. R. Bittner, *J. Chem. Phys.* **128**, 035101 (2008).
- [183] H.-H. Ritze, P. Hobza, D. Nachtigallová, *Phys. Chem. Chem. Phys.* **9**, 1672 (2007).
- [184] F. Santoro, V. V. Barone, R. Improta, *Proc. Nat. Acad. Sci. USA* **104**, 9931 (2007).
- [185] F. Santoro, V. Barone, R. Improta, *Chem. Phys. Chem.* **9**, 2531 (2008).
- [186] R. Improta, *Phys. Chem. Chem. Phys.* **10**, 2656 (2008).
- [187] D. Nachtigallová, P. Hobza, H. H. Ritze, *Phys. Chem. Chem. Phys.* **10**, 5689 (2008).
- [188] S. Tonzani, G. C. Schatz, *J. Am. Chem. Soc.* **130**, 7607 (2008).
- [189] A. W. Lange, J. M. Herbert, *J. Am. Chem. Soc.* **131**, 3913 (2009).
- [190] C. E. Crespo-Hernández, B. Cohen, B. Kohler, *Nature* **441**, E8 (2006).
- [191] A. W. Lange, M. A. Rohrdanz, J. M. Herbert, *J. Phys. Chem. B* **112**, 6304 (2008).

Chapter 2

Experimental Section

Although the DNA bases exhibit high cross sections for the absorption of UV light, the fluorescence quantum yields are extraordinarily low. Typically, only $\leq 0.01\%$ of the absorbed energy is released via fluorescence photons. As a consequence, a minimal number of fluorescence photons, which are distributed over all spatial angles, has to be detected. To complicate matters further, these few photons are released on an ultrafast timescale, as the excited state lifetimes of the nucleobases are of the order of some hundreds of femtoseconds. This limits the application of ‘standard’ detection techniques due to the comparatively long rise and decay times of electronic devices, which are more than an order of magnitude too slow for the fluorescence signals originating from the nucleobases.

Thus, the fluorescence detection process has to be decoupled from too slow electronic assemblies and is instead carried out optically via the pump-probe principle already introduced in *Chapter 2*. For fluorescence spectroscopy, this purely optical method is established in two different techniques, which both rely on the principle of optical gating. They are, namely, the fluorescence up-conversion and the optical Kerr gating experiment. The optical gating technique is introduced in Section 2.2.

All results of the present *Thesis* were obtained with the fluorescence up-conversion experiment. Therefore, it will be described in some detail in the following. However, in this context first steps have also been made to set up a broadband up-conversion and a Kerr gate experiment. Measurements on laser dyes, which were used as model systems, gave first signals, but the setups have to be improved further to make them applicable to low-fluorescent DNA samples or related molecules of interest. It will only be briefly commented on this techniques here.

All optical processes employed by the mentioned techniques are based on the field of nonlinear optics. The most important topics will be summarized in 2.1, but a detailed description goes beyond the scope of this *Thesis* and thus, the reader is referred to the literature [1, 2].

This chapter additionally includes in Section 2.3 the data analysis procedure applied to the fluorescence decay profiles obtained with the femtosecond fluorescence up-conversion experiment. The sample preparation is described in Section 2.4 and Section 2.5 briefly summarizes the methods of static spectroscopy, which were used to characterize the DNA samples.

2.1 Introduction to Nonlinear Optics

Light fields can exert a strong electromagnetic force on matter, as this consists of the heavy, positively charged atomic nuclei and the corresponding light, negatively charged electrons, which start to oscillate with the applied field. If the field intensities are high enough, the resulting optical phenomena cannot be described any longer with the principles of linear optics.

Instead, nonlinear components, i.e., the quadratic and cubic terms of the macroscopic electromagnetic polarization $\mathbf{P}(E)$ (where E is the electromagnetic field) can no longer be neglected. $\mathbf{P}(E)$ can be described in a Taylor series expansion [2]:

$$\mathbf{P}(E) = \epsilon_0[\chi^{(1)}\mathbf{E} + \chi^{(2)}\mathbf{E}^2 + \chi^{(3)}\mathbf{E}^3 + \dots]. \quad (2.3)$$

Here, χ is the electric susceptibility of the dielectric material, which specifies its polarizability. ϵ_0 is the vacuum permittivity.

Because of the nonlinear response to the electromagnetic field \mathbf{E} , this opens the field of nonlinear optics. $\mathbf{P}(E)$ gives rise to a number of nonlinear optical phenomena, which are commonly ranked by their order with respect to χ . The most important processes, especially those relevant for the present *Thesis* are briefly sketched in the following.

2.1.1 Optical Kerr Effect, Group Velocity Dispersion and Phase Modulation

At high electromagnetic field intensities $I(t)$, as they are achieved by fs laser pulses, the refractive index $n(\omega, I)$ of matter becomes intensity-dependent and can as well be described through a power series expansion [1]:

$$n(\omega, I) = n_0(\omega) + n_2 \cdot I(t) \dots \quad (2.4)$$

Here, $n_0(\omega) = c_0/c(\omega)$ is the refractive index known from linear optics ($c_0 \equiv$ speed of light in vacuum; $c(\omega) \equiv$ speed of light inside matter) and $n_2 \cdot I(t)$ is the nonlinear, intensity-dependent contribution. It directly affects the phase ϕ of the electromagnetic field

$$\mathbf{E}(x, t) = \mathbf{E}_0 \cos(\omega t + \mathbf{k}(\omega)x), \quad (2.5)$$

by

$$\phi = \omega t - \mathbf{k}(\omega)x = \omega \left(t - \frac{n_0(\omega)x}{c} - \frac{n_2x \cdot I(t)}{c} \right) \quad (2.6)$$

and its frequency ω by

$$\omega = \frac{d\phi}{dt} = \omega_0 - \frac{n_2x}{c} \cdot \frac{dI(t)}{dt}. \quad (2.7)$$

\mathbf{E}_0 gives the field amplitude and $|\mathbf{k}(\omega)| = \omega \cdot n(\omega, I)/c(\omega)$ is the wave vector in the propagation direction x . The described dependencies are essential for nonlinear optics, as they cause the effects of self-focusing and (self)phase modulation.

Self-focusing (\equiv optical Kerr effect (OKE) or Kerr lensing) occurs, because $n(\omega, I)$ of a powerful laser pulse is highest in the intense center areas of the beam profile. Thus, as light is refracted into the direction of the highest $n(\omega, I)$ due to Snell's law, a 'self-bundling' of the beam (n_2 is positive in normal materials) results. This creates a focusing density profile, which acts as its own driving force. Linear optical dispersion due to $dn_0/d\omega$ impedes the breakdown of the pulse. In regions of normal optical dispersion, $dn_0/d\omega$ is negative and leads to higher velocities of the red-shifted spectral components of the pulse and so

they travel ahead of the blue frequencies (up-chirp). This applies *vice versa* for anomalous dispersion (down-chirp, $dn_0/d\omega > 0$) [1, 2].

Ultrafast laser pulses are short in the time domain, but consequently, have a broad spectral distribution in the frequency domain. As the different spectral components contributing to the pulse envelope exhibit different velocities within the nonlinear medium, this causes a *temporal broadening* of the laser pulse. The phase velocities of each spectral component are summarized in the group velocity v_G , which describes the propagation of the pulse envelope through the medium. The pulse thus experiences the group velocity dispersion (GVD) [3]:

$$\text{GVD} = \frac{\partial}{\partial \omega} \cdot \left(\frac{1}{v_g} \right) = \frac{\partial^2 \mathbf{k}}{\partial \omega^2} = \frac{\lambda^3}{2\pi c^2} \cdot \frac{\partial^2 n}{\partial \lambda^2} \quad (2.8)$$

Here, v_g denotes the group velocity, defined as

$$v_g = \frac{\partial \omega}{\partial \mathbf{k}} = c \cdot \left[n(\omega) + \omega \left(\frac{\partial n(\omega)}{\partial \omega} \right) \right]^{-1}. \quad (2.9)$$

Suitable dispersive optical elements (prisms, gratings, chirped mirrors) can be used for dispersion compensation.

Due to Eq. 2.4, a laser beam, which propagates through matter, additionally causes a time-dependent modulation of $n(\omega, I)$, because of the nonlinear contribution $n_2 \cdot I(t)$. From Eqs. 2.6 and 2.7, it becomes clear that this results in a self-phase modulation (SPM) and thus, in a self-induced shift of the frequency spectrum of the traversing light wave. The frequencies in the front of the pulse are hence shifted to lower frequencies ($dI(t)/dt > 0$), while those in the back of the pulse are shifted to higher frequencies ($dI(t)/dt < 0$). This results in a *spectral broadening* of the laser pulse. Very strong spectral broadening generates supercontinuum ('white') light, which is required for frequency conversion processes (see Section 2.1.2) and widely used for broadband absorption experiments.

Other phase-sensitive techniques, which rely on Eq. 2.4 and result from a higher number of interacting waves, are the processes of cross-phase modulation (XPM) and (degenerate) four wave mixing ((D)FWM).

2.1.2 Frequency Mixing and Conversion Processes

In a suitable nonlinear medium, the parametric processes of frequency mixing and conversion occur, because the nonlinear electric polarization $\mathbf{P}(E)$ contains frequency components that are not present in the incident wave(s). If the Taylor series expansion is limited to the quadratic term ($\chi^{(2)}$ processes), $\mathbf{P}(E)$ includes, aside from the fundamental frequency ω_1 (and ω_2 in the case of two interfering light waves), additional contributions of converted frequencies. Those manifest themselves in second harmonic generation (SHG), indicated by $2\omega_1$ (and $2\omega_2$), and contributions of mixed frequencies, occurring as sum frequency generation (SFG) and difference frequency generation (DFG), represented by $\omega_1 \pm \omega_2$,

respectively:

$$\mathbf{P}^{(2)} = \epsilon_0 \chi^{(2)} [\mathbf{E}_1 \cos(\omega_1 t) + \mathbf{E}_2 \cos(\omega_2 t)]^2 \quad (2.10)$$

$$= \epsilon_0 \chi^{(2)} [\mathbf{E}_1^2 \cos^2(\omega_1 t) + \mathbf{E}_2^2 \cos^2(\omega_2 t) + 2\mathbf{E}_1 \mathbf{E}_2 \cos(\omega_1 t) \cos(\omega_2 t)] \quad (2.11)$$

$$= \epsilon_0 \chi^{(2)} \frac{1}{2} [(\mathbf{E}_1^2 + \mathbf{E}_2^2) + \mathbf{E}_1^2 \cos(2\omega_1 t) + \mathbf{E}_2^2 \cos(2\omega_2 t) + 2\mathbf{E}_1 \mathbf{E}_2 \cos[(\omega_1 + \omega_2)t] + 2\mathbf{E}_1 \mathbf{E}_2 \cos[(\omega_1 - \omega_2)t]]. \quad (2.12)$$

Anisotropic, birefringent crystals, made from β -bariumborate (BBO), lithium triborate (LBO) or potassium diphosphate (KDP) are commonly used as nonlinear media, because of their high $\chi^{(2)}$ and their high damage thresholds.

The efficiency of the converting process is most sensitive to the phase (mis)match of the incident light wave(s). For efficient frequency mixing and conversion processes, the phase mismatch has to be eliminated and, instead, a proper in-phase relationship between the interacting waves needs to be ensured. This requires the conservation of energy

$$\omega_3 = \omega_1 + \omega_2 \quad (2.13)$$

and momentum

$$\mathbf{k}_3 = \mathbf{k}_1 + \mathbf{k}_2. \quad (2.14)$$

The mismatch is given by

$$\Delta \mathbf{k} = \mathbf{k}_3(\omega_3) - \mathbf{k}_1(\omega_1) - \mathbf{k}_2(\omega_2) = \frac{n_3}{\lambda_3} - \frac{n_1}{\lambda_1} - \frac{n_2}{\lambda_2}. \quad (2.15)$$

Phase matching can be achieved by a proper choice of the polarizations of the incident wave(s) (type I or type II phase matching) and a suitable positioning, i.e., tilting, of the birefringent crystal, because the refractive index of the extraordinary wave directly depends on the relative angle α between the incident wave(s) and the optical axis of the crystal [3]

$$n_e(\alpha) = n_o \sqrt{\frac{1 + \tan^2 \alpha}{1 + (n_o/n_e)^2 \tan^2 \alpha}} \quad (2.16)$$

This, in consequence, determines the phase matching angle ϑ . If it is adjusted correctly, the phase matching condition is fulfilled and all waves experience the same refractive index and positive interference is given. However, chromatic dispersion leads to a GVD mismatch, which is the limiting factor and which determines the phase matching bandwidth. Phase matching can be achieved either in collinear or non-collinear beam geometries of the incident waves.

Fully tunable light pulses, where the target frequency can be set over a broad spectral range, rely on the process of (nonlinear) optical parametric amplification, ((N)OPA) [4]. Here, an incident weak photon (seed) traverses through the nonlinear crystal together with a pump

photon (amplifier) of much higher intensity and frequency. The latter then decomposes in an ‘inverse’ SFG process to two photons of ordinary and extraordinary polarization, named signal and idler. The frequency of the signal is commonly determined by the seed frequency, while the idler matches the difference between seed and pump energy. The intensity can be either adjusted to the signal or the idler. Usually, the seed frequencies are obtained from white light photons via supercontinuum generation in a suitable nonlinear device (e.g., glass plate) through the process of self-phase modulation. By delaying the seed light pulse in time relative to the amplifying pump pulse, different signal frequencies can be obtained.

2.2 Femtosecond Fluorescence Spectroscopy by Optical Gating

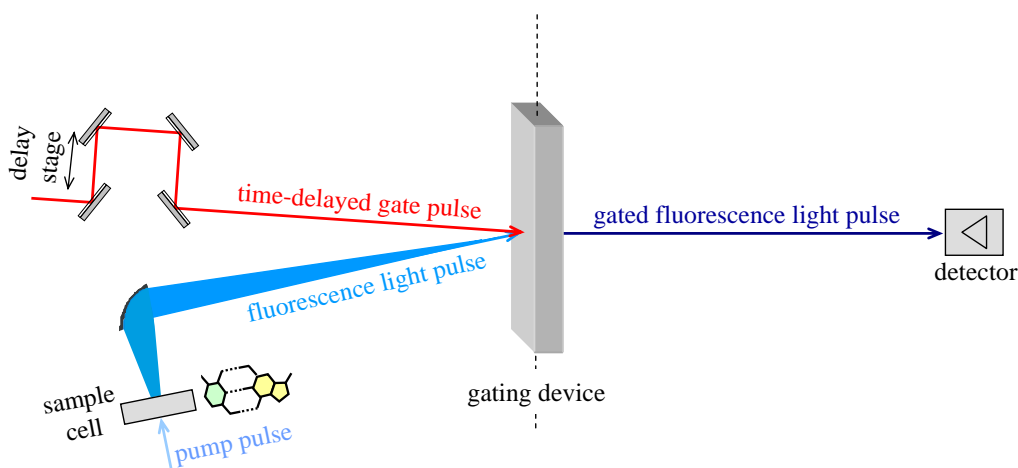


Figure 2.1: Principle of optical gating in time-resolved fluorescence spectroscopy: After photo-excitation through the pump pulse, the resulting fluorescence light pulse is injected into a gating device, which is opened by the temporal and spatial coincidence of the gate pulse. The gated fluorescence light is detected as a function of the time-delayed gate pulse.

In the transient absorption technique, the sequence of pump and probe pulse allows for a direct detection of the transmission properties of a sample solution and the corresponding population density of the involved states via the change in optical density. In contrast, in transient fluorescence experiments, the pump pulse only initiates the molecular occasion. Thus, non-directionally and incoherently emitted photons have to be correlated to the probe pulse. Therefore, an additional procedure, the so-called optical gating process, is required. Here, the generated fluorescence photons are collected in a certain spatial angle and are focused on a suitable optical gating device. The device gains its functionality only through the presence of the probe pulse, which consequently is named ‘gate’ pulse in femtosecond fluorescence experiments. It does not apply to the fluorescence photons on its own. In the device, the molecular fluorescence light pulse and the gate pulse are temporarily and spatially overlapped. As the intensity of the gate pulse is much higher than the fluorescence light, it is powerful enough to alter the optical properties of the gating medium, experienced by the bypassing fluorescence light and thus, it serves as the

gate opener. Therefore, femtosecond fluorescence spectroscopy can be considered rather as ‘pump-gate’ than as pump-probe spectroscopy. The gated fluorescence light, which can pass the optical gating device for the duration of the gate pulse, can then be detected as a function of the latter, which is delayed in time by a suitable delay stage. Hence, the gated fluorescence light is detected time-resolved. A sketch of the general gating procedure is given in Fig. 2.1.

2.2.1 Femtosecond UV Fluorescence Up-Conversion Technique

The optical gating medium in the fluorescence up-conversion technique is a nonlinear crystal. Due to its high nonlinear second-order susceptibility and the high intensity of the gate pulse, frequency conversion via the nonlinear process of SFG opens the gating device in a $\chi^{(2)}$ process: The gate pulse (ω_{gate}) up-converts (gates) the fluorescence photons (ω_{fl}) under conservation of energy and momentum, into photons of the sum frequency (ω_{SFG}), which can only occur if both, fluorescence light pulse and gate pulse are temporarily and spatially overlapped in the crystal:

$$\omega_{SFG} = \omega_{fl} + \omega_{gate}. \quad (2.17)$$

Fig. 2.2 gives a sketch of the resulting scanning sequence of the gate in the up-conversion experiment. As the gate pulse is delayed in time, the respective time-dependent overlap integral of fluorescence light and gate pulse determines the SFG intensity, which is directly correlated to the molecular fluorescence intensity.

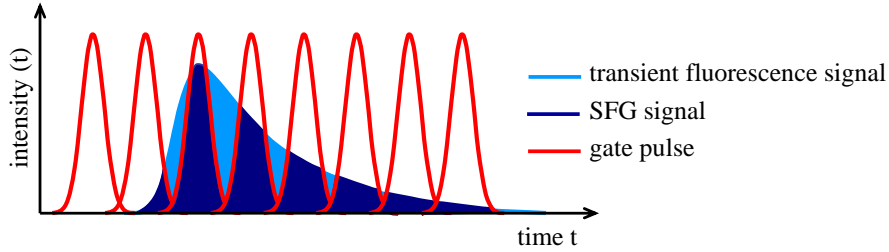


Figure 2.2: Gating process in fluorescence up-conversion spectroscopy: The fluorescence light pulse (ω_{fl}) is transmitted for the duration of the gate pulse (ω_{gate}), which up-converts the fluorescence light pulse into the sum frequency (ω_{SFG}). The gate opens the gating device for its respective pulse duration. Thus, the SFG intensity is correlated to the gate and fluorescence light pulse intensity. As the latter is a transient decreasing signal, the evolution of the SFG signal monitors directly the changes of the molecular fluorescence.

As the SFG process requires phase matching conditions, only a limited part of the spectral range can be up-converted simultaneously. The spectral bandwidth of the up-converted light as well as conversion efficiency of the process is mostly dependent on the mismatch of the involved \mathbf{k} vectors of the light pulses:

$$\Delta\mathbf{k} = \mathbf{k}_{SFG}(\omega_{SFG}) - \mathbf{k}_{fl}(\omega_{fl}) - \mathbf{k}_{gate}(\omega_{gate}) \quad (2.18)$$

The quantum efficiency of the SFG process is given by [3]:

$$\frac{W_{SFG}}{W_{fl}} = \text{const.} \cdot \frac{L^2 \cdot d_{eff}^2 \cdot W_{gate} \cdot \omega_{SFG} \cdot \omega_{fl}}{A \cdot \lambda_{SFG}^2 \cdot n_{SFG} \cdot n_{fl} \cdot n_{gate}} \left(\frac{\sin \Delta k L / 2}{\Delta k L / 2} \right)^2. \quad (2.19)$$

Here W denotes the respective power per area of the involved light pulses, L is the optical pathlength of the crystal and d_{eff} is its frequency and angle dependent anisotropy coefficient. The interaction length of the light pulses within the crystal is described by A . Because of the \mathbf{k} -dependent GVD of the incident waves in the SFG crystal and a strong walk-off effect, enforced by too harsh focusing conditions, the phase matching condition $\Delta \mathbf{k} = 0$ can only be approximated. Recently, it has been shown that the use of very thin crystals and NIR gate pulses in a non-collinear SFG geometry with an additional pulse front tilting of the gate pulse gives up-converted fluorescence spectra over a wide frequency range with 80 fs time resolution [3, 5].

In non-collinear geometry, the up-converted light can be obtained relative to the incident gate or fluorescence light pulse under the relative internal angle β or γ . Both can be calculated from a suitable reference scheme. This is given in Fig. 2.3. Here, the main reference axes are the optical axis z of the crystal and the surface normal N . They enclose the angle Θ_N . The relative angles of up-converted, fluorescence and gate pulse with z are Θ_{SFG} , Θ_{fl} and Θ_{gate} . The angle α determines the relative, internal angle of incident for the fluorescence and gate light pulse. It determines the center frequency of the up-converted spectral region and thus a tilting of the crystal allows for the selection of a desired spectral range. A numeric calculation of the parameters can be carried out, if $n(\omega)$, λ_{fl} , λ_{gate} and α are known:

$$\mathbf{k}_{SFG}^2 = \mathbf{k}_{gate}^2 + \mathbf{k}_{fl}^2 - 2\mathbf{k}_{gate}\mathbf{k}_{fl} \cos(180^\circ - \alpha) \quad (2.20)$$

$$= \mathbf{k}_{fl}^2 + \mathbf{k}_{gate}^2 + 2\mathbf{k}_{gate}\mathbf{k}_{fl} \cos \alpha \quad (2.21)$$

$$\mathbf{k}_{fl}^2 = \mathbf{k}_{gate}^2 + \mathbf{k}_{SFG}^2 - 2\mathbf{k}_{gate}\mathbf{k}_{SFG} \cos \beta. \quad (2.22)$$

External angles can be derived by Snell's law.

However, the application of the femtosecond fluorescence up-conversion method is limited. As described above, the up-converted frequency region is restricted by the fulfillment of the phase matching condition. Moreover, the up-conversion efficiency is wavelength-dependent and the tilting of the SFG crystal entails a wavelength-dependent mismatch of the time origin and thus a suitable time-correction is needed [3, 5, 6]. Nevertheless, the femtosecond fluorescence up-conversion experiment has been established as a powerful, highly sensitive tool for the detection of extremely low-intensity fluorescence signals in a single photon counting mode.

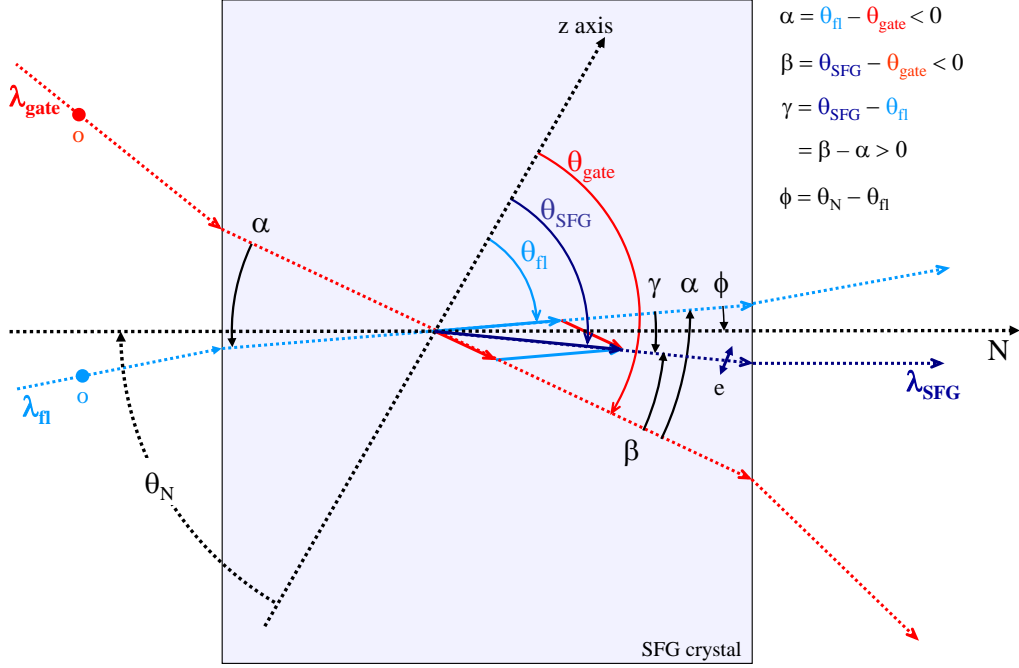


Figure 2.3: Non-collinear beam geometry in fluorescence up-conversion spectroscopy.

2.2.2 Setup of the UV Fluorescence Up-Conversion Experiment

The following description of the experimental setup can be followed with the help of Fig. 2.4. One half ($\approx 450\mu\text{J}$) of the output intensity of a regeneratively amplified Ti:Sa femtosecond laser (Clark-MXR, CPA 2001) with a pulse duration of ≈ 150 fs (Gaussian FWHM), a repetition rate of 1 kHz and an output wavelength of $\lambda = 775$ nm was used to run the experiment. The laser pulse was split approximately equally into the pump ($\approx 230 \mu\text{J}$) and gate ($\approx 220 \mu\text{J}$) pulses.

2.2.2.1 Generation of UV Pump Pulses for Excitation

All time-resolved fluorescence measurements were carried out with UV excitation pulses and thus, the laser fundamental had to be converted to the UV. The pump pulse wavelength was needed to be tunable between $258 \text{ nm} \leq \lambda_{pump} \leq 325 \text{ nm}$, as specific excitation schemes were realized for the different experiments performed within this *Thesis*. Thus, the pump pulses were generated from a home-built frequency-doubled tunable non-collinear optical parametric amplifier (NOPA).

As the NOPA was pumped with the second harmonic of the laser fundamental, the bulk of the $230 \mu\text{J}$ Ti:Sa split-off beam was used for the SHG process. The incoming pulse passed a quartz glass wedge (30° , $d = 25$ mm, $l = 3$ mm, Laseroptik), which was used to separate $\approx 1 \mu\text{J}$ for the seed pulse generation (see below). After traversing through a manually controlled delay stage, a 2 : 1 telescope system ($f = 200$ mm and $f = -100$ mm) was used to reduce the spot size. It was then guided onto a BBO crystal to obtain SHG ($\Theta = 29.8^\circ$,

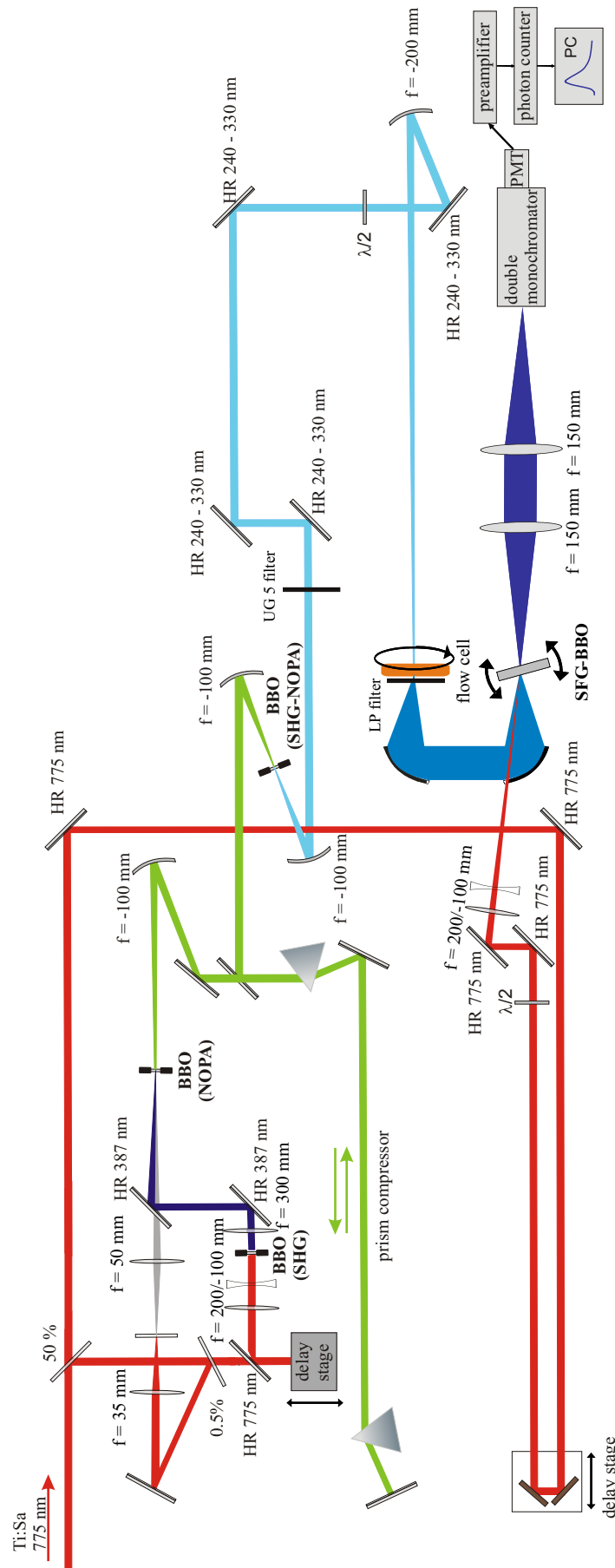


Figure 2.4: Experimental setup of the UV fluorescence up-conversion experiment.

$\varphi = 90^\circ$, type I, $7 \times 7 \times 0.5 \text{ mm}^3$, TOPAG). Residual light of the fundamental was cut off by two dielectric mirrors (HR 387 nm/HT 775 nm, Laseroptik). A $f = 300 \text{ mm}$ lens was afterwards used to focus the second harmonic into a BBO crystal ($\Theta = 32^\circ$, $\varphi = 90^\circ$, type II, $6 \times 6 \times 2 \text{ mm}^3$, TOPAG) for the amplification process.

Here, it was spatially and temporarily overlapped with the seed pulse. The seed was generated from the front surface reflection of the quartz glass wedge ($\approx 1 \mu\text{J}$). After passing suitable gradient neutral density (NG) filters ($l = 1 \text{ mm}$, Edmund Optics), it was focused with a $f = 35 \text{ mm}$ lens onto a sapphire plate ($l = 2.3 \text{ mm}$, Newport) for supercontinuum generation. In this process, the laser fundamental was spectrally and temporarily broadened. It finally covered the spectral range between $\approx 450 \text{ nm}$ and the NIR, and exhibited a pulse duration $> 1 \text{ ps}$. A second lens with $f = 50 \text{ mm}$ focused the seed pulse into the BBO crystal for amplification. The desired NOPA output wavelength within the white light supercontinuum pulse was then chosen by varying the delay time between pump and seed through a manually controlled delay stage.

A $f = 100 \text{ mm}$ lens (or likewise a $f = -100 \text{ mm}$ spherical mirror ($d = 25.4 \text{ mm}$, Laser Components)) was used to collimate the NOPA output. The pulse duration of the NOPA output was reduced by a prism compression stage. It was made up by two 60° FS prisms with side lengths of 2.5 cm . Aside from the folding mirror (prot. Al for VIS/IR, Laser2000) behind the second prism, an additional folding mirror was used to reduce the space on the optical table required for the compression stage. The distance between the two prisms was set to fit the respective amplified NOPA output wavelength and ranged between ≈ 89 and 120 cm . Prism compression provided pulses of $< 50 \text{ fs}$ (typically $\approx 35 \text{ fs}$) duration (Gaussian FWHM).

The compressed NOPA output was coupled out and focused (lens with $f = 100 \text{ mm}$ or spherical mirror with $f = -100 \text{ mm}$, respectively) into a suitable BBO crystal for collinear SHG. Different BBOs (TOPAG) with different phase matching parameters were used to cover certain spectral regions of the NOPA output. For the generation of UV pump pulses around $\lambda_{pump} = 260 \text{ nm}$, a crystal with $\Theta = 49.3^\circ$, $\varphi = 90^\circ$, type I, $5 \times 5 \times 0.2 \text{ mm}^3$ was used. Around $\lambda_{pump} = 280 \text{ nm}$, the parameters were $\Theta = 44.3^\circ$, $\varphi = 90^\circ$, type I, $5 \times 5 \times 0.2 \text{ mm}^3$. A crystal with $\Theta = 41.4^\circ$, $\varphi = 90^\circ$, type I, $5 \times 5 \times 0.2 \text{ mm}^3$ was taken for $\lambda_{pump} \approx 295 \text{ nm}$, while $\Theta = 38.9^\circ$, $\varphi = 90^\circ$, type I, $5 \times 5 \times 0.2 \text{ mm}^3$ was suited for $\lambda_{pump} \approx 310 \text{ nm}$. The spectral bandwidth was between $\Delta\lambda \approx 3 - 5 \text{ nm}$ (FWHM) in all cases. A second, identical lens/spherical mirror was used to collimate the frequency-doubled output. Due to the collinear arrangement of the SHG process, the remaining NOPA fundamental was separated from the UV pulses (collimated beam diameter $\approx 4 \text{ mm}$) by three or four dielectric mirrors. Different sets with adequate coatings for the respective spectral region were used (HR 245 – 330/HT 490 – 660, Laseroptik). If necessary, a UG 5 filter ($l = 1 \text{ mm}$, Schott LOT) was placed in the beam path.

2.2.2.2 Sample Excitation and Fluorescence Picking

The generated UV excitation pulses were focused either with a lens of $f = 300$ mm or a spherical mirror of $f = -200$ mm into the sample cell. The polarization of the fluorescence light was rotated to the magic angle in order to avoid fluorescence depolarization effects ($d = 25.4$ mm, zero-order wave plate $\lambda/2$, Newport). The sample cell was a flow cell with a pathlength of $l = 1$ mm and quartz glass windows with a diameter of $d = 15$ mm and a thickness of $l = 0.2$ mm (Korth Kristalle). The spot size of the pump light in the flow cell was ≈ 400 μm . A peristaltic pump (Ismatec, MS-CA2/860; 6.8 mL/min flow rate; 3-stop tubing (inner diameter $d = 1.42$ mm): Fluran HCA F-5500-A or PharMed Ismaprene) was used to continuously pump the sample solutions through the flow cell to avoid the accumulation of photoproducts. The integrity of the sensitive and easy to damage biological sample material was ensured by two closely linked requirements. First of all, the maximum excitation pulse energy never exceeded $E_{(pump)} \approx 0.18$ μJ . The highest intensities were only used for the most stable sample material, e.g., for the adenine (A) derivative dimethyladenine (DMA) (*Chapters 3 and 4*). Indeed, extraordinary high care was taken to rule out photodamage especially of guanine (G) containing samples. For measurements on the hydrogen-bonded base pairs (*Chapters 5, 6, 8 and 9*) as well as the short DNA single and double strands (*Chapters 10 and 11*) the pump pulse energy was not more than $E_{pump} \approx 0.03 - 0.1$ μJ . Additionally, the sample volume, allocated in the sample tank, and the sample concentrations were chosen to vastly exceed the number of UV pump photons arriving at the sample cell.

A detailed description of the sample preparation and handling is given in Section 2.4. Typically, measurements were repeated up to four times with the same sample volume and again with different sample batches to check the reproducibilities of the measurements. Additionally, measurements on the neat solvent or buffer were done on each measuring day to cross-check, whether unwanted background signals occurred. All time-resolved fluorescence measurements were carried out at room temperature.

The fluorescence generated by the pump pulse was collected and collimated by a 90° off-axis parabolic mirror ($f = 119$ mm, aperture = 63.5 mm, Melles-Griot). Residual pump light was caught by a beam stop and, if necessary, scattered pump light was blocked via a white glass filter ($l = 1$ mm, HQ340LP, Schott LOT). A second, identical parabolic mirror was used to refocus the fluorescence light into the BBO crystal ($\Theta = 54.4^\circ$, $\varphi = 0^\circ$, type I, $5 \times 5 \times 0.1$ mm³, GWU) for the SFG process. This crystal was used for the measurements on the DNA samples. It has to be replaced, if measurements in a different spectral region are performed, i.e., if other up-converted fluorescence wavelengths are of interest.

2.2.2.3 Gate Pulse Coupling and SFG Process

The Ti:Sa laser fundamental was used as the gate pulse. It traversed a similar optical path length as the pump/fluorescence light and was focused into the SFG crystal by either a

2 : 1 telescope system ($f = 200$ mm and $f = -100$ mm) or a spherical mirror ($f = -100$ or -200 mm). The focal plane was set ≈ 5 cm before or after the SFG crystal, as the crystal would have been destroyed otherwise. Temporal fluorescence profiles were recorded by stepping the time delay of the gate pulses using a computer-controlled 150 mm linear translation stage (M-415CG, Physik Instrumente). The polarization of the gate beam was rotated ($d = 25.4$ mm, zero-order wave plate $\lambda/2$, Newport) from horizontal to vertical in order to obtain type I non-collinear SFG, which is required for the up-conversion process in the UV. The relative angle between the incident fluorescence light and gate beam was $\approx 14^\circ$. Typically, the gate pulse energy was $\approx 90 \mu\text{J}$.

Fluorescence signals were recorded between $290 \text{ nm} \leq \lambda_{fl} \leq 650 \text{ nm}$ (up-converted wavelengths between $211 \text{ nm} \leq \lambda_{SFG} \leq 354 \text{ nm}$) in a set of different pump-gate scans. Each required an appropriate setting of the monochromator wavelength and a specific tilting of the SFG crystal by a few degrees. Unfortunately, the gate pulse easily generated its second and third harmonic in the type I SFG crystal. The spectral region between $369 \text{ nm} \lesssim \lambda_{fl} \lesssim 405 \text{ nm}$ ($250 \text{ nm} \lesssim \lambda_{SFG} \lesssim 266 \text{ nm}$) was spectroscopically dark due to interfering third harmonic signals (THG). The THG signal ($\lambda_{THG} = 258 \text{ nm}$) is overwhelming and easily saturates (i.e., damages) the PMT detection unit (see Section 2.2.2). Nevertheless, it was in majority efficiently blocked by the 3-slit double monochromator assembly. However, at the edges of the spectroscopically dark window, a background drift due to the competing processes of THG vs. SFG occurred, which could affect the measured fluorescence decay profiles and thus needed to be eliminated by a proper alignment of the setup. Moreover, at red fluorescence wavelengths, i.e., $\lambda_{fl} > 550 \text{ nm}$ ($\lambda_{SFG} > 320 \text{ nm}$), interfering SHG signals caused an enhanced background noise. However, if the fluorescence was monitored for a set of fluorescence wavelength extending into the visible, the type I arrangement was maintained, although type II SFG would give a better S/N ratio here. This avoided the exchange of the up-conversion crystal during the experiments and the realignment of the optical setup between scans for different λ_{fl} .

In order to keep the signals of the harmonics as low as possible, it was proceeded as follows:

(i) The higher the tilt angle of the crystal (it has to be tilted by $\Phi \geq 20^\circ$ for $\lambda_{fl} \geq 500$ nm) the more efficient were the processes of SHG and THG. But, as the acceptance angle for SFG has some variance of $\Delta\Phi \approx 3 - 5^\circ$, Φ was set to the lowest possible tilt angle at an arguable cost of the photon count rate. Unfortunately, SFG crystals, where the cut angle matches for the up-conversion of red fluorescence wavelengths without tilting (e.g., $\Theta = 43.3^\circ$ or $\Theta = 46.3^\circ$), did produce THG and SHG signals, which overruled any other nonlinear signals generated through excitation with low-power (E_{pump}) UV pump light.

(ii) Both, the SFG and the THG/SHG signal efficiencies directly depend on the intensity of the gate pulse. Thus, it can be expected that a reduction of the gate pulse energy (E_{gate}) reduces the background noise, especially caused by THG in a $\chi^{(3)}$ process. A successive reduction of E_{gate} from ≈ 80 to $30 \mu\text{J}$ showed a linear decrease of the SFG count rate, but as the THG signal was higher than the saturation limit of the PMT, it

was not affected significantly. However, best results with sufficient background suppression were observed, when the spot size of the gate pulse in the SFG crystal was expanded by the telescope system. Although the focus of the fluorescence spot in the SFG crystal was around $\approx 400\mu\text{m}$, the gate pulse diameter was set to the dimension of the crystal aperture ($2.5 \times 2.5\text{mm}$). This gave satisfying SFG count rates at all gated fluorescence wavelengths and the interference of THG and SHG was under control.

2.2.2.3.1 Time Resolution and Time Zero

The instrument response function (IRF) was determined by cross-correlation of scattered pump light with the gate pulses. The width of the IRF on average corresponded to a standard deviation of a Gaussian of $\tau_{IRF} = 0.2 \pm 0.04$ ps, which was the approximate time resolution of the experiments. This limit was set through the use of the laser fundamental for gating. Its auto-correlation width measured shortly before its injection into the SFG crystal was ≈ 163 fs (Gaussian FWHM).

Time zero values (t_0), especially for rise time measurements at the red fluorescence wavelengths of DMA (see *Chapters 3* and *4*), were determined by reference to the emission of selected laser dyes (rhodamine 6G, coumarin, fluorescein 27, stilbene 3 and DMQ) with fast fluorescence rise times.

2.2.2.4 Photon Counting Detection Unit

The up-converted light was collimated and focused (SQ, $f = 150$ mm, 2") onto the entrance slit of an $f = 0.1$ m double monochromator (1 mm slit width; 5 nm spectral resolution; 1200G/mm gratings, blaze wavelength = 250 nm; Jobin-Yvon HR 10) and detected with a photomultiplier (Hamamatsu R1527P) connected to a preamplifier (Stanford Research SR 445) and gated photon counter (Stanford Research SR 400). Due to the required time budget, the gate delay of the photon counter was set to 178 ns and the gate width was best at 65 ns. On average 15.000 laser shots were accumulated per delay step. A minimum of 5000 shots as well as a maximum of 30.000 shots were exceeded. Thus, at 1 kHz repetition rate, the photon count rates never overran 200 photons/s to avoid two-photon coincidences. Typically, 20 – 50 photons/s were detected.

The fluorescence decay profiles were monitored in steps of $\Delta t \approx 50 - 500$ fs in the region of the rise and initial decay of the fluorescence decay curves. Otherwise, step sizes of 1 – 25 ps were used. The entire data collection, including the delay stage, was controlled by a program written in LabView software (see *Appendix*) [7].

2.2.3 Broadband Detection Techniques

2.2.3.1 Broadband Up-Conversion Experiment

First steps have been made to monitor the gated SFG bandwidth of the up-conversion setup. Towards these ends, the gated spectral bandwidth of an aqueous solution of stilbene 3 was estimated with the ‘standard’ PMT detection unit first. At a tilt angle of $\approx 5^\circ$, fluorescence light could be monitored between $430 \text{ nm} \leq \lambda_{fl} \leq 510 \text{ nm}$ with sufficient background suppression (ratio between fluorescence decay curve maximum and background was 80 at the maximum and 2 at the minimum).

In order to measure the full up-converted spectral band simultaneously, a broadband detection unit with a spectrograph (Acton ARC SP-2156, 150G/mm grating, blaze wavelength = 300 nm) and a ICCD camera (PI-MAX 1024RB-25FG-43) was used. A bandpass filter (Semrock FF01-280/20) was used for background suppression. The obtained signal was rather weak, although 40.000 – 1.500.000 laser shots were accumulated with full MCP gain. The data collecting procedure, including the delay stage was under LabView control [8]. Fig. 2.5 gives the measured up-converted spectral bandwidth of stilbene 3 in water after excitation with $\lambda_{pump} = 260 \text{ nm}$. The excitation energy was $\approx 0.05 \mu\text{J}$ and the entrance slit width was 0.75 mm. The center wavelength of the spectrograph was set to $\lambda_{SFG} = 280 \text{ nm}$. The ICCD was run in shutter mode, i.e., it was triggered by the Ti:Sa laser and opened for the preset exposure time. The upper panel shows the raw data, while the lower shows the spectrum after background subtraction in comparison to the static fluorescence spectrum of stilbene 3.

Clearly, the combination of the single slit spectrometer with a grating of 150 G/mm, which monitors a spectral bandwidth of $\approx 720 \text{ nm}$ on the CCD chip, is insufficient to resolve the SFG signal from the large THG and SHG background noise. However, no other grating was available in our laboratory at the time of these experiments. The THG and SHG backgrounds appear on the same fs timescale and cannot be cut off by the shutter (or gate mode) operation of the ICCD camera. An aperture was placed between the spectrograph and the ICCD camera to avoid a damage of the CCD chip by the zero- or higher-order diffractions. Because of the low spectral resolution, a filtering of the up-converted signal from the background in accordance to Cannizzo *et al.* [9], who carried out a spatial selection after the SFG crystal, was not helpful. Other gratings (600 and 1200 G/mm) with higher diffraction might help to improve the setup, but these will strongly disperse the SFG signal over the CCD chip. In consequence, this will give a low electron/pixel ratio, which might increase the accumulation time for the SFG spectrum. Alternatively, a prism spectrometer might be helpful, because of its much higher light power.

A second important fact to mention is the difference in the amplification factors of the ICCD and the preamplifier/PMT setups. The intensifier of the ICCD consists of a UV-sensitive photocathode, a single MCP and P43 phosphor screen. MCP and phosphor screen give an amplification factor of ≈ 80.000 (but this is altered by the quantum efficiency of

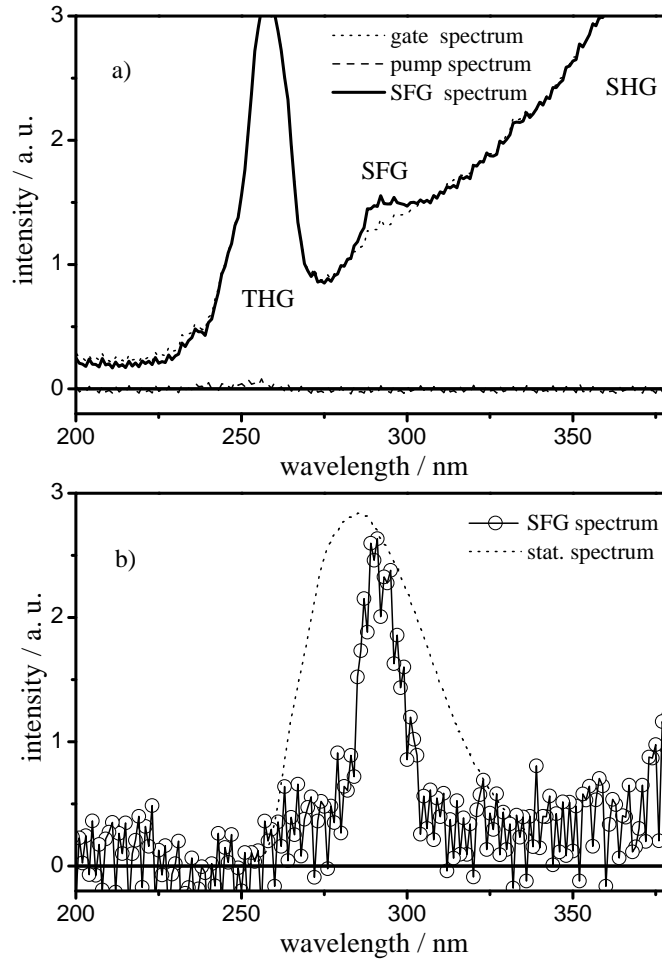


Figure 2.5: SFG spectrum of stilbene 3: a) Raw data; b) Data after background subtraction.

the photocathode). In contrast, the gain factor of the preamplifier and PMT is $\approx 3 \cdot 10^7$. Of course, both setups depend on the UV efficiencies of the gratings.

2.2.3.2 Kerr Gate Experiment

In the optical Kerr gating experiment, the nonlinear BBO crystal is replaced by a Kerr medium as the gating device. The Kerr medium is isotropic and can be a gas, a liquid or a solid. It is placed between two crossed polarizers. The incident fluorescence light passes the first polarizer, propagates through the Kerr medium and is not permitted by the second, crossed polarizer as long as the gate pulse is absent. When the gate beam is focused onto the Kerr medium (without passing the first polarizer), its high intensity induces a strong anisotropy in the medium. Due to the OKE $\chi^{(3)}$ process, the Kerr medium becomes birefringent. The passing linearly polarized fluorescence light changes to an elliptical polarization because of the modulation the refractive index. Best gating efficiencies are obtained, when the relative polarization angle between gate and fluorescence light is 45° . A part of the elliptically polarized fluorescence light can then pass the second polarizer and is detected.

The spectral bandwidth of the Kerr gated light is not restricted by any phase matching conditions as in the up-conversion experiment. It is only determined by the transmittive properties of the Kerr medium. But, as in the fluorescence up-conversion experiment, the gating efficiency and time resolution depends on the time duration of pump and gate pulses, their relative angle of incidence on the Kerr medium and the GVD of the setup and inside the Kerr medium. A proper choice of the Kerr material is highly critical for the performance of the Kerr gate setup, especially with regard to the S/N ratio and the temporal resolution. The induced anisotropy in a solid is only dependent on the displacement of the electrons, which can follow the electric field practically instantaneously. In gases or liquids, the relaxation appears on a picosecond timescale, which excludes those materials for experiments in which a subpicosecond time resolution is required. Moreover, the gate pulse is scattered on the Kerr medium and might induce a high background noise (e.g., supercontinuum light), which can exceed the gated fluorescence signal at the detector by orders of magnitude. Finally, the extinction ratio of the crossed polarizers is essential for a sufficient S/N ratio, as the gated fluorescence light is rotated only by a few degrees [10, 11]. In the present *Thesis*, first steps have been done to realize a Kerr gate scheme. A sketch of the setup is given in Fig. 2.6. The SFG crystal of the described fluorescence up-

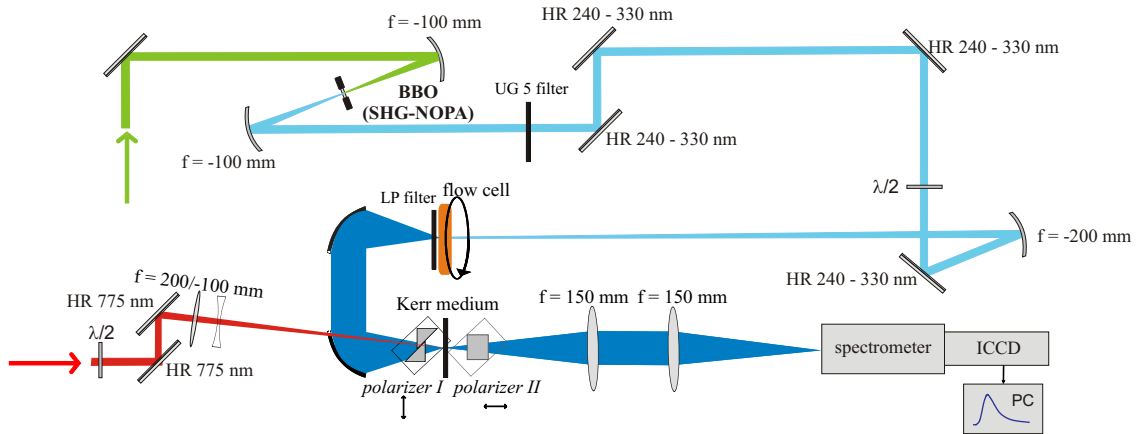


Figure 2.6: Experimental setup of the Kerr gate experiment. Note that the gate pulse does not pass polarizer I. Instead it was coupled into the Kerr medium from above under an angle of $\approx 20^\circ$.

conversion setup and the photon counting detection unit were replaced by the Kerr gate and by the spectrograph/ICCD camera already described above. The wavelength- and time-resolved data collection procedure, including the delay stage, was under LabView control (see *Appendix*) [8]. A $l = 0.2$ mm thick quartz window (Korth Kristalle) as well as a cuvette (special order, $l = 1$ mm, Hellma GmbH) with Uvasol benzene were tested as Kerr media. The respective Kerr medium was placed between two Glan prisms (calcite, edge length = 10 mm; variable aperture of 1–5 mm; extinction ratio 10^{-6} , B. Halle), which were placed on rotary mounts (Newport). A 700 nm cut-off filter ($l = 1$ mm, Edmund Optics) was used for background suppression.

The setup mostly suffered from a too low filtering of the polarization of the fluorescence light. This was mainly due to the focal length of the off-axis parabolic mirrors. The effective length, on which the fluorescence light has a small spot size, was not more than ≈ 1.5 cm. Thus, both polarizers and the Kerr medium have to be placed in short succession behind each other, which made it difficult to illuminate the prisms accurately, although apertures were used to minimize the amount of unwanted scattered and diffusely polarized light. Due to the reduced space, the gate pulse was coupled into the Kerr medium from above under a angle of $\approx 20^\circ$. A replacement of the paraboloidal mirrors, e.g., by concave mirrors with high focal length according to Arzhantsev *et al.* [11], will improve the setup.

Nevertheless, measurements with benzene as the Kerr medium gave first signals. Fig. 2.7 gives the gated spectrum of rhodamine 6G in water after excitation with $\lambda_{pump} = 260$ nm. The excitation energy was $\approx 0.05 \mu\text{J}$ and the entrance slit width was 1.3 mm. The center wavelength of the spectrograph was set to $\lambda = 800$ nm, which avoided the detection of zero- or higher-order diffraction. The ICCD was run in shutter mode and 8000 images were accumulated at each delay step ($\Delta t = 0.35$ ps) with full gain of the ICCD. The upper panel shows the raw data of signal (red) and background (black) at $\lambda_{fl} = 550$ nm. The middle panel shows the spectrum after background subtraction in comparison to the static fluorescence spectrum of rhodamine 6G and the lower gives the fluorescence decay profile at $\lambda_{fl} = 550$ nm. The discrepancy between

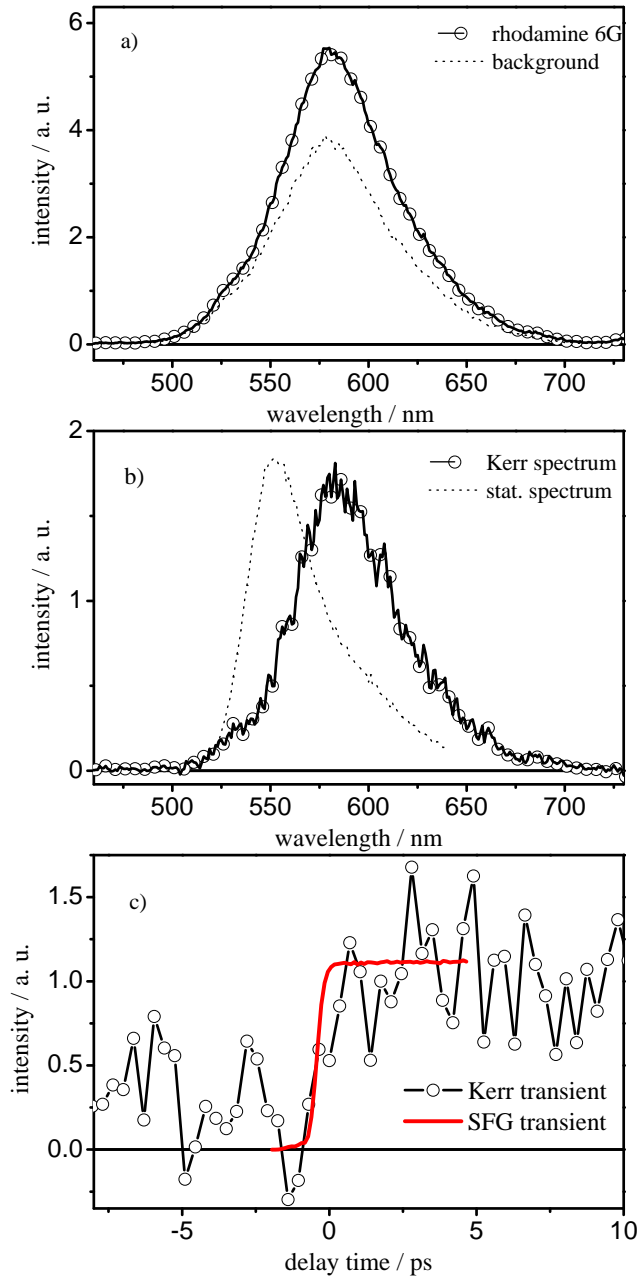


Figure 2.7: Kerr-gated spectrum of rhodamine 6G: a) Raw data; b) data after background subtraction in comparison to the static fluorescence spectrum; c) fluorescence time profile at $\lambda_{fl} = 650\text{nm}$ in comparison to the profile measured with the up-conversion setup under the same conditions. The noise arises from the high background.

the stationary and Kerr-gated fluorescence spectra might be due to an insufficient calibration of the spectrometer (carried out with photodiodes of different wavelengths) as it was far from the blaze wavelength of the grating.

2.3 Data Analysis

All fitting routines used for the data analysis of the measured transient decay curves (see 2.3 and 2.3) and static spectra (see 2.5) were programmed with the MATHEMATICA software [12]. Because of their size, the respective source codes are not listed in this *Thesis*. However, the basic fit functions are described in the following.

2.3.1 Fluorescence Decay Profiles

The measured fluorescence decay profiles were analyzed using a nonlinear least-squares fitting routine based on the Levenberg-Marquardt algorithm implemented in the MATHEMATICA software [12]. The time profiles $f(\lambda, t)$ at the fluorescence wavelength λ of the molecules studied can each be represented by using sums of exponentials with time constants τ_i and amplitudes A_i

$$f(\lambda, t) = \sum A_i \cdot \exp\left(\frac{-t}{\tau_i}\right) \quad (2.23)$$

for $t \geq 0$ ($f(\lambda, t) = 0$ for $t < 0$). However, the final experimental time resolution owing to the finite duration of the pump and gate pulses and owing to the GVD and other experimental effects has to be taken into account. These contributions are described by the instrumental response function (IRF). It is customary to approximate the IRF by a Gaussian

$$g(t) = \frac{1}{\sigma\sqrt{2\pi}} \cdot \exp\left[-\frac{t^2}{2\sigma^2}\right] \quad (2.24)$$

with unit area, width parameter σ (\equiv standard deviation of the Gaussian) and peak at $t = 0$. The width σ is related to the full width at half maximum (FWHM) by

$$FWHM = \sqrt{8 \cdot \ln 2} \approx 2.355 \cdot \sigma. \quad (2.25)$$

The experimentally observed fluorescence decay profile $I(\lambda, t)$ is thus described by the convolution of $f(\lambda, t)$ with $g(t)$, which is usually abbreviated by

$$I(\lambda, t) = [f(\lambda) * g](t), \quad (2.26)$$

where $*$ marks the convolution integral. $[f(\lambda) * g](t)$ is defined as

$$[f(\lambda) * g](t) \equiv \int_{-\infty}^{+\infty} f(t')g(t-t')dt' = \int_{-\infty}^{+\infty} f(t-t')g(t')dt', \quad (2.27)$$

where t' is the integration variable. Substituting for $f(\lambda)$ and g using Eqs. 2.23 and 2.24, the convolution integral can be evaluated analytically [12] to yield the observable

fluorescence decay profile

$$I(\lambda, t) = b + \frac{1}{2} \sum A_i \cdot \exp \left[\frac{\sigma^2}{2\tau_i^2} - \frac{(t - t_0)}{\tau_i} \right] \cdot \left[1 + \operatorname{erf} \left(\frac{(t - t_0)\tau_i - \sigma^2}{\sqrt{2} \cdot \sigma \cdot \tau_i} \right) \right] \quad (2.28)$$

Here, in addition to the convolution, the shift of the experimental time scale to t_0 (\equiv time of pump laser pulse) has been taken into account. An additional constant background term b has been added to account for scattered light, etc. (if necessary, a further linear drift term $c \cdot t$ could be added as well).

In the data analysis carried out in this work, a model function of the type $I(\lambda, t)$ (Eq. 2.28) was first fitted to each measured fluorescence time profile individually to determine the time zero t_0 , IRF parameter σ and the set of time constants τ_i with fractional amplitudes A_i . All parameters were allowed to float freely. The IRF widths determined by these fits agreed with the pump-gate cross-correlation values given above. The parameters b and t_0 were subsequently subtracted from the displayed transient data sets in all figures in this *Thesis* and the included publications, as they are merely experimental parameters. The fitted parameters τ_i and A_i are given as results with 2σ standard deviation (95% confidence interval). The sums of the respective fractional A_i s were normalized (i.e., $\sum A_i = 1$).

A global fitting procedure was applied, when it turned out that the individual fits results of specific fluorescence decay curves showed virtually identical decay constants within the standard deviation. All global parameters were free-floating, but, if necessary, t_0 values were kept fixed at the result from the individual fits to avoid memory overflow.

A special variation of the described data analysis was needed to dissect the measured fluorescence decay profiles into contributions of nucleobase monomer (M) and homo- or heterodimer (D) (*Chapters 5 and 6*). Both constitute the experimentally observed profiles via

$$F(t, c_0) = n_{abs}(c_0) \cdot [(1 - \beta_i(c_0)) Y_M(t) + \beta_i(c_0) Y_D(t)] \quad (2.29)$$

with $n_{abs}(c_0)$ being the effective number of photo-excited molecules, β_i the respective degree of association and $Y_{M,D}(t)$ given through 2.28. Thus, data separation was required to determine their fractional fluorescence decay curves and individual decay time constants.

At time $t = 0$ after the pump pulse the initial fluorescence signals should correspond to the number of photo-excited monomer and dimer molecules $n_{abs}(c_0)$ at the respective initial concentration c_0 , if the electronic properties of the molecules (i.e., fluorescence transition properties) are not significantly altered on complexation. Moreover, the relationship $\epsilon_D = 2\epsilon_M$ has to be fulfilled, which fully holds true for the investigated hydrogen-bonded G and C containing base pairs (*Chapters 5 and 6*). Due to Lambert-Beer's law, $n_{abs}(c_0)$ is given by

$$n_{abs}(c_0) = 1 - 10^{\epsilon_i \cdot c \cdot l}, \quad (2.30)$$

where l is the optical pathlength and ϵ_i is the effective absorption coefficient with respect to c_0 .

The respective amount of monomer and homo- or heterodimer in solution depend on the association equilibria given by β_i and the association constants K_i , respectively (see 2.5).

The fluorescence decay profiles of the respective pure monomers ($i = M$) from a homonucleoside ($i = MM$) solution can be derived via

$$\begin{aligned} I_M^{corr}(\lambda, t) &= n_{abs}(c_{01}) \cdot I^{norm}(\lambda, t, c_{01}) \\ &- \frac{n_{abs}(c_{01}) \cdot \beta_{MM}(c_{01})}{n_{abs}(c_1) \cdot \beta_{MM}(c_1)} \cdot F(t, c_0 = c_1) \end{aligned} \quad (2.31)$$

at low-concentration measurements ($c_0 = c_{01} = 0.1$ mM). The pure homodimer profiles ($i = MM$) can be obtained from higher-concentration measurements ($c_0 = c_1 = 1.0$ mM) via

$$\begin{aligned} I_{MM}^{corr}(\lambda, t) &= n_{abs}(c_1) \cdot I^{norm}(\lambda, t, c_1) \\ &- \frac{n_{abs}(c_1) \cdot (1 - \beta_{MM}(c_1))}{n_{abs}(c_{01}) \cdot (1 - \beta_{MM}(c_{01}))} \cdot F(t, c_0 = c_{01}). \end{aligned}$$

Residual fractions of unpaired nucleosides needed to be subtracted from the measured fluorescence decay profiles of the 1:1 mixtures of the nucleobase $i = M$ with $i = N$ to observe the profiles of the ‘pure’ hetero-base pair ($i = MN$) at any concentration c_0 by

$$\begin{aligned} I_{MN}^{corr}(\lambda, t, c_0) &= I_{MN}^{norm}(\lambda, t, c_0) \\ &- \beta_{MN}(c_0) \cdot \left(\frac{\epsilon_M(c_0)}{\epsilon_{MN,eff}(c_0)} \cdot I_M^{norm}(\lambda, t, c_0) \right) \\ &- \beta_{MN}(c_0) \cdot \left(\frac{\epsilon_N(c_0)}{\epsilon_{MN,eff}(c_0)} \cdot I_N^{norm}(\lambda, t, c_0) \right), \end{aligned}$$

where $\epsilon_{MN,eff}$ is given by

$$\epsilon_{MN,eff} = \epsilon_{MN}(c_0) - \beta_{MN}(c_0) \cdot [(\epsilon_M(c_0) + \epsilon_N(c_0))].$$

2.3.2 Transient Fluorescence Spectra

Transient emission spectra $S_{fl}(\lambda, t)$ were reconstructed from the fluorescence decay profiles of DMA in water and in dioxane. Here, the normalized time-integrated intensities ($I_\infty(\lambda)$) were scaled by the intensities of the measured static fluorescence spectra ($I_{stat}(\lambda)$) using the approach introduced by Maroncelli and Fleming [13–15] as already described earlier [16, 17]:

$$I_\infty(\lambda) = \int_{t=0}^{\infty} I(\lambda, t) dt = \sum_i A_i \cdot \tau_i \quad (2.32)$$

and

$$S_{fl}(\lambda, t) = I_{stat}(\lambda) \cdot \frac{I(\lambda, t)}{I_{\infty}(\lambda)}. \quad (2.33)$$

A plot of $S_{fl}(\lambda, t)$ vs. λ_{fl} gives the temporal evolution of all λ_{fl} at the respective delay time t .

2.4 Sample Preparation and Handling

In the experiments, different DNA sample materials have been investigated. Each respective sample required a special treatment depending on whether a nucleobase monomer, nucleobase pairs or DNA single or double strands were studied. In the following, the sample handling for all three cases is listed.

2.4.1 Nucleobase Monomers

All nucleobase monomers were purchased from Sigma Aldrich. These, as well as the employed solvents, were used without further purification, if not stated otherwise.

N^6, N^6 -Dimethyladenine, DMA. Solutions of DMA (purity $\geq 98\%$) in water (bidest.) or in dry dioxane (Merck Uvasol, $\geq 99.9\%$) were prepared at a concentration of typically $c = 1$ mM. Test measurements were carried out at a ten times higher concentrations ($c = 10$ mM).

Guanosine, G. In order to estimate the effect of the TBDMS (*tert.*-butyldimethylsilyl) protecting group of G(TBDMS)₃ (preparation is given in the following) on the fluorescence decay in comparison to native G, solutions of both have been prepared in Uvasol ethanol (EtOH, Purity $\geq 99.9\%$) at a concentration of $c = 0.5$ mM.

Deoxyribose Monophosphates. For reference, all deoxyribose monophosphates (XMP) have been measured at $\lambda_{pump} = 260, 269$ and 284 nm (see *Appendix*). Therefore, solutions of $c = 0.1$ mM in water (bidest.) have been prepared of each XMP, which were purchased as deoxyribose monophosphate sodium salts.

2.4.2 Nucleobase Pairs

Specially protected (deoxy)ribose nucleosides X(TBDMS)_y (X = G, C, A, T, 2AP; y = 2,3) with sterically demanding unpolar *tert.*-butyldimethylsilyl (TBDMS) groups at the (deoxy)ribose units were synthesized. The modified nucleosides were highly soluble in aprotic solvents of low polarity like chloroform (CHCl₃), carbon tetrachloride (CCl₄) and *n*-hexane (C₆H₁₄). Thus, the solvent itself, as well as the (deoxy)ribose moieties, could not participate in hydrogen bonding. Moreover, in contrast to water, no base stacking occurred. Instead, the formation of well-defined hydrogen-bonded base pairs [18–22] was observable. The slightly polar or nonpolar environments induced by CHCl₃ ($\epsilon = 4.9$), CCl₄ ($\epsilon = 2.2$) and C₆H₁₄ ($\epsilon = 1.9$), respectively, perfectly well mimics the surrounding of

a nucleobase pair incorporated in a DNA double helix. Here, the dielectric constant was found to be of the order of $\epsilon = 3 - 5$ [23].

Different batches of protected nucleosides have been synthesized and characterized by NMR and FTIR spectroscopy. In the vast majority, transient experiments have been carried out on G and C containing base pairs. The protecting groups were found to have no impact on the fluorescence decay of the nucleosides (see *Chapters 6*). The synthesis protocol was as follows:

All starting material was commercially available from Sigma Aldrich, Merck, Ega-Chemie, Roth, Fluka or Acros. Solvents were distilled before use and, unless stated otherwise, chemicals were used without any further purification. G and C were purchased from Sigma-Aldrich. Synthesis was done under N₂ atmosphere. Thin-layer chromatography (TLC) was performed on Polygram SIL G/UV silica gel plates (Marcherey-Nagel), detected with UV-light (254 and 366nm). Flash column chromatography of the raw products was carried out with silica gel (particle size 0.06 mm–0.2 mm). NMR spectra were recorded on a Bruker DRX 500 instrument (300MHz for ¹H).

Synthesis of Protected Deoxycytidine dC(TBDMS)₂. 2.0 g (7.6 mmol) deoxycytidine was dissolved in 10 mL dimethyl formate (DMF) and stirred overnight with 5.05 g (33.5 mmol) TBDMSCl and 4.56 g (66.9 mmol) imidazole under N₂ atmosphere. Afterwards, the DMF was extracted with water (5 × 5 mL) and the organic phase was washed with ethyl acetate (5 × 5 mL). The combined organic phase was dried with sodium sulfate, subsequently filtered and most of the solvent was removed by evaporation. The obtained raw product was purified by flash column chromatography (ethyl acetate : THF, 7:3). The purified product was dried in vacuum for 8 days. 2.8 g (6.1 mmol) of a white powder was obtained (81%).

¹H-NMR (500 MHz, [D]CHCl₃, 298 K, TMS): $\delta = 8.01$ (d, 1H, C6-H), 6.25 (dd, 1H, C1'-H), 5.69 (d, 1H, C5-H), 4.37 (m, 1H, C3'-H), 3.91 (m, 2H, C4'-H, C5'-H), 3.76 (m, 1H, C5''-H), 2.42 (m, 1H, C2'-H), 2.08 (m, 1H, C2'-H), 1.1 (s, 18H, C(-CH₃)₃), 0.07 (m, 12H, Si-CH₃) ppm.

Synthesis of Protected Guanosine G(TBDMS)₃. 2 g (7.14 mmol) guanosine was dissolved in 18 mL DMF and stirred overnight with 5.4 g (36 mmol) TBDMSCl and 4.9 g (72 mmol) imidazole under N₂ atmosphere. The following work-up procedure was the same as for cytidine. The obtained raw product was recrystallized from ethanol and a white-yellowish solid was obtained. This was finally purified by flash column chromatography (chloroform : ethanol, 7:3). A white solid was obtained in a yield of 63% (2.8 g (4.5 mmol)).

¹H-NMR (500 MHz, [D]CHCl₃, 298 K, TMS): $\delta = 12.03$ (s, 1H, N1-H), 7.91 (s, 1H, C8-H), 6.24 (s, br, 2H, C2-NH₂), 5.82 (d, 1H, C1'-H), 4.44 (dd, 1H, C3'-H), 4.28 (dd, 1H, C2'-H), 4.10 (m, 1H, C4'-H), 3.99 (q, 1H, C5'-H), 3.77 (q, 1H, C5''-H), 0.96, 0.92, 0.87 (s, 27H, C(-CH₃)₃), 0.14, 0.09, 0.03 (m, m, s 9H, Si-CH₃) ppm.

Support in synthesis workload (especially for the ribose nucleosides and 2AP containing samples) was obtained from T. Michalak and J. Gripp (see *Appendix* and [20, 22, 24]).

Sample Handling in the fs Fluorescence Experiment. All UV fluorescence up-conversion experiments were performed with sample concentrations of 0.1 mM and 1.0 mM of G and C, respectively. Hence, parent solutions, each with a concentration of $c_0 = 2.0$ mM of G or C in CHCl_3 , were prepared. One half of each solution was subjected to a 1:1 mixture to obtain the $c_0 = 1.0$ mM concentrated solution of the hydrogen-bonded $\text{G}\cdots\text{C}$ Watson-Crick base pair. Each of the other half of the parent solutions were twofold diluted to obtain homonucleoside solutions with a concentration of $c_0 = 1.0$ mM. Part of each $c_0 = 1.0$ mM concentrated solution was then tenfold diluted to get the respective $c_0 = 0.1$ mM sample solutions. Amylene-stabilized chloroform was purchased from Sigma-Aldrich (> 99%ig, very high dry spectral grade). The sample volumes were between 150 – 250 mL. This ensured that approximately only 1% of the nucleobases were exposed to a UV pump photon during 6h of measurement.

If proceeded otherwise, i.e., using UV pump pulse powers $\gg 0.05 \mu\text{J}$ and low sample volumes ($\ll 100$ mL), G containing sample solutions became instable and showed drastically changing fluorescence decay profiles, which appeared as an increase of the relative count rates and a pronounced elongation of the fluorescence decay in dependence of the exposure time. This is exemplarily shown in Fig. 2.8. The observed dramatic changes in the transient profiles did not have an equivalent in the static UV absorption spectra. A change in the band shape of the static UV absorption spectrum of G was only observed under very harsh conditions, i.e., a few milliliters of allocated sample volume, reduced flow rate and > 6 h of irradiation. A comparison of the static UV absorption spectrum of a intact, purely G containing sample solution with its photo-burned counterpart is given in Fig. 2.9. Accordingly, ‘simple’ static UV absorption spectroscopy is not a suitable tool for monitoring the integrity of G containing DNA samples.

2.4.3 DNA Single and Double Strands

In general, specific problems have to be addressed, if experiments are carried out on synthesized DNA single and double strands or if isolated non-artificial DNA sample systems are investigated. Controlling the quality of the samples is of crucial importance. The oligo- or polynucleotides can be destroyed by DNA nuclease, which is an enzyme capable of cleaving the phosphodiester bonds between the nucleotide subunits. This is especially the case, if the DNA samples are bought in solution and are stored at room temperature. Thus, it is best to obtain them as lyophilisates and to store them, especially the solutions, at -20°C to minimize the activity of DNA nuclease.

Moreover, contaminations of the DNA sample batches has to be safely excluded. If DNA is isolated from living cells, it is difficult to separate the DNA polymer from other, often highly fluorescent elements of the cell, which could give overwhelming spectroscopic signals. Thus,

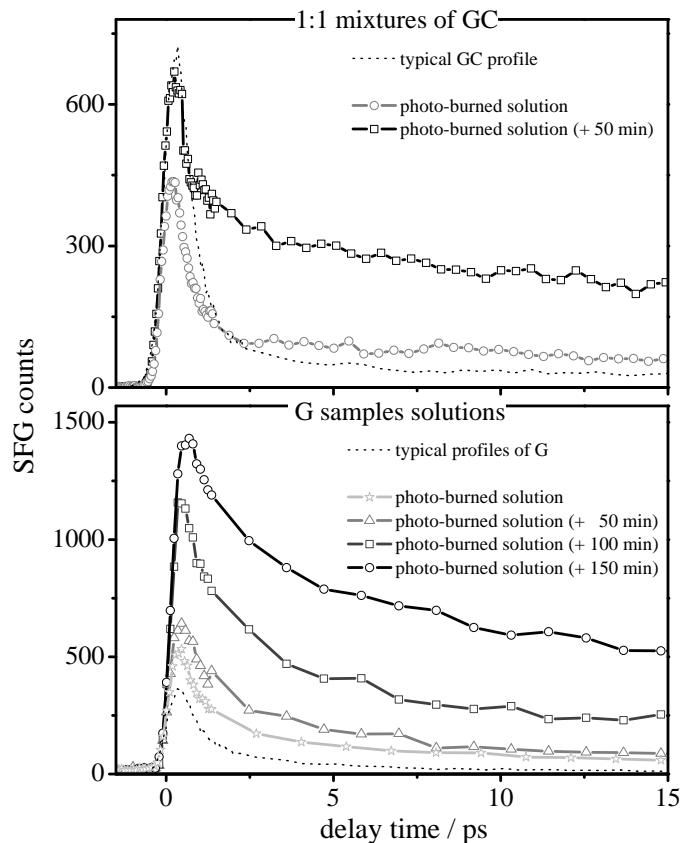


Figure 2.8: Fluorescence decay profiles of G (top) and GC (bottom) containing sample solutions after photo-induced damage

normally, differently sized DNA fragments with arbitrary base sequence are generated from an automated oligonucleotide synthesizer via solid phase phosphoramidite synthesis. This includes a number of work-up and standard purification steps, from which the desired pure oligonucleotides can be obtained in high quality ($\geq 95 - 98\%$ depending on the number of purification steps).

Nevertheless, there is still a remaining risk to obtain unwanted sideproducts:

(i) In majority, artificially produced oligonucleotides are used for biotechnological applications, for which they may carry specific fluorescence markers. Hence, traces of these dyes might be present in the eluent from a preceding synthesis on the same synthesizer. Those traces can dramatically effect stationary spectra. Transient spectroscopy, especially femtosecond fluorescence spectroscopy, is practically insensitive to these impurities, as dyes normally have long fluorescence lifetimes. In consequence, fluorescence photons are released on a nanosecond timescale and statistically, no photon is monitored in the detection window opened for the duration of the gate pulse.

(ii) However, the performed experiments are sensitive to biological contamination resulting from unwanted DNA side products, like fragments of shorter chain length. This is a fundamental point, especially if short oligonucleotide strands are synthesized. Oligonucleotides of relatively high chain length normally drop out from the eluent in the work-up procedure,

while short multimers, e.g., di-, tri- or tetramers, remain dissolved. This implies that low-molecular fragments can be dragged along the work-up and purification steps. In this case, and if oligonucleotides of relatively equal chain length have to be separated, it is inevitable to repeat the purification procedure several times, e.g., through double HPLC purification or through capillary electrophoresis.

In the present work, all DNA single and double strands were purchased from biomers.net GmbH (Ulm) as lyophilized sodium salts. The strands were synthesized following standard solid phase protocols. Thus, the deoxyribose oligonucleotides did not carry phosphates groups at the 3' and 5' terminals. Purification was carried out through a single run with high pressure liquid chromatography (HPLC). MALDI mass spectrometry was used for characterization.

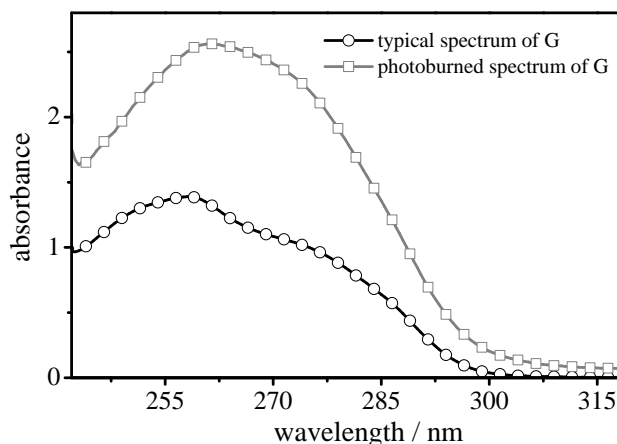


Figure 2.9: UV absorption spectrum of G after photo-induced damage

The optical density in the UV fluorescence up-conversion sample cell at the absorption maximum $\lambda_{abs,max}$ of each compound was $OD = 0.05 - 0.15$ at $c_0 = 0.1$ mM and ten times higher for measurements performed at $c_0 = 1$ mM. Accordingly, the optical density for excitation close to the electronic origin ($\lambda_{pump} = 296$ nm) was not more than $OD = 0.01 - 0.03$.

Deoxyribose Oligonucleotides. Homopurine and -pyrimidine deoxyribose oligonucleotides with different base sequence were obtained in several batches of ≈ 0.8 μmol each. The sample material was dissolved in 20 – 30 mL of ultrapure water containing phosphate buffer (6 mM Na_2HPO_4 , 2 mM NaH_2PO_4 , pH 7.1) and 185 mM NaCl and 1 mM EDTA. Thus, the average optical density was ≈ 0.5 OD. All solutions were heated to 85 – 90°C for 10 min and were allowed to cool down to room temperature before any stationary or transient measurements were carried out. The average concentration was $c_0 = 0.023$ per deoxyribose oligonucleotide ($\equiv 0.46$ mM per base), which was determined via the standard protocol [25–27]. Duplexes were prepared by mixing equimolar solutions of the respective single strands. Each deoxyribose oligonucleotide faced only 0.5 pump photons during the UV fluorescence up-conversion measurements (≈ 40 min) to ensure that the formation of photoproducts was prevented.

Stationary UV absorption spectroscopy, including the monitoring of the respective melting curves of the duplexes, as well as circular dichroism (CD) spectroscopy have been used to characterize the single and double strands.

Self-complementary Deoxyribose Oligonucleotide Loop. A self-complementary oligonucleotide loop 5'-GpGpGp-S-pCpCpC-3' (S \equiv hexaethyleneglycol) as well as 5'-GpGpG-3' trimer were obtained in a batch of $\approx 1 \mu\text{mol}$, respectively. Both were dissolved in 100 mL of ultrapure water containing a Na^+/K^+ phosphate buffer (1 \times PBS), which gave initial concentrations of $c_0 = 0.01 \mu\text{M}$. Thus, 0.4 photons were absorbed per oligonucleotide in a measurement of 1h duration.

The formation of the self-complementary duplex structure was monitored with temperature dependent UV absorption and CD spectroscopy as well as through correlated ^1H NMR (TOCSY, NOESY) measurements.

2.5 Stationary Spectroscopy

2.5.1 Stationary UV Absorption Spectroscopy.

UV absorption spectra and melting curves of the DNA samples were measured on a Shimadzu UV-2401 desktop spectrometer. The optical density at the respective absorption maxima of the samples ($\lambda_{abs,max}$) was adjusted to 0.5 – 1.5 OD. Thus, cuvettes of different pathlength ($l = 0.01, 0.1$ and 1 cm) were used in concentration dependent measurements (nucleobase monomers, but especially nucleobase pairs). Otherwise, measurements were carried out with diluted solutions (DNA single and double strands). Temperature-dependent measurements were carried out in a thermostated 1 cm cuvette. The respective neat solvent or buffer solution was taken as the background before each measurement and was automatically subtracted from the sample spectra.

2.5.2 Stationary UV Fluorescence Spectroscopy.

Fluorescence spectra were measured on a Horiba Jobin Yvon Fluoromax 4 spectrometer. 3D scans of the fluorescence spectra were performed at different excitation wavelengths λ_{ex} , which were chosen to match the wavelength of the pump pulses (λ_{pump}) used in the UV fluorescence up-conversion experiments. The same 3D scan was performed on the neat solvent/buffer solution to determine the respective background spectra, which were subtracted from the sample spectra in the subsequent data analysis. A Schott WG 295 filter was used to block scattered Rayleigh and Raman light. Measurements on the nucleobase monomers (e.g., DMA) were carried out in standard 90° detection geometry with highly diluted sample solutions. When the sample concentrations had to be kept high (e.g., for nucleobase pairs), the fluorescence spectra were recorded in reflection mode (45° detection geometry) to avoid inner filtering effects. Measurements of the monophosphates

at different concentrations in water at 90° and at 45° verified that the band shapes were reproduced correctly.

2.5.3 Stationary Circular Dichroism Spectroscopy

CD spectra were recorded at room temperature on a JASCO J-715 spectrometer in cuvettes of $l = 0.1$ and 1 cm pathlength. The cuvettes were chosen to give optical densities of $\approx 0.5 - 1.5$. The respective neat solvent or buffer was measured before and after each period of measurements and was subsequently subtracted.

2.5.4 Stationary FTIR Spectroscopy

FTIR spectra of the hydrogen-bonded nucleobase pairs were taken on a Bruker IFS 66v spectrometer at room temperature at different initial concentrations. Cuvettes of variable pathlength ($l = 0.1 - 2$ mm) equipped with CaF₂ windows were used. The exact pathlength was determined from the interferogram of the empty cuvette. The sample compartment of the FTIR spectrometer was flushed with dry N₂ to minimize atmospheric H₂O and CO₂ absorptions. All solutions were prepared just before their use. Low-concentration samples were obtained by diluting a common parent solution. Measurements were started from the lowest c_0 . The background of the solvent was taken before each set of measurements and automatically subtracted from each spectrum.

The association constants K_i of the homo- ($i = MM$) and heterodimers ($i = MN$) were determined from the concentration-dependent FTIR spectra. Through $c_0 = [M] + 2 [MM]$, K_{MM} is defined as

$$K_{MM} = \frac{[MM]}{[M]^2} = \frac{\beta_{MM}}{2c_0(1 - \beta_{MM})^2} \quad (2.34)$$

with β_{MM} begin the degree of self-association of monomers to a homodimer, given by

$$\begin{aligned} \beta_{MM} &= \frac{c_0 - [M]}{c_0} = \frac{2 [MM]}{c_0} \\ &= \frac{1 + 4 \cdot K_{MM} \cdot c_{0,MM} - \sqrt{1 + 8 \cdot K_{MM} \cdot c_{0,MM}}}{4 \cdot c_{0,MM}}. \end{aligned} \quad (2.35)$$

Accordingly, for an equimolar mixture of the two nucleobases M and N ($[M] = [N]$), K_{MN} is specified by

$$K_{MN} = \frac{[MN]}{[M][N]} = \frac{\beta_{MN}}{c_0(1 - \beta_{MN})^2}, \quad (2.36)$$

where $c_0 = [M] + [MN]$. The degree of association β_{MN} is then given by

$$\begin{aligned} \beta_{MN} &= \frac{c_0 - [M]}{c_0} = \frac{c_0 - [N]}{c_0} = \frac{[MN]}{c_0} \\ &= \frac{1 + 2 \cdot K_{MN} \cdot c_{0,MN} - \sqrt{1 + 4 \cdot K_{MN} \cdot c_{0,MN}}}{2 \cdot c_{0,MN}}. \end{aligned} \quad (2.37)$$

Towards these ends, the spectral contributions of the monomer ($i = M, N$) and dimer ($i = MM, MN$) bands, given by ϵ_i , respectively, were each modeled by using a number of Gaussian basis functions with center frequencies $\omega_{0,i}$, widths σ_i , and amplitudes A_i . The monomer and dimer spectra were coupled by the respective degrees of association β_i or, if desired, directly by K_i :

$$\epsilon(\omega) = b + [2 \cdot (1 - \beta_{MM})\epsilon_M(\omega) - \beta_{MM} \cdot \epsilon_{MM}(\omega)], \quad (2.38)$$

and

$$\epsilon(\omega) = b + [(1 - \beta_{MN})(\epsilon_M(\omega) + \epsilon_N(\omega) - \beta_{MN} \cdot \epsilon_{MN}(\omega))], \quad (2.39)$$

The parameter b was added as a fixed background term. All other parameters appearing in $\epsilon(\omega)$ were then determined by a simultaneous, global fit to all observed spectra using a nonlinear least-squares routine based on the Levenberg-Marquardt algorithm written in MATHEMATICA software [12]. All parameters were free-floating.

2.5.5 Stationary NMR Spectroscopy

Standard ^1H -NMR spectra were measured in the Otto-Diels Institute of Organic Chemistry at Kiel University. Spectra of the specially protected nucleobases were taken on a Bruker ARX300 and Bruker DRX500 to control their purity.

Moreover, 2D correlated (TOCSY and NOESY) ^1H -NMR spectra of the self-complementary deoxyribose oligonucleotide loop were recorded in ongoing studies by F. Sönnichsen (Otto-Diels Institute of Organic Chemistry at Kiel University) on a Bruker Avance 600 instrument to determine the structure of the loop from the resulting coupled spectral signatures. The field gradients were chosen to give an adequate suppression of H_2O signals. Temperature-dependent spectra were carried out with a cryostat sample holder ($-5^\circ\text{C} \leq T \leq 60^\circ$).

References and Notes

- [1] W. Demtröder, *Laserspektroskopie, Grundlagen und Techniken* (Springer-Verlag, Berlin, Heidelberg, New York, 2000).
- [2] R. Paschotta, *Encyclopedia of Laser Physics and Technology* (Wiley-VCH, Berlin, 2008).
- [3] L. Zhao, J. L. P. Lustres, V. Farztdinov, N. P. Ernsting, *Phys. Chem. Chem. Phys.* **7**, 1716 (2005).
- [4] T. Wilhelm, J. Piel, E. Riedle, *Opt. Lett.* **22**, 1494 (1997).
- [5] H. R. Schanz, S. A. Kovalenko, V. Kharlanov, N. P. Ernsting, *Appl. Phys. Lett.* **79**, 566 (2001).
- [6] H. Murakami, *Rev. Sci. Instrum.* **77**, 113105 1 (2006).
- [7] *Lab View SOFTWARE 8.0* (National Instruments, Corp., 2006).
- [8] *Lab View SOFTWARE 8.5* (National Instruments, Corp., 2008).
- [9] A. Cannizzo *et al.*, *Opt. Lett.* **32**, 3555 (2007).
- [10] B. Schmidt, S. Laimgruber, W. Zinth, P. Gilch, *Appl. Phys. B* **76**, 809 (2003).
- [11] S. Arzhantsev, M. Maroncelli, *Appl. Spec.* **59**, 206 (2005).
- [12] Wolfram Research, *Mathematica Version 6.0* (Wolfram Research, 2007).
- [13] M. Maroncelli, G. R. Fleming, *J. Chem. Phys.* **86**, 6221 (1987).
- [14] N. Eilers-König, T. Kühne, D. Schwarzer, P. Vöhringer, J. Schroeder, *Chem. Phys. Lett.* **253**, 69 (1996).
- [15] S. K. Pal, J. Peon, A. H. Zewail, *Chem. Phys. Lett.* **363**, 57 (2002).
- [16] N. K. Schwalb, *Time-Resolved Femtosecond Fluorescence Spectroscopy of N^6, N^6 -Dimethyladenine* (Diploma Thesis, Christian-Albrechts-University, Kiel, 2005).
- [17] N. K. Schwalb, F. Temps, *Phys. Chem. Chem. Phys.* **8**, 5229 (2006).
- [18] Y. Kyogoku, R. C. Lord, A. Rich, *Science* **154**, 518 (1966).
- [19] P. Carmona, M. Molina, A. Lasagabaster, R. Excoibar, A. B. Altabef, *J. Phys. Chem.* **97**, 9519 (1993).
- [20] T. Michalak, *Characterization of Cytisine and H-bonded Cytidine Dimers in Solution by FTIR Spectroscopy and Quantum Chemical Calculations* (Diploma Thesis, Christian-Albrechts-University, 2007).
- [21] L. Biemann, T. Häber, D. Maydt, K. Schaper, K. Kleineremanns, *J. Chem. Phys.* **128**, 195103 (2008).
- [22] T. Michalak, N. K. Schwalb, J. Gripp, F. Temps, *Spectrochim. Acta A* (submitted, 2009).
- [23] K. Siriwong, A. A. Voityuk, M. D. Newton, N. Rösch, *J. Phys. Chem. B* **107**, 2595 (2003).
- [24] T. Michalak, N. K. Schwalb, J. Gripp, F. Temps, *manuscript in preparation* (2009).

- [25] V. A. Bloomfield, D. M. Crothers, I. Tinoco, *Nucleic Acids: Structures, Properties and Functions* (University Science Books, Sausalito, 2000).
- [26] C. R. Cantor, M. M. Warshaw, H. Shapiro, *Biopolymers* **9**, 1059 (1970).
- [27] M. J. Cavalluzzi, P. N. Borer, *Nucl. Acids Res.* **32**, e13 (2004).

Chapter 3

Femtosecond Time-Resolved Fluorescence Spectroscopy of N^6,N^6 -Dimethyladenine: New Explanation of the “Dual Fluorescence” Dynamics from Decay and Rise Time Measurements at Threshold

Nina K. Schwalb,* Friedrich Temps

Institut für Physikalische Chemie, Christian-Albrechts-Universität zu Kiel,
Olshausenstr. 40, D-24098 Kiel, Germany

*To whom correspondence should be addressed.

E-mail: schwalb@phc.uni-kiel.de

Springer Series in Chemical Physics, Vol. 92:
Ultrafast Phenomena XVI, publication date: July 7, **2009**.

Abstract

Femtosecond time-resolved fluorescence measurements on N^6,N^6 -dimethyladenine in a wide wavelength range following excitation at threshold and much higher show identical dynamics, requiring a new explanation for the so-called “dual fluorescence” of the molecule.

Copyright 2009 Springer-Verlag GmbH, Heidelberg.

Chapter 4

A Modified Four-State Model for the “Dual Fluorescence” of N^6,N^6 -Dimethyladenine derived from Femtosecond Fluorescence Spectroscopy

Nina K. Schwalb,* Friedrich Temps*

Institut für Physikalische Chemie, Christian-Albrechts-Universität zu Kiel,
Olshausenstr. 40, D-24098 Kiel, Germany

*To whom correspondence should be addressed.
E-mail: schwalb@phc.uni-kiel.de, temps@phc.uni-kiel.de.

J. Phys. Chem. A **2009**,
Robert W. Field Festschrift,
accepted and in press.

Abstract

The radiationless deactivation of the excited electronic states of the dual fluorescence molecule N^6,N^6 -dimethyladenine (DMAde) was investigated using femtosecond time-resolved fluorescence up-conversion spectroscopy. The molecules were studied in solution in water and in dioxane. Fluorescence-time profiles were recorded in the wide wavelength range from $290 \text{ nm} \leq \lambda_{fl} \leq 650 \text{ nm}$. The excitation wavelengths in the region of the first UV absorption band were tuned from close to the electronic origin ($\lambda_{pump} = 294 \text{ nm}$) to excess energies of $\approx 5400 \text{ cm}^{-1}$ above ($\lambda_{pump} = 258 \text{ nm}$). Global fits to the measured curves turned out to reflect distinctive molecular relaxation processes on five well-defined time scales. Sub-100 fs and 0.52(3) ps lifetimes were found to predominate at the shortest UV and blue emission wavelengths in water, 1.5(1) and 3.0(2) ps components at intermediate wavelengths, and a 62(1) ps value in the red region of the spectrum (2σ error limits of last digits in parentheses). In dioxane, these lifetimes changed to $\leq 0.27 \text{ ps}$ and 0.63(4) ps at UV, 1.5(1) and 10.9(10) ps in a wide range of intermediate, and 1.40(4) ns at the longest wavelengths. However, little dependence of the respective time constants on λ_{pump} was observed, indicating that the ensuing relaxation processes proceed via practically barrierless pathways through conical intersections. Building on the knowledge for the parent molecule adenine (Ade), the observations were rationalized with the help of a modified four-state model for the electronic dynamics in DMAde with the $\pi\pi^*(L_a)$, $\pi\pi^*(L_b)$, and $n\pi^*$ states similar as in Ade and an intramolecular charge transfer (ICT) state, which has no counterpart in Ade, responsible for the long-wavelength fluorescence.

Keywords: *Dual Fluorescence; Nucleic Acid Bases; DNA; Electronic Relaxation; Radiationless Processes; Intramolecular Charge Transfer.*

Chapter 5

Ultrafast Electronic Relaxation in Guanosine is Promoted by Hydrogen Bonding with Cytidine

Nina K. Schwalb,* Friedrich Temps*

Institut für Physikalische Chemie, Christian-Albrechts-Universität zu Kiel,
Olshausenstr. 40, D-24098 Kiel, Germany

*To whom correspondence should be addressed.
E-mail: schwalb@phc.uni-kiel.de, temps@phc.uni-kiel.de.

J. Am. Chem. Soc. **2007**, *129*, 9272-9273.

Abstract

The excited electronic state lifetime of the guanosine-cytidine (G···C) Watson-Crick (WC) base pair has been directly measured in comparison to free G and C. Measurements have been carried out in solution in chloroform, where the formation of H-bonded base pairs is strongly favored, using the technique of femtosecond fluorescence up-conversion spectroscopy. The results show that the formation of the H-bonded WC pair leads to steep acceleration of the ultrafast nonradiative electronic deactivation compared to the free nucleosides, especially G, which can be explained by an intermolecular G-to-C electron-induced proton-transfer mechanism in the excited state. The results are of vital interest for bridging the huge gap between the well-known electronic properties of the isolated nucleobases and the strikingly different dynamics of DNA molecules.

Copyright 2007 ACS American Chemical Society.

Supporting Information

Ultrafast Electronic Relaxation in Guanosine is Promoted by Hydrogen Bonding with Cytidin

Nina K. Schwalb, Friedrich Temps

Institut für Physikalische Chemie, Christian-Albrechts-Universität zu Kiel,
Olshausenstr. 40, D-24098 Kiel, Germany

E-mail: schwalb@phc.uni-kiel.de, temps@phc.uni-kiel.de.

Copyright 2007 ACS American Chemical Society.

Chapter 6

Ultrashort Fluorescence Lifetimes of Hydrogen-Bonded Base Pairs of Guanosine and Cytidine in Solution

Nina K. Schwalb,* Friedrich Temps*

Institut für Physikalische Chemie, Christian-Albrechts-Universität zu Kiel,
Olshausenstr. 40, D-24098 Kiel, Germany

*To whom correspondence should be addressed.
E-mail: schwalb@phc.uni-kiel.de, temps@phc.uni-kiel.de.

submitted.

Abstract

The optically excited electronic states of hydrogen-bonded homo- and heterodimers of guanosine (G) and deoxycytidine (C) were investigated by femtosecond fluorescence up-conversion spectroscopy. The base pairs were prepared in CHCl_3 solution by employing *tert*-butyldimethylsilyl (TBDMS) groups at the OH positions of the ribose (G) or deoxyribose (C) moieties to enhance the solubilities of the nucleosides in organic solvents. The H-bonded complexes that were obtained were characterized by FTIR spectroscopy. Fluorescence lifetime measurements were performed following electronic excitation at a series of UV wavelengths from $\lambda_{\text{pump}} = 294$ nm, close to the electronic origins of the bases, to $\lambda_{\text{pump}} = 262$ nm, where significant excess vibronic energy is deposited in the molecules, at nucleoside concentrations of $c_0 = 0.1$ and 1.0 mM. The experimental results revealed the existence of an ultrafast deactivation pathway for the electronically excited G·C Watson-Crick base pair, which was found to have a lifetime of $\tau_{\text{GC}} = 0.30(3)$ ps (with 2σ error limits) irrespective of the pump wavelength. A similar short decay time, $\tau_{\text{GG}} = 0.32(2)$ ps, was observed for the G·G homodimer. In contrast, the G monomer displayed a significantly longer-lived and wavelength-dependent deactivation, requiring three time constants, between $0.43(6)$ ps $\leq \tau_{\text{G},1} \leq 1.2(1)$ ps, $4.2(8)$ ps $\leq \tau_{\text{G},2} \leq 8(1)$ ps, and $\tau_{\text{G},3} = 195(32)$ ps. Self-complexation of C, on the other hand, led to a longer-lived excited state with a lifetime estimated between 1 ps $\leq \tau_{\text{CC}} \leq 10$ ps, compared to the dominant initial sub-picosecond decay time of the C monomer of $\tau_{\text{C},1} = 0.80(4)$ ps.

Keywords: *Ultrafast electronic deactivation; photostability; hydrogen bonding; DNA; guanosine; cytidine; Watson-Crick base pairs; UV fluorescence up-conversion spectroscopy.*

Unpublished work copyright 2009, submitted for publication.

Chapter 7

A Combined FTIR and DFT Study of Hydrogen-Bonded Complexes of Cytidine in Solution

T. Michalak, Nina K. Schwalb, J. Gripp, Friedrich Temps*

Institut für Physikalische Chemie, Christian-Albrechts-Universität zu Kiel,
Olshausenstr. 40, D-24098 Kiel, Germany

*To whom correspondence should be addressed.
E-mail: temps@phc.uni-kiel.de.

submitted.

Abstract

Hydrogen-bonded aggregates of 2'-deoxycytidine were studied by FTIR spectroscopy and complementary DFT calculations in solution in the aprotic solvent CHCl_3 , where formation of H-bonded complexes is strongly favored. Vibrational bands in the NH stretch and in the CO stretch/ NH_2 bend spectral regions belonging to monomers and dimers were identified by their concentration dependences, dependences on temperature, and spectral band fitting. The dimer equilibrium constant was derived by a global fit to the spectra in the NH stretch region versus concentration. The analysis of the spectra was complemented by G3B3 calculations of the Gibbs free enthalpies of the pertinent tautomers and by DFT calculations of the binding energies for the H-bonded complexes and the vibrational frequencies of the monomers and dimers at the PW91/6-311⁺⁺G(d,p) and TPSS/cc-pVTZ levels of theory with account of the solvent by the polarizable continuum model (PCM). Comparisons of the experimental and calculated vibrational frequencies, which were in excellent agreement, led to firm assignments of the measured monomers and dimers. Spectra of larger complexes (trimers, tetramers) were observed in CCl_4 . The applied combination of tools is well suited for studies of other H-bonded nucleobase aggregates, including distinctive isomers, complexes with noncanonical configurations, and heterodimers composed of two different bases.

Keywords: *Cytidine; Tautomers; Nucleic Acid Base Pairs; Hydrogen Bonding.*

Unpublished work copyright 2009 submitted for publication.

Supporting Information

A Combined FTIR and DFT Study of Hydrogen-Bonded Complexes of Cytidine and in Solution

T. Michalak, Nina K. Schwalb, J. Gripp, Friedrich Temps

Institut für Physikalische Chemie, Christian-Albrechts-Universität zu Kiel,
Olshausenstr. 40, D-24098 Kiel, Germany

E-mail: temps@phc.uni-kiel.de.

Unpublished work copyright 2007, submitted for publication.

Chapter 8

On the Structure and Photostability of Cytosine Self-Assemblies with Extended Hydrogen-Bonding Networks

Nina K. Schwalb,* Friedrich Temps*

Institut für Physikalische Chemie, Christian-Albrechts-Universität zu Kiel,
Olshausenstr. 40, D-24098 Kiel, Germany

*To whom correspondence should be addressed.
E-mail: schwalb@phc.uni-kiel.de, temps@phc.uni-kiel.de.

submitted.

Abstract

The nucleoside cytidine (C) assembles in hydrogen-bonded cyclic aggregates in neat apolar solvents like *n*-hexane, when carrying inert hydrophobic groups at the 2',3',5'-oxygen atoms of the ribose moiety. The ensuing structures, which constitute model systems for DNA super-structures such as triplexes or quadruplexes, were elucidated by FTIR spectroscopy and further characterized by UV spectroscopy. The lifetimes of the optically excited electronic states of the aggregates were investigated using femtosecond UV fluorescence up-conversion spectroscopy. Time profiles were measured after excitation at a number of pump wavelengths between $296 \text{ nm} \geq \lambda_{\text{pump}} \geq 262 \text{ nm}$. The bi-exponential decay curves were characterized by time constants (with 2σ error limits) of $\tau_{1,\text{C}} = 0.58(1)$ ps (88 – 95 %) and $\tau_{2,\text{C}} = 19.4(13)$ ps (12 – 5 %) independent of the pump wavelength. The results indicate that the C multimers do not gain photostability by their extended H-bonded networks. This was already observed for the H-bonded C·C dimer and the G-tetrad studied previously, but contrasts with recent other findings for the G·G and G·C dimers.

Keywords: *Cytidine; DNA Base Pairs; Hydrogen Bonding; Self-Assembly; Fluorescence; Electronic Relaxation; Radiationless Transitions.*

Unpublished work copyright 2009, submitted for publication.

Chapter 9

Spectra and Dynamics of the G-Tetrad, a Model for G-Quadruplex DNA

Nina K. Schwalb,* Friedrich Temps*

Institut für Physikalische Chemie, Christian-Albrechts-Universität zu Kiel,
Olshausenstr. 40, D-24098 Kiel, Germany

*To whom correspondence should be addressed.
E-mail: schwalb@phc.uni-kiel.de, temps@phc.uni-kiel.de.

submitted.

Abstract

The nucleoside guanosine (G) forms a hydrogen-bonded cyclic tetramer, which constitutes the structural motif of the well-known G-quadruplex DNA encountered in the centromeres and telomeres of the genome. We show that the G-tetrad can be prepared in neat nonpolar solvents by using a derivative of guanosine carrying inert hydrophobic groups at the 2',3',5'-O atoms. The ensuing structure was elucidated by FTIR spectroscopy. Measurements of the UV and CD spectra revealed significant couplings of the chromophores in the tetrad, as is known for G-quadruplex DNA. The ultrafast dynamics of the excited electronic states of the G-tetrad were investigated in *n*-hexane solution using the femtosecond UV fluorescence up-conversion technique. Time profiles of the fluorescence were measured at two different monomer concentrations ($c_0 = 0.1$ and 1.0 mM) after excitation at pump wavelengths ranging between $296 \text{ nm} \geq \lambda_{pump} \geq 262 \text{ nm}$. The results indicate that the G-tetrad does not gain photostability by the extended H-bonded network, in contrast to the dimers G·G and G·C studied previously. Instead, the fluorescence lifetimes were found to be even longer than for the G monomer. Fits to the observed time profiles required three exponentials, with a main decay constant of $\tau_{1,G} = 0.63(4)$ ps (69 %) and two smaller components of $\tau_{2,G} = 8.4(4)$ ps (22 %) and $\tau_{3,G} = 114(9)$ ps (9 %). The $\tau_{1,G}$ value doubled, when the tetrad was excited at $\lambda_{pump} = 296$ nm, close to the electronic origin.

Unpublished work copyright 2009 submitted for publication.

Chapter 10

Base Sequence and Higher-order Structure Induce the Complex Excited-State Dynamics in DNA

Nina K. Schwalb,* Friedrich Temps*

Institut für Physikalische Chemie, Christian-Albrechts-Universität zu Kiel,
Olshausenstr. 40, D-24098 Kiel, Germany

*To whom correspondence should be addressed.
E-mail: schwalb@phc.uni-kiel.de, temps@phc.uni-kiel.de.

Science **2008**, *329*, 243-245.

Abstract

The high photostability of DNA is commonly attributed to efficient radiationless electronic relaxation processes. We used femtosecond time-resolved fluorescence spectroscopy to reveal that the ensuing dynamics are strongly dependent on base sequence and are also affected by higher-order structure. Excited electronic state lifetimes in dG-doped d(A)₂₀ single-stranded DNA and dG·dC-doped d(A)₂₀·d(T)₂₀ double-stranded DNA decrease sharply with the substitution of only a few bases. In duplexes containing d(AGA)·d(TCT) or d(AG)·d(TC) repeats, deactivation of the fluorescing states occurs on the subpicosecond time scale, but the excited-state lifetimes increase again in extended d(G) runs. The results point at more complex and molecule-specific photodynamics in native DNA than may be evident in simpler model systems.

Copyright 2008 AAAS American Association for the Advancement of Science.

Supporting Information

Base sequence and higher-order structure induce the complex
excited-state dynamics in DNA

Nina K. Schwalb, Friedrich Temps

Institut für Physikalische Chemie, Christian-Albrechts-Universität zu Kiel,
Olshausenstr. 40, D-24098 Kiel, Germany

E-mail: schwalb@phc.uni-kiel.de, temps@phc.uni-kiel.de.

Copyright 2008 AAAS American Association for the Advancement of Science.

Chapter 11

Concluding Discussion

In the present *Thesis*, femtosecond UV fluorescence spectroscopy was used to investigate the ultrafast electronic deactivation dynamics of low-fluorescent DNA model systems, which exhibit fluorescence quantum yields of $\Phi_{fl} \leq 10^{-4}$. Following a bottom-up strategy, comprehensive studies have been performed on free DNA monomers and nucleobase derivatives, on isolated hydrogen-bonded Watson-Crick (WC) and non-WC nucleobase pairs as well as on higher H-bridged aggregates, and on short DNA single and double strands and self-complementary oligomer loops.

The aim of the *Thesis* was to elucidate in some detail the photodynamics of selected DNA model systems and their underlying building blocks and to clarify the competing roles of essential structural elements, like nucleobase pairs and stacks. The obtained state-of-the-art results contribute to our fundamental understanding of the photodynamics of DNA.

The applied experimental setup displayed an extraordinarily high sensitivity. It was possible to monitor single UV fluorescence photons, even when the optical density of the photo-excited DNA sample solutions was less than $OD = 0.01$. Furthermore, so-called ‘optically dark’ and practically ‘non-radiative’ intermediate excited states of low oscillator strength became observable. Hence, the setup has turned out to be a very powerful tool. It monitored the fluorescence decays of the photo-excited state(s), which directly returned the lifetimes of the optically excited states of the investigated DNA building blocks, without interference through additional and sometimes masking signals like overlapping electronic ground state and multiple (interwoven) excited-state effects.

11.1 Fluorescence Decays of DNA Monomers

The previously reported photodynamic research on isolated DNA bases had drawn a partially incomplete picture of the electronic deactivation dynamics of monomeric nucleobases. In fact, comprehensive studies have been performed [1], in majority with the transient absorption technique. But practically in all cases, the dynamics were monitored after excitation high above the electronic origin, as the third harmonic of the laser fundamental was used as the pump pulse. Thus, high vibrational excess energy was available in the photo-excited molecules, which made it impossible to monitor essential dynamic processes close to the electronic origin(s) of the involved excited-state(s). Possible potential energy barriers en route the MEP(s) could not be detected. Thus, the data needed for a full understanding of the electronic deactivation mechanisms in free nucleobases were incomplete.

These questions have been addressed in the present *Thesis*. Although the focus of this study was set on nucleobase assemblies, measurements on the electronic deactivation dynamics of all four free deoxyribose monophosphates were carried out in parallel to gain reference values. They have been described in *Chapter 10* and in the *Appendix*. Moreover, a comprehensive study on specially protected G and C nucleosides was performed, which has been described in *Chapters 5* and *6*. The electronic relaxation dynamics have been measured in water and in different organic solvent (i.e., dioxane and chloroform) after photo-excitation

at wavelengths between $258 \text{ nm} \leq \lambda_{\text{pump}} \leq 296 \text{ nm}$. The results demonstrate that different relaxation pathways are accessible from the optically prepared FC region in dependence on the excess energy available. It was found that always more than one excited-state surface is responsible for the observed dynamics and that spectroscopically dark states are involved as intermediates.

The most prominent example for a nucleobase monomer, which exhibits a multiple excited-state topology and thus displayed tremendously altered fluorescence decay profiles, was DMA, which is a closely related derivative of the naturally occurring nucleobase A (see Chapters 3 and 4).

The obtained data on the DNA monomers are most helpful for theoretical chemists, who perform high-level ab-initio calculations on the relaxation pathways of the free nucleobases, including their specific MEPs, possible transition states (TS), reaction barriers and CIs. Part of the published theoretical works is still debatable as corresponding experimental data were missing.

11.2 Fluorescence Decay Dynamics of H-Bonded DNA Base Pairs and Self-Assemblies

The electronic dynamics occurring in DNA base pairs, which constitute a fundamental structural elements of DNA, have been studied individually in detail. The obtained data were found to be essential to assess the role of hydrogen-bonding dynamics for the electronic deactivation of the DNA double helix. Corresponding data have been missing completely as the relevance of the ‘pairing effect’ has not been addressed in earlier studies on the photostability of complex DNA systems.

The main focus in the studies on DNA base pairs was set on heterodimer formation, especially on the hydrogen-bonded $\text{G} \cdots \text{C}$ WC base pair. Aside, non-complementary homodimer formation, leading to a symmetric $\text{C} \cdots \text{C}$ base pair and the $\text{G} \cdots \text{G}$ Hoogsteen base pair were studied.

Complementary, and in special cases, even non-complementary base pairing motifs displays a key feature for the shape and function of DNA and are therefore of crucial biological importance. The hydrogen bonds of the WC scheme stabilize the double helical structure and, moreover, participate in the fundamental processes of DNA replication and gene expression. Non-WC pairs, e.g. $\text{G} \cdots \text{G}$ pairing motifs, have been found to be essential for the formation of DNA super-structures (DNA tri- and quadruplexes) and play a role in cell division (mitosis and meiosis) and programmed cell death (apoptosis).

As described in the preceding chapters, isolated DNA base pairs are not formed in aqueous solution. Therefore, suitable (not commercially available) nucleoside building blocks were synthesized and characterized in a comprehensive way (Chapters 5, 6, 7, 8 and 9).

The results obtained by the femtosecond UV fluorescence up-conversion experiment unambiguously demonstrate that, compared to the dynamics of the underlying free nucleosides, the excited-state lifetime is dramatically reduced upon complementary hydrogen-bonding in the G···C WC base pair [2, 3]. The effect was most pronounced for G, which is rather long-lived in its monomeric form and, thus, a G-to-C mechanism could be assumed. The observed dynamics were found to be independent on the vibrational excess energy deposited into the sample molecules after photo-excitation close to their excited-state electronic origin ($\lambda_{pump} = 290 - 296$ nm) or high above ($\lambda_{pump} = 262 - 283$ nm). This was interpreted as a hint for the existence of a single and globally active deactivation pathway, which is easily accessible from the spectroscopically prepared FC region and which leads to an ultrafast recovery of the initial WC ground state. The triply hydrogen-bonded G···C pair was not found to dissociate upon electronic excitation. However, it could not be ruled out, whether the observed ultrafast process are related to structural features like H-movement(s), including an interim partial breaking and (re-)making of hydrogen bonds, because the fluorescence up-conversion technique is not sensitive to vibrational fingerprints. Corresponding UV/IR pump-probe experiments are needed (and planned) to address this question. However, the experimental observations clearly pointed at an outstanding photodynamical role of the WC base pairing motif.

The experimental data on the G···C WC base pair are in agreement with theory, which suggested an intermolecular coupled electron-proton-transfer mechanism for the rapid and radiationless deactivation of isolated Watson-Crick base pairs [4–6]. The proposed mechanism includes an electron transfer from the highest occupied molecular orbital (HOMO, π) of the purine base into the lowest unoccupied molecular orbital (LUMO, π^*) of the pyrimidine base, which is immediately followed by a proton transfer along the central NH hydrogen bond of the base pair. Along the transfer coordinate, an extended CI seam [6] can be accessed, accounting for the extremely fast, nonradiative depopulation of the excited state.

The naturally occurring Hoogsteen G···G motif was found to profit in a related way from self-complexation, while a symmetric C···C base pair displays a rather long-lived electronic lifetime [3].

Similar, yet unpublished data were observed in corresponding experiments on A···T and 2AP···T containing homo- and hetero-base pairs [7]. These are briefly described in the *Appendix*.

Other basic hydrogen-bonded motifs of biologically relevant structures, i.e., subunits for DNA tri- and quadruplexes, were easily available by the above described procedure [8, 9]. A C-containing triad and a cyclic reverse-Hoogsteen H-bonded G tetrad were investigated in *n*-hexane solutions. Interestingly, none of these DNA super-structures gained photostability by their extended hydrogen-bond networks. Instead, they displayed long-lived fluorescence decay profiles. The tri- and quadruplex structures have not been investigated by direct means before to our knowledge, although they serve as key motifs for DNA

super-structures and connect the world of DNA/RNA to (quadruplex-specific) proteins. This opens the window to a rapidly growing research area of structural and molecular biology, medicinal chemistry and molecular pharmacology.

11.3 Short DNA Single Strands and Duplexes

The available information on DNA single and double strands was and is still limited. Earlier studies tried to shed light on the DNA building blocks in a top-down strategy. Here, DNA oligonucleotides with strand lengths of ≈ 20 nucleobase or even much higher (> 1000) have been studied [10–12].

Most of these studies were performed on A and T containing sequences, and the obtained results can not be generalized. Within this *Thesis*, through a strategically planned approach, many relevant effects of structural origin, namely base pairing, base stacking and secondary-order (i.e., conformational) effects were addressed successfully by investigations of DNA single and double strands of different base sequence [13]. The electronic relaxation in d(G)-doped d(A)₂₀ and in the corresponding, complementary d(C)-doped d(T)₂₀ DNA single strands as well as in the resulting d(G)·d(C)-doped d(A)₂₀·d(T)₂₀ DNA duplexes were investigated.

Comparably ‘simple’ results were obtained for the homopyrimidine single stands. The incorporated bases are barely stacked and the observed dynamics were rather monomer-like.

In contrast, pronounced stacking occurred in the homopurine single strands. For pure d(A) runs, the stacking was in B-DNA geometry and changed to a strongly stacked B/A-DNA intermediate type, as typically found in G-quadruplex structures, for pure d(G) repeats. Both ‘extrema’ have been found to be long-lived.¹ The substitution of every fifth, third or second base reduces the electronic lifetimes significantly. In mixed sequences of both purine bases, i.e., in AGA repeats, the shortest electronic lifetimes were found.

A similar behavior was found for the homopurine·homopyrimidine duplexes: Pure and highly stacked sequences are rather long-lived, but the excited-state relaxation accelerates upon base mixing. Additionally, a reduction of the electronic lifetime appears through H-bonding dynamics on complementary WC pairing via the G···C WC base pairs, i.e., for d(AGA)·d(TCT), d(AG)·d(TC) and pure d(G)·d(C) repeats. However, in the latter case, this effect is influenced by the change in the secondary structure from B- to B/A-type DNA. The observations point at the importance of the intermolecular coupled electron-proton-transfer mechanism, established for the isolated G···C WC base pair, as the driving force for the electronic deactivation at least in d(G)·d(C) rich sequences. In contrast, the dynamics in tracts of high d(A)·d(T) contents seem to be rather controlled by base stacking.

¹ Batches of pure d(A) runs might be contaminated with unwanted short-chain fragments like ApA (see Section 2.4.3 and [14]).

The results show that the photodynamics in native DNA are rather complex, molecule-specific and significantly controlled by the primary and secondary structure of DNA.

The experimentally obtained observations might be summed up in the schematical energy diagram given in Fig. 11.1. Due to strong cooperative couplings owing to the nearby chromophoric systems of the nucleobases incorporated in DNA, the photo-electronically active states of the individual nucleobases, especially of purine-rich tracts, might become highly delocalized over the full DNA system and might be shared by a number of different bases in an exciton-like fashion. Photo-excitation of these delocalized excitonic states primarily initiates photo-relaxation processes within the exciton band, which could be monitored approximately on a 0.5 – 1 ps timescale.

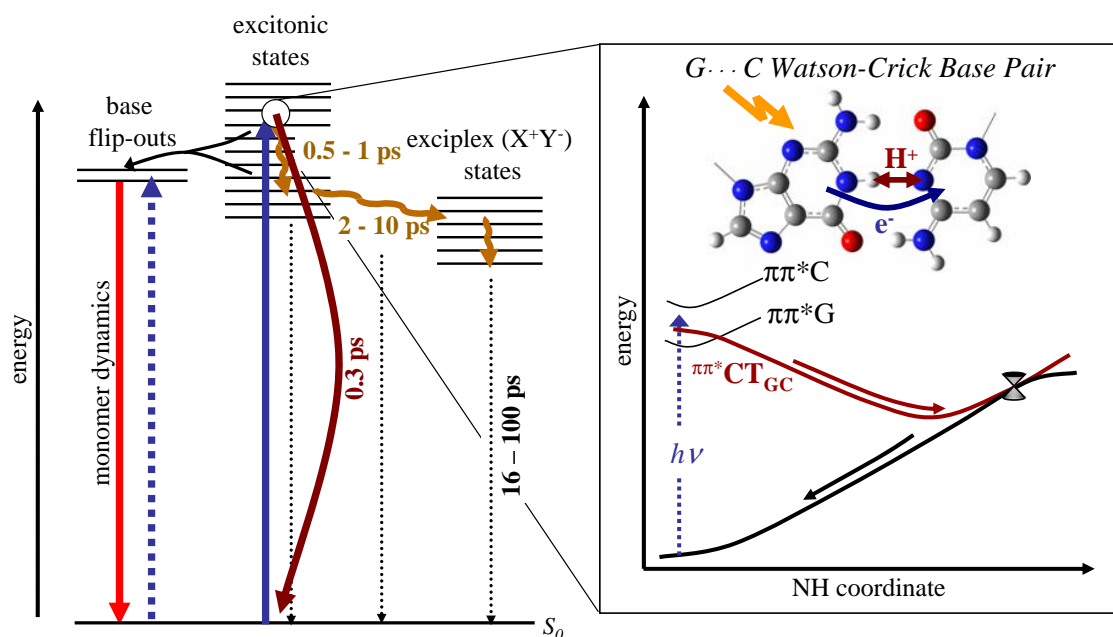


Fig. 11.1: Schematic energy diagram for the photodeactivation pathways in single- and double-stranded DNA oligomers.

Relaxed, and thus more localized excitonic states can couple in a certain region of the PEHS to the nearby, but optically forbidden CT states. These might result either from the CT transitions within the exciton band or from CT transitions between two nearby nucleobases in accordance to the frequently discussed DNA electron transfer processes, due to the different redox potentials of the bases. As the concerned conversion processes might possibly take place in a rather flat region of the PEHS, the observed fluorescence time components slow down to 2 – 10 ps. Deactivation from these dark CT states occurs in 16 – 100 picoseconds.

Finally, if the content of G-C base pairs in DNA oligomer duplexes is high, relaxation through the G-C-base-pair-related deactivation pathways on the 0.3 ps timescale is overriding.

However, as DNA is a flexible molecule, flipped out bases as well as insignificantly stacked DNA segments or runs (homopyrimidine sequences) may contribute to the overall fluorescence decay profiles in a rather monomer-like way.

11.4 Ongoing and Future Experimental Work

As demonstrated above, the photodynamics of DNA are multifaceted and cannot be attributed to a single deactivation mechanisms. In fact, it is rather the interplay of different structurally related processes, i.e., nucleobase pairing and stacking dynamics, which are altered by the higher-order structure of DNA. The results obtained within the present *Thesis* have established benchmarks for the understanding of photodynamical properties of DNA base pairs and short DNA single and double-stranded oligomers.

Nevertheless, it is inevitable to bridge the gap inbetween by investigating very short single- and double-stranded oligomers with 2 to 4 nucleobases. This allows us to address both fundamental structural key features, i.e., nucleobase pairs and stacks, in molecules of ‘manageable’ size, which lack the ‘winding effect’ of the higher-order structure and partially ‘circumvent’ the change of the stacking geometry (B- or B/A-stacking).

First experiments on commercially available di- and tetranucleotides single strands have been performed by the Kohler group with the transient absorption experiment at a fixed excitation wavelength of $\lambda_{pump} = 267$ nm [15, 16]. However, the full dynamics, including reaction barriers, transition states and CIs along all possible MEPs, can only be unraveled, if the excitation energy is varied over the full $\pi\pi^*$ -absorption bands of the DNA assemblies. The femtosecond fluorescence experiment allows for the detection the full photo-response of the DNA sample without suffering from interfering signals from hot-ground state and multiple excited-state absorptions and other coherent effects (SPM, XPM). In contrast to earlier assumptions [17], optically dark and practically non-emittive states, which act as intermediates in the electronic deactivation, can be detected, at least in the region where these states are coupled to the optically bright, photo-excited states. Additionally, the described experimental setup allows experiments on the sensitive and easily damaged biological sample materials to be carried out under very gentle conditions (≤ 50 nJ pump pulse power) with highly diluted sample concentrations ($OD < 0.01$).

Nevertheless, DNA duplex formation and stability requires a certain strand length. The limit is at a length of $\approx 7 - 8$ nucleobases for the strongly triple-hydrogen-bonded, purely d(G)·d(C) containing DNA strands. Thus, DNA duplexes with a reduced number of nucleobases are most difficult to prepare. Self-complementary oligonucleotide loops are commonly used to enforce duplex formation in strands with a low number of bases. For biochemical or biotechnological applications, such loops are made from a suitable self-looping DNA sequences. However, these are incompatible with photodynamical studies (although they have been used recently [15]), as the loop itself is sensitive to UV absorption. For the

same reason, stilbene which has been used in NMR studies of short self-complementary nucleobase triplets [18] is excluded.

In ongoing studies [19], it was shown that a very short G·C loop made up by only three complementary G·C WC base pairs was best prepared with an inert and non-absorbing hexaethyleneglycol spacer, which was chosen to guarantee self-complexation.

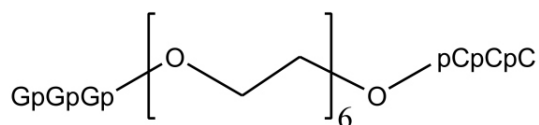


Fig. 11.2: Chemical structure of the G·C loop.

A sketch of the chemical structure of this loop is given in Fig. 11.2.

Static UV absorption and CD spectroscopy approved the folded structure of the loop. Fig. 11.3a displays the static UV absorption spectrum of the G·C loop compared to the spectra of its constituent G and C trinucleotides at room temperature. The respective sum of the two latter spectra is shown as well. All spectra were normalized at $\lambda = 260$ nm, which is a common procedure for DNA samples and which is indicated by a thin vertical black line in Fig. 11.3.

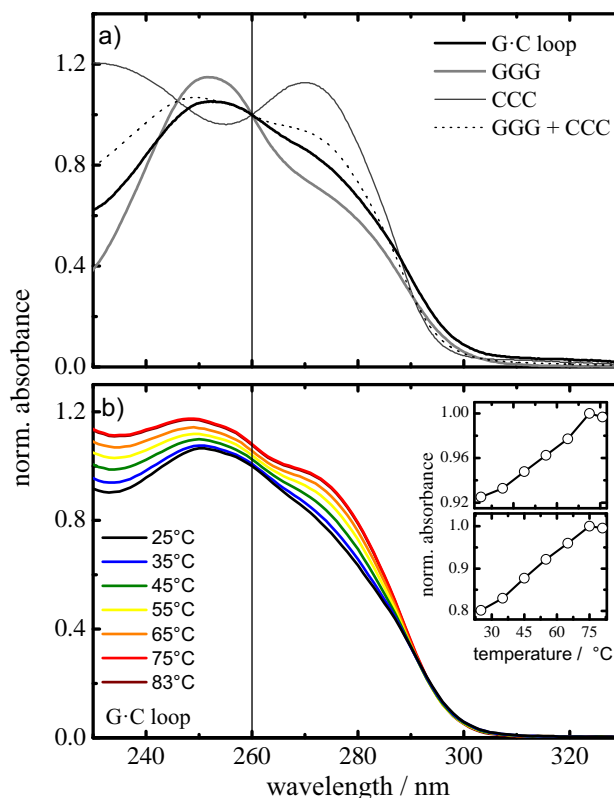


Fig. 11.3: a) Static UV absorption spectra of the self-complementary G·C loop (solid black line) and the underlying G (solid gray line) and C (thin gray line) single-stranded trinucleotides at room temperature. The sum of the two latter is indicated by the dotted line. All displayed spectra were normalized at $\lambda = 260$ nm. b) Temperature-dependent UV absorption spectra of the self-complementary G·C loop. Low-temperature measurements are indicated by blue color, higher temperature spectra are given in red. The upper inset gives the corresponding melting curve at $\lambda = 260$ nm, the lower inset the same at $\lambda = 280$ nm.

The circular dichroism (CD) spectrum of the G·C loop is displayed in Fig. 11.4. It is compared to the spectrum of the d(G)₁₀-d(C)₁₀ duplex [13]. Both spectra are practically

identical and it can be concluded that both compounds display the same secondary double helical DNA structure. The CD band, centered at $\lambda_{CD} = 260$ nm, is typical for strong G base-stacking interactions.

In parallel, the structure and stability of the loop has been determined by F. Sönnichsen (Otto-Diels Institute of Organic Chemistry at Kiel University) in multi-dimensional NMR experiments. Those studies confirmed the self-complexation via WC base pairs and ruled out the formation of G·G hydrogen bonds, which are formed by runs of G in the DNA quadruplex structure. Moreover, the NMR data revealed that the loop was relatively flexible and only the middle G·C pair was fully bonded, while the two outer

pairs showed some fraying, especially at the loop terminal. To our knowledge, this is the first time that structure-sensitive 1D and 2D NMR methods have been combined with femtosecond spectroscopy to unravel the photodynamics and -stability of DNA.

The fluorescence decay profile of the G·C loop is given in Fig. 11.5a together with the $d(G)_{10}\cdot d(C)_{10}$ duplex measured previously [13]. The decay profiles are virtually identical and the fluorescence decay time constants for the loop, derived from a nonlinear data analysis, were $\tau_{1,loop} = 0.50(15)$ ps (83(11)%) and $\tau_{2,loop} = 5(2)$ ps (17(7)%) with 2σ standard deviation in parenthesis.

The fluorescence decay curve of the constituent G trinucleotide is shown in the lower panel of Fig. 11.5. It is closely related to the fluorescence decay of the single-stranded $d(G)_{10}$ decamer [13], which is its structural analogue of higher length. The latter exhibits a slightly longer-lived profile. This is mainly due to different fractional amplitudes and otherwise, the fluorescence decay constants of both compounds match fairly well. We determined $\tau_{1,trimer} = 0.93(20)$ ps (83(7)%) and $\tau_{2,trimer} = 10(4)$ ps (17(6)%). It might be argued that the long-lived component is related to the G-stacking architecture, which clearly is more abundant in the longer decamer and thus results in a higher amplitude of the long-lived component τ_2 .

The time profiles for the G·C loop and the G trinucleotide are compared in Fig. 11.5c. Additionally, the fluorescence decay curve of the free G monophosphate (dGMP) is displayed for reference. In accordance with the literature [20], it exhibits a monoexponential decay behavior with $\tau_{dGMP} = 0.78(4)$ ps. Both, loop and trimer, have a secondary long-lived decay component, typical for nucleobase chromophores incorporated in DNA.

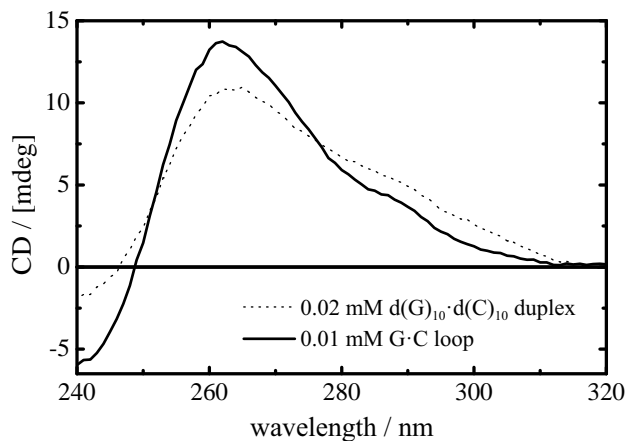


Fig. 11.4: CD spectrum of the G·C loop (solid line) in comparison to the $ud(G)_{10}\cdot d(C)_{10}$ DNA duplex (dotted line).

However, it is most eye-catching that the single-stranded G trinucleotide exhibits slower dynamics than the self-complementary loop, which manifests itself in a longer-lived primary and secondary decay component. In contrast, the self-complementary loop shows a very fast initial decay similar to that of the free dGMP. This acceleration effect on the photodynamics has to originate from the folded structure of the loop, mediated through the WC hydrogen bonds. Taking into account that, according to NMR data, only ≈ 1.5 WC base pairs do stabilize the loop, the effect of hydrogen bonding on the photodynamics of DNA via the complementary base pairing motif is significant.

Our observations oppose previous assumptions by other groups [17, 21], but confirm our conclusions of the outstanding photodynamical role of the DNA H-bonding network, which we have found to be driving force for the photodeactivation of the G-C WC base pair, either in its isolated form and probably also when it is incorporated in DNA [2, 3, 13].

The employed self-complementary oligonucleotide loop has turned out to be a powerful tool for ongoing studies, as it mimics the cooperative photodynamics of more complex DNA duplexes. Thus, it can be utilized as a template structure to investigate different short-stranded DNA sequences by femtosecond spectroscopy combined with NMR structural analysis. Moreover, is rather small in size and can be addressed by theoretical means.

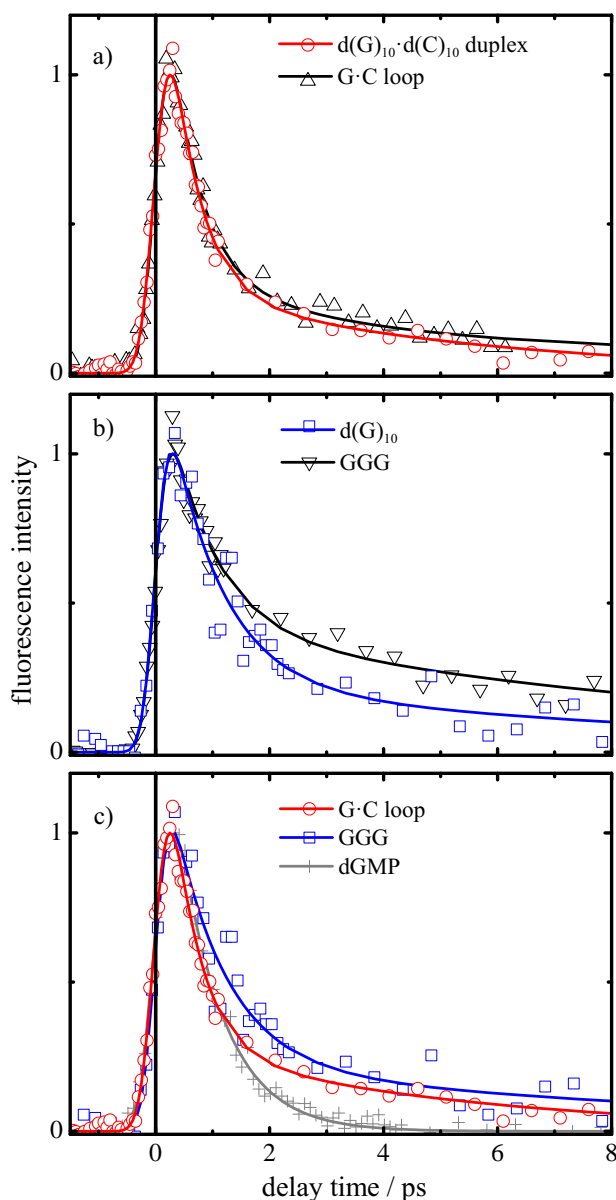


Fig. 11.5: Femtosecond fluorescence decay profile of a) the G-C self-complementary loop in comparison to the d(G)₁₀-d(C)₁₀ duplex; b) the G trinucleotide (blue, open rectangles) and the single-stranded d(G)₁₀ decamer; c) comparison of the G-C loop with the G trinucleotide and dGMP.

11.5 Discussion of Recent Theoretical Studies

High-level ab-initio calculation on nucleobase assemblies, similar to those performed on single free bases, are needed for further studies. Sustained success in the complete description of the photodynamics of DNA can only be achieved by a comprehensive experimental and theoretical interplay, as has been shown for nucleobase monomers.

Although first theoretical models [22–33] make it possible for the first time to describe the photodynamics of DNA including cooperative effects, they still suffer from crucial approximations. Foremost, the electronic coupling between the nearby bases is modeled by the (point or extended) dipole approximation, but multipole interactions were neglected, which is unsuitable if the distance between the chromophores is of the order of the length scale of one nucleobase. Additionally, calculations have been performed nearly exclusively in the gas phase, but the dielectric environment induced by a solvent cavity is expected to affect the electrostatic coupling interactions. Closely related is the neglect of dynamic disorder. Nucleobase chromophores incorporated in DNA experience a non-symmetric environment, because DNA is prone to show local fluctuations at least in short sub-segments and the flexibility can be considered to be more pronounced at the ends of each duplex. This might lead to a strong mismatch and subsequent flip-out of nucleobases. In consequence, this gives rise to a gradient energy splitting of the excitonic eigenstates. Attempts have been made to include this problem by molecular dynamics simulations, in which snapshots of the DNA geometry were obtained and have been subsequently subjected to quantum chemical calculations in order to obtain an average electronic coupling [26, 32]. It was found that the structural fluctuations of DNA, which can be considered to localize certain sub-segments of DNA, reduce the amount of delocalization [28, 31, 32]. Moreover, it is necessary to mention that often just one of the two optically bright states of the underlying nucleobases was addressed in the calculation given above, although DNA nucleobases exhibit at least two close-lying, bright $\pi\pi^*$ states and one dark $n\pi^*$ state. Nevertheless, two studies confirmed that the $n\pi^*$ transitions do not participate in electronic coupling [31] and, moreover, were found to be negligible in DNA multimers for energetic reasons [28].

Because of the complexity of DNA fragments (i.e., high number of atoms), theoretical calculations have so far been carried out mostly with the TDDFT method [28–30, 33, 34]. A major drawback of this method is its shortcoming in calculating charge-separated Rydberg or CT states. It fails to describe the asymptotic behavior of the potential for long-range dispersion interaction. This mainly results in an overestimation of the stability of those states [35, 36]. Suitable (non-empirical) functionals need to be applied and can be combined with additional long-range correction terms that do perform correctly in the asymptotic limit [28–30, 33, 34]. These combined methods can be considered as a local (TD)DFT description, in which the long-range Coulomb interaction is switched on by a suitable function (i.e., error function) that increases non-local Hartree-Fock exchange

needed for CT states [33, 34]. Although the relative ordering of the optically dark $\pi\pi^*$ CT states with respect to the optically bright $\pi\pi^*$ states is sensitive to the applied functional and even more to the solvation shell that has been introduced in these calculations, the outcome can be summarized as follows: CT states, either concerned to intrastrand CT via stacked nucleobases, interstrand CT originating from hydrogen bonding or cross-coupled interstrand CT states of nearby nucleobases on opposite strands, can be located within or around the spectroscopically bright $\pi\pi^*$ transitions, which can lead to pronounced internal conversion processes. After photo-excitation, the bright delocalized FC regions of the exciton states might evolve into rather localized states on the PEHS, from which monomer-like deactivation seems to compete significantly with the decay to the most localized exciplex and CT states. Theory predicts that the latter are reachable ultrafast without substantial rearrangements of the stacked geometry and are irreversibly populated [28]. Other (still unknown) radiationless processes account for the deactivation of those states. Finally, it has to be noted that none of the theoretical studies of electronic coupling in the DNA included nuclear degrees of freedom, required for internal conversion processes (CIs). Thus, a real dynamic picture similar to that introduced for nucleobase monomers still remains a task for the future. Only two months ago, this field has been accessed and first calculations on the electronic relaxation pathways of homodimers of A with different degrees of stacking interaction have been performed at the CASPT2 level of theory [37]. The results suggested that the main deactivation channel in monomeric A, i.e., the CI mediating between the optically prepared $\pi\pi^*$ state and S_0 , is accessible in the stacked dimers as well. An energy barrier en route has to be surmounted, which leads to a slowdown of the excited-state dynamics. The height of the barrier depends on the stability of the dimer, i.e., the strength of the stacking interaction.

References and Notes

- [1] C. E. Crespo-Hernández, B. Cohen, P. M. Hare, B. Kohler, *Chem. Rev.* **104**, 1977 (2004).
- [2] N. K. Schwalb, F. Temps, *J. Am. Chem. Soc.* **129**, 9272 (2007).
- [3] N. K. Schwalb, F. Temps, *J. Phys. Chem. A*, *submitted* (2009).
- [4] A. L. Sobolewski, W. Domcke, C. Hättig, *Proc. Nat. Acad. Sci. USA* **102**, 17903 (2005).
- [5] P. R. L. Markwick, N. L. Doltsinis, *J. Chem. Phys.* **126**, 175102 (2007).
- [6] G. Groenhof *et al.*, *J. Am. Chem. Soc.* **129**, 6812 (2007).
- [7] N. K. Schwalb, F. Temps, *unpublished results* (2009).
- [8] N. K. Schwalb, F. Temps, *Angew. Chem.*, *submitted* (2009).
- [9] N. K. Schwalb, F. Temps, *J. Photochem. Photobiol. A*, *submitted* (2009).
- [10] C. E. Crespo-Hernández, B. Cohen, B. Kohler, *Nature* **436**, 1141 (2005).
- [11] D. Onidas, T. Gustavsson, E. Lazzarotto, D. Markovitsi, *J. Phys. Chem. B* **111**, 9644 (2007).
- [12] D. Onidas, T. Gustavsson, E. Lazzarotto, D. Markovitsi, *Phys. Chem. Chem. Phys.* **9**, 5143 (2007).
- [13] N. K. Schwalb, F. Temps, *Science* **322**, 243 (2008).
- [14] J. Kleber, Statische absorptions- und fluoreszenzspektroskopische untersuchungen von kooperativen effekten zwischen dna-chromophoren im einzelstrang, Master's thesis, Christian-Albrechts-University (2009).
- [15] C. E. Crespo-Hernández, K. de La Harpe, B. Kohler, *J. Am. Chem. Soc.* **130**, 10844 (2008).
- [16] T. Takaya, C. Su, K. de La Harpe, C. E. Crespo-Hernández, B. Kohler, *Proc. Nat. Acad. Sci. USA* **105**, 10285 (2008).
- [17] C. E. Crespo-Hernández, B. Cohen, B. Kohler, *Nature* **441**, E8 (2006).
- [18] J. Tuma, S. Tonzani, G. C. Schatz, A. H. Karaba, F. D. Lewis, *J. Phys. Chem. B* **111**, 13101 (2007).
- [19] N. K. Schwalb, J. Kleber, F. Sönnichsen, F. Temps, *Phys. Chem. Chem. Phys.*, *manuscript in preparation* (2009).
- [20] C. E. Crespo-Hernández, B. Cohen, P. M. Hare, B. Kohler, *Chem. Rev.* **104**, 1977 (2004).
- [21] D. Markovitsi *et al.*, *Nature* **441**, E7 (2006).
- [22] B. Bouvier, T. Gustavsson, D. Markovitsi, P. Millié, *Chem. Phys.* **275**, 75 (2002).
- [23] B. Bouvier *et al.*, *J. Phys. Chem. B* **107**, 13512 (2003).
- [24] E. Emanuele, D. Markovitsi, P. Millié, K. Zakrewska, *Chem. Phys. Chem.* **6**, 1387 (2005).
- [25] E. R. Bittner, *J. Chem. Phys.* **125**, 094909 (2006).
- [26] A. Czader, E. R. Bittner, *J. Chem. Phys.* **128**, 035101 (2008).

- [27] H.-H. Ritze, P. Hobza, D. Nachtigallová, *Phys. Chem. Chem. Phys.* **9**, 1672 (2007).
- [28] F. Santoro, V. V. Barone, R. Improta, *Proc. Nat. Acad. Sci. USA* **104**, 9931 (2007).
- [29] F. Santoro, V. Barone, R. Improta, *Chem. Phys. Chem.* **9**, 2531 (2008).
- [30] R. Improta, *Phys. Chem. Chem. Phys.* **10**, 2656 (2008).
- [31] D. Nachtigallová, P. Hobza, H. H. Ritze, *Phys. Chem. Chem. Phys.* **10**, 5689 (2008).
- [32] S. Tonzani, G. C. Schatz, *J. Am. Chem. Soc.* **130**, 7607 (2008).
- [33] A. W. Lange, J. M. Herbert, *J. Am. Chem. Soc.* **131**, 3913 (2009).
- [34] A. W. Lange, M. A. Rohrdanz, J. M. Herbert, *J. Phys. Chem. B* **112**, 6304 (2008).
- [35] A. Dreuw, J. L. Weisman, M. J. Head-Gordon, *J. Chem. Phys.* **119**, 2943 (2003).
- [36] A. Dreuw, M. Head-Gordon, *J. Am. Chem. Soc.* **126**, 4007 (2004).
- [37] G. Olasso-González, M. Merchán, L. Serrano-Andrés, *J. Am. Chem. Soc.* **131**, 4368 (2009).

Appendix

A DNA Monophosphates

A.1 Fluorescence Decay Profiles

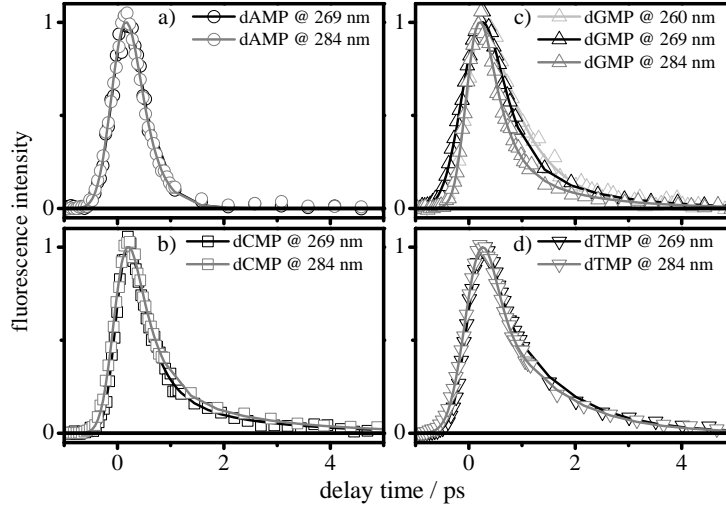


Fig. A.1: Fluorescence decay profiles of all DNA monophosphates measured at $\lambda_{pump} = 260, 269$ and 284 nm in buffered solution. a) dAMP: monoexponential decay with $\tau_{dAMP} = 0.30(1)$ ps; b) dCMP: monoexponential fitting ($\tau_{dCMP} = 0.62(1)$ ps) was not fully sufficient, but biexponential fitting provided $\tau_{dCMP,1} = 0.39(2)$ ps (84%) and $\tau_{dCMP,2} = 1.9(2)$ ps; c) dGMP: at $\lambda_{pump} = 260$ nm a monoexponential fit gave $\tau_{dGMP,260} = 0.78(2)$ ps, all other profiles could not be described satisfactorily by a monoexponential fit. Biexponential fitting resulted in $\tau_{dGMP,1} = 0.34(4)$ ps (82%) and $\tau_{dGMP,2} = 1.4(2)$ ps; d) TMP: monoexponential fitting ($\tau_{TMP} = 0.78(2)$ ps) did not suit fully to the observed profiles and, hence, the fluorescence decay was best described with $\tau_{dTMP,1} \ll 0.1$ ps and $\tau_{dTMP,2} = 1.13(3)$ ps. All data resemble literature values [1].

A.2 CD Spectra

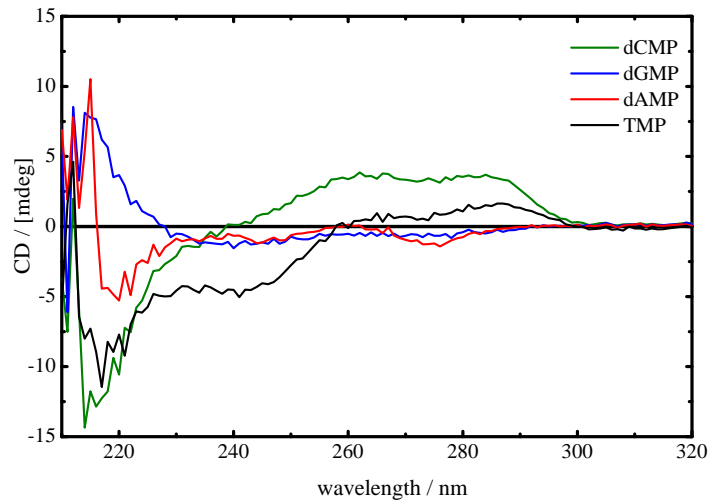


Fig. A.2: CD spectra of all DNA monophosphates. All data resemble literature values [2–4].

B Band Analysis of the FTIR Spectra of G, C and G...C

In the global fit analysis, vibrational bands of the monomer and the dimer were coupled through K_i/β_i ($i = G \cdots G, C \cdots C$ and $G \cdots C$) given by the respective association equilibria (see *Chapter 3*). In the following graphs, ϵ_{eff} (calculated from the initial concentration c_0) is plotted vs. the wavenumber in cm^{-1} . Gray open symbols indicate data points, solid lines denote the fit results. The dimer spectrum is colored in red and the monomer spectrum is given in blue. The dark green curve presents a broad background term, which results from the tail of the strong absorption bands of the TBDMS groups well below the fitting window and from the H-bonded network around $\approx 3200 - 3150 \text{ cm}^{-1}$. The sum of all individual spectra is given in black.

B.1 Gaussian Band Analysis of the FTIR Spectra of C

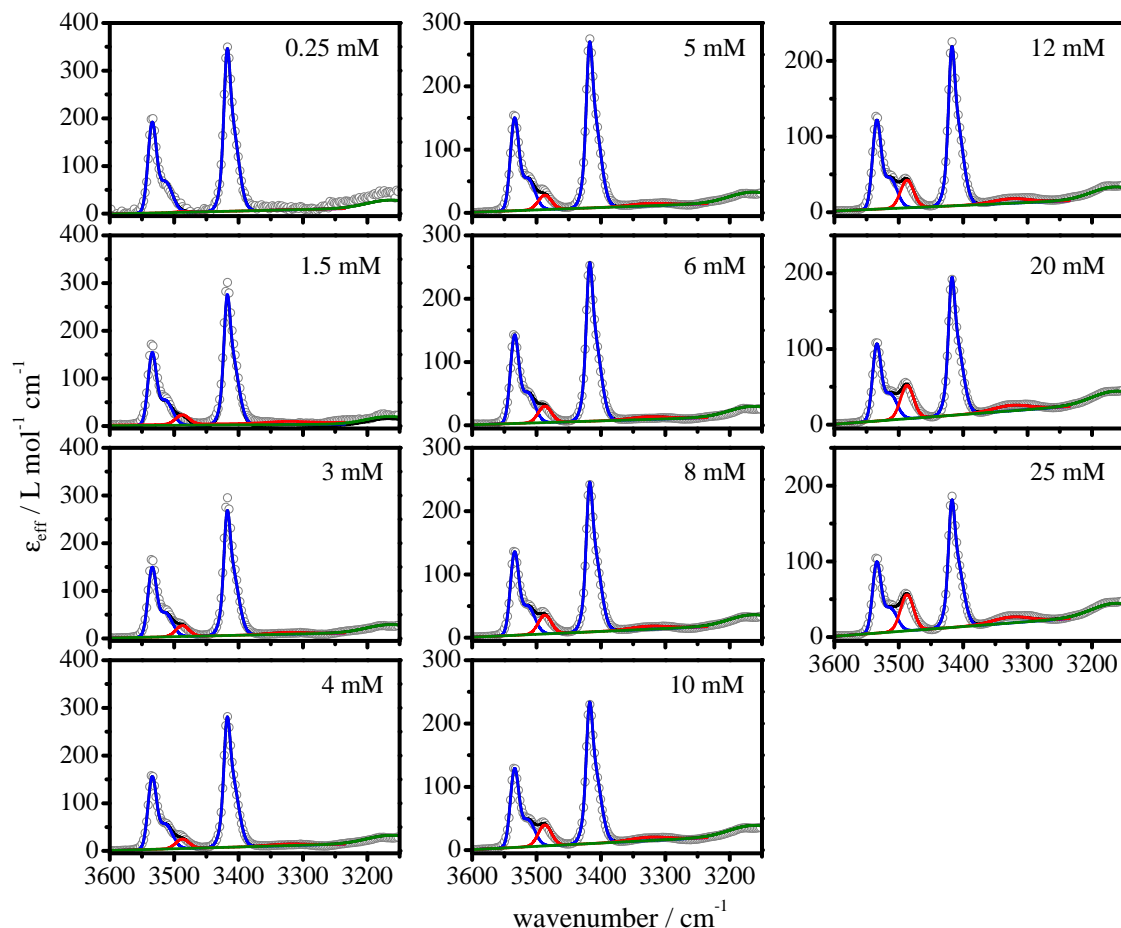


Fig. B.1: Global Gaussian band analysis of C. The globally determined value for the self-association constant of C was $K_{C \cdots C} = (42.8 \pm 2.1) \text{ M}^{-1}$ [5, 6].

B.2 Gaussian Band Analysis of the FTIR Spectra of G

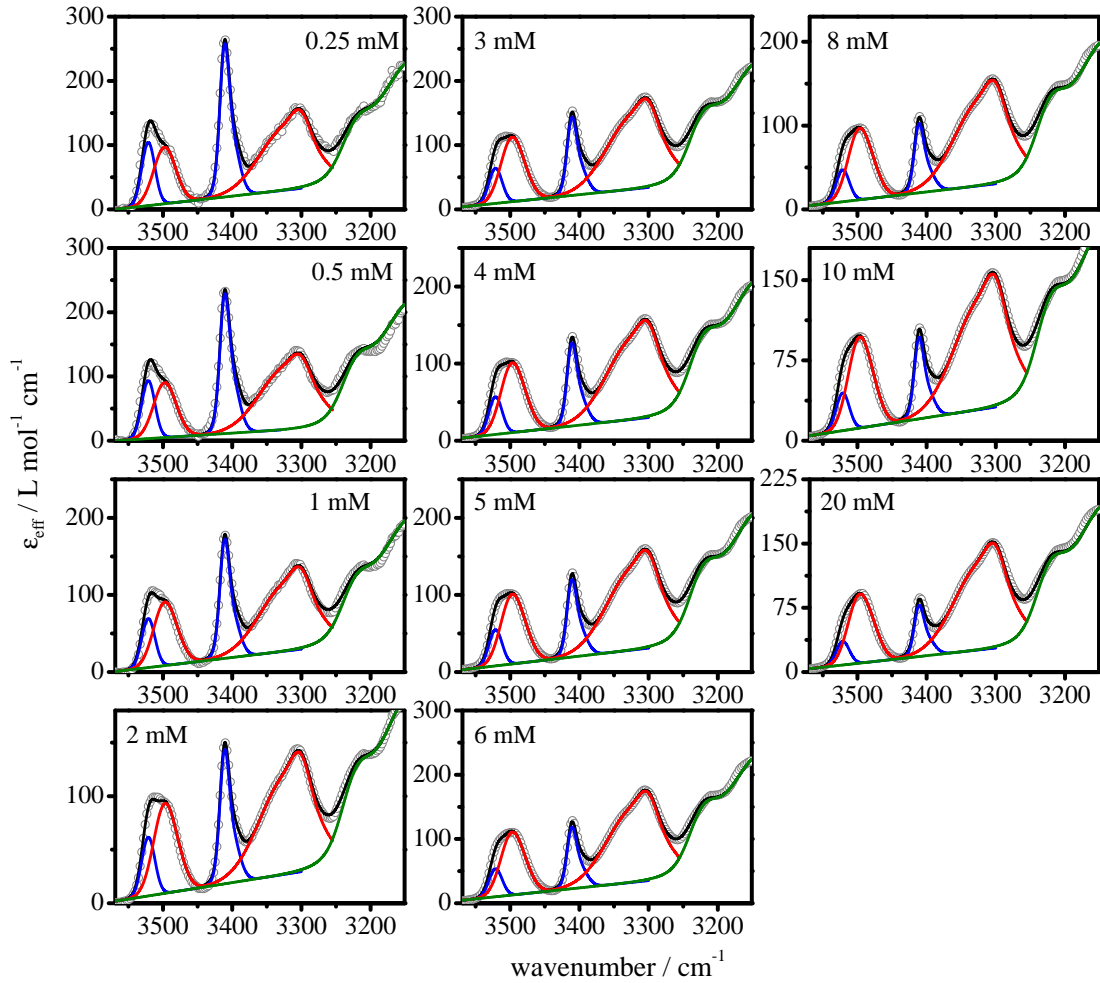


Fig. B.2: Global Gaussian band analysis of G. G displays a strong and highly structured vibrational band of the H-bond, which points to strong anharmonic couplings of the H-bonded $\text{NH}\cdots\text{O}$ and $\text{NH}\cdots\text{N}$ stretching vibrations. As the $\text{G}\cdots\text{G}$ dimer structure is asymmetric [7], the spectral bands of the dimer consist of two Gaussians indicating the partially and fully free NH_2 and NH stretches. However, in dependence on how many bands and spectra were coupled, the globally determined values for the self-association constant of G varied between $K_{\text{G}\cdots\text{G}} = (557 \pm 94)$ to $(1013 \pm 370) \text{ M}^{-1}$ [6, 7]. Due to error propagation, the maximum relative error for the degree of $\text{G}\cdots\text{G}$ self-association of $\beta_{\text{G}\cdots\text{G}}$ is less than 3%.

B.3 Gaussian Band Analysis of the FTIR Spectra of G...C

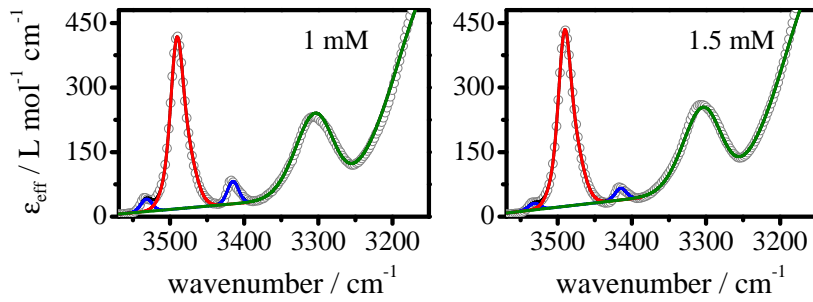


Fig. B.3: Global Gaussian band analysis for G...C. The degree of association $\beta_{G...C}$ is too strong for a sufficient fitting of the ϵ -spectra of G...C, which were calculated from the absorption spectra due to Lambert-Beer's law and thus strongly depend on ΔA , Δc_0 and Δl . Only the spectra measured at $c_0 = 1.0$ and 1.5 mM could be subjected to a global fit analysis. Here, the two residual monomer bands at ≈ 3531 and 3415 cm^{-1} were coupled with the dimer band at 3490 cm^{-1} . This band is made up by two Gaussians, representing both free NH_2 stretching vibrations of the dimer. The globally determined value for the G...C association constant was $K_{G...C} = (33.9 \pm 7.5) \cdot 10^3 \text{ M}^{-1}$ [6, 7].

B.4 Single Band Analysis of the FTIR Spectra of G, C and G...C

At an early stage of this *Thesis*, the association constants K_i have been determined from a single band analysis, following the protocol of Carmona *et al.* [8]. All observed monomer and dimer bands have been subjected to this analysis. Exemplarily, three results are displayed in the following. All obtained values resembled the literature data [8].

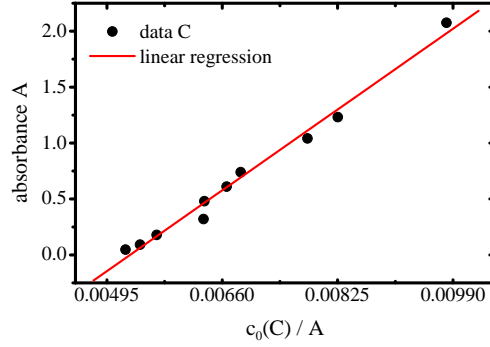


Fig. B.4: Determination of $K_{C...C}$ from the monomer band at 3411 cm^{-1} . Plotted is the concentration-dependent absorbance A of the vibrational band vs. the ratio of initial concentration and respective absorbance. The obtained value for the C...C association constant was $K_{C...C} = (41 \pm 3)\text{ M}^{-1}$.

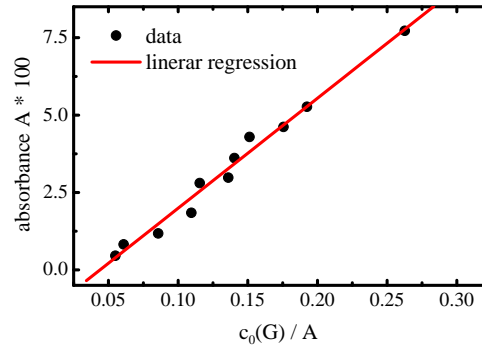


Fig. B.5: $K_{G...G}$ was determined from the monomer band at 3521 cm^{-1} . Plotted is the concentration-dependent absorbance A of the vibrational band vs. the ratio of initial concentration and respective absorbance. The obtained value for the G...G association constant was $K_{G...G} = (728 \pm 182)\text{ M}^{-1}$, which fairly well matches the literature data [8].

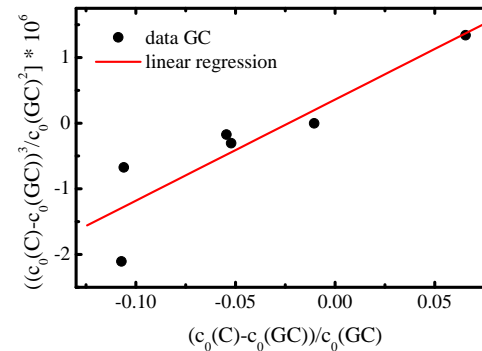


Fig. B.6: Following the protocol of Carmona *et al.* [8], $K_{G...C}$ was determined from a single band analysis. Considering the dimer band at 3488 cm^{-1} with regard to the very weak and practically negligible residual monomer bands and a proper adjustment of $\epsilon_{G...C}$ [8], the obtained value for the G...G association constant was $K_{G...G} = (64.9 \pm 1.6 \cdot 10^3)\text{ M}^{-1}$.

B.5 CD Spectra of G, C and G...C

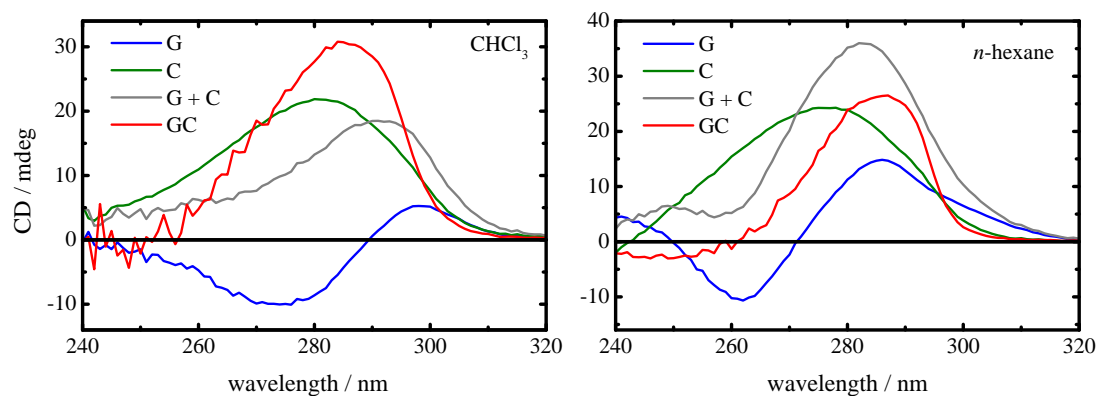


Fig. B.7: CD spectra of G (blue), C (green), their sum G+C (gray) and G...C (red). Left: in CHCl₃; Right: in *n*-hexane. A solvent-dependent spectral difference, which is most pronounced for the G-containing sample spectra, is observed. It can be concluded that different hydrogen bonded complexes are formed in the respective solvents. Note that the spectra of the H-bonded species do not display a CD band at $\lambda = 260$ nm, typical for G base stacks.

C Hydrogen-Bonding Dynamics in A···T and 2AP···T Base Pairs

C.1 Introduction

In analogy to the experiments performed on the G···C base pair (see *Chapters 4* and *5*, [6, 9]), we have carried out similar experiments on the adenosine-thymidin (A···T) and 2-aminopurine-thymidin (2AP···T) base pairs. At least for the A···T Watson-Crick (WC) base pair, the same intermolecular reversible purine-to-pyrimidine electron-induced proton-transfer mechanism has been postulated [10]. 2AP is commonly utilized as an intrinsic fluorophore for studying local conformational changes within the DNA and environmental and solvation dynamics. However, in these studies, the effect of hydrogen-bonding dynamics of the 2AP···T pair incorporated in DNA have been neglected and the observed photo-effects have only been attributed to π -stacking interactions of 2AP with its neighboring nucleobases. An additional feature of 2AP is its red-shifted absorption, which allows for a selective excitation of 2AP in a mixture of nucleobases, especially next to T.

The preliminary results of the measured static and transient spectra on A, 2AP and T as well as on the respective base pairs A···T and 2AP···T are listed in the following. The experimental setup and details, including sample preparation and handling equaled those described earlier (see *Chapters 5*, *6*, *7* and *8*). The synthesis of the A(TBDMS)₃ and T(TBDMS)₂ samples was carried out by H.-M. Behrends as a student research assistant. The 2AP(TBDMS)₂ sample was synthesized by H. Neumann and T. Michalak, who additionally performed all FTIR measurements during an advanced research internship.

In the displayed FTIR spectra, ϵ_{eff} (calculated from c_0) is plotted vs. the wavenumber in cm^{-1} . The color coding is as follows: Gray open symbols indicate data points, solid lines denote the fit results. The obtained dimer spectra are colored in red and the monomer spectra are given in blue. The green curve in each spectrum represents a broad background term, which results from the H-bond network around $\leq 3320 \text{ cm}^{-1}$ and the tail of a strong absorption band of CHCl_3 or *n*-hexane well below the fitting window. The sum of all individual spectra is assigned in black. The UV spectra are given in Fig. C.1.

C.1.1 UV spectra

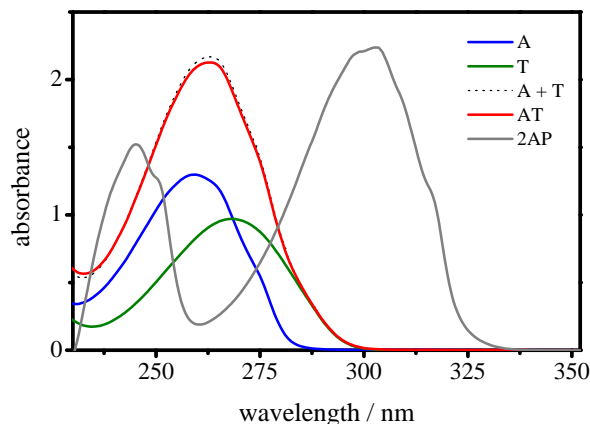


Fig. C.1: UV absorption spectra of A, T, A···T ($c_0 = 1.0 \text{ mM}$) and 2AP ($c_0 = 3.0 \text{ mM}$) in CHCl_3 .

C.1.2 Gaussian Band Analysis of the FTIR Spectra

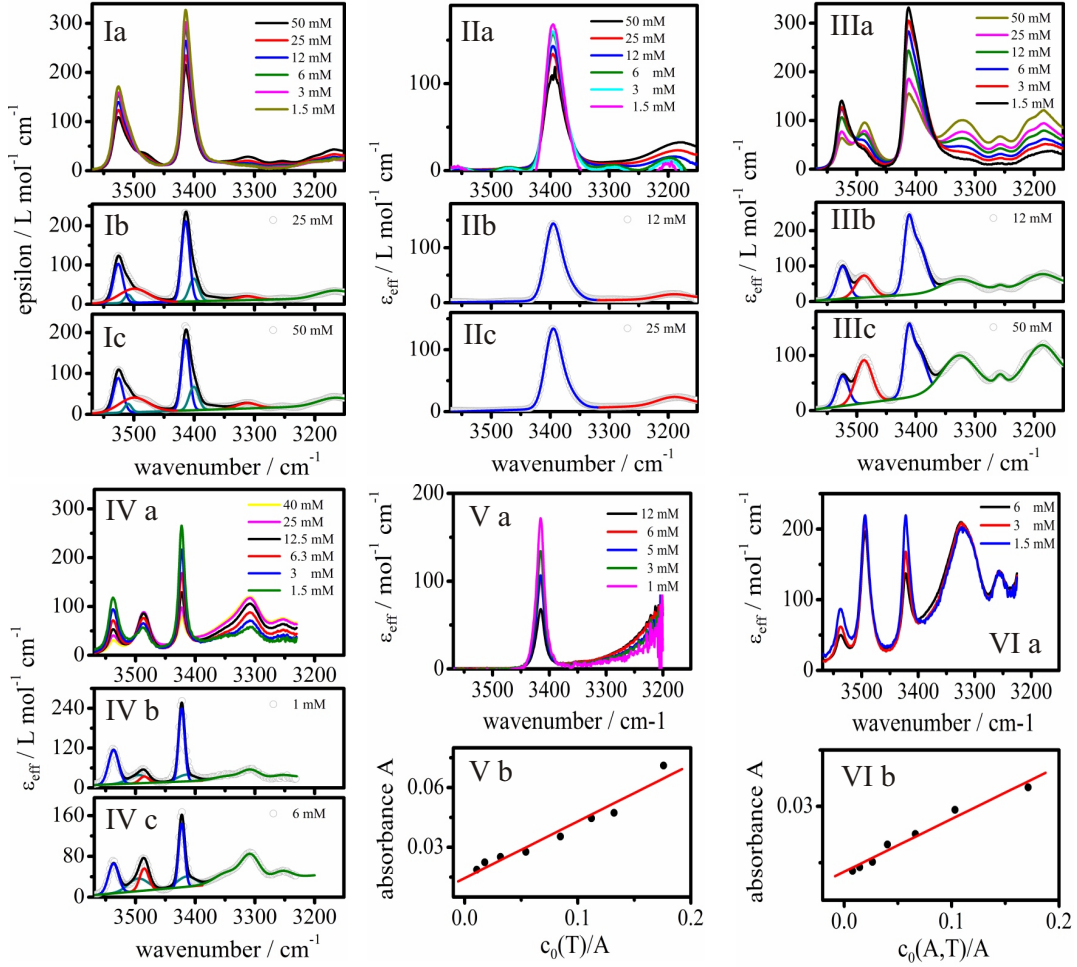


Fig. C.2: Global Gaussian band analysis of the FTIR spectra of A, T and A...T in CHCl_3 (I-III) and n -hexane (IV - VI).

Figs. Ia - VIa give an overview over the respective FTIR spectra. Figs. Ib,c - VIb,c display selected spectra and their global fit results. Note that hints were found in the FTIR spectra of A, which point to the existence of more than one tautomer present in the investigated concentration range, which was suggested by others as well [11]. Further experimental data and DFT(TPSS) calculations similar to those performed on the G and C containing base pairs [5, 7, 12] are needed for a full understanding.

(I) A in CHCl_3 : In accordance with the literature, spectral band fitting requires the existence of a second monomer (dark cyan curve) aside from the most stable canonical monomer (blue curve) [11], but only a single A...A dimer is formed. The globally determined value for the self-association constant of the homo-dimer was $K_{A...A} = (12.4 \pm 0.7) \text{ M}^{-1}$. **(II)** T in CHCl_3 : The globally determined value for the self-association constant was $K_{T...T} = (6.7 \pm 1.0) \text{ M}^{-1}$. **(III)** A...T in CHCl_3 : The globally determined value for the association constant was $K_{A...T} = (107.0 \pm 3.9) \text{ M}^{-1}$. **(IV)** A in n -hexane: Like the spectra in CHCl_3 , a second monomer (dark cyan curve) exists aside from the most stable canonical monomer (blue curve), which is not participating in the association equilibrium. The globally determined value for the self-association constant was $K_{A...A} = (233.5 \pm 68.2) \text{ M}^{-1}$. **(V)** T in n -hexane: As the band of the H-bonded network is hidden by the strong absorption of n -hexane, a single band analysis following the protocol of Carmona *et al.* [8] was carried out. The value for the self-association constant was $K_{T...T} = (1354 \pm 577) \text{ M}^{-1}$. **(VI)** A...T in n -hexane: Only the band at 3422 cm^{-1} could be evaluated in a single band analysis and gave an association constant of $K_{A...T} = (888.0 \pm 194.9) \text{ M}^{-1}$.

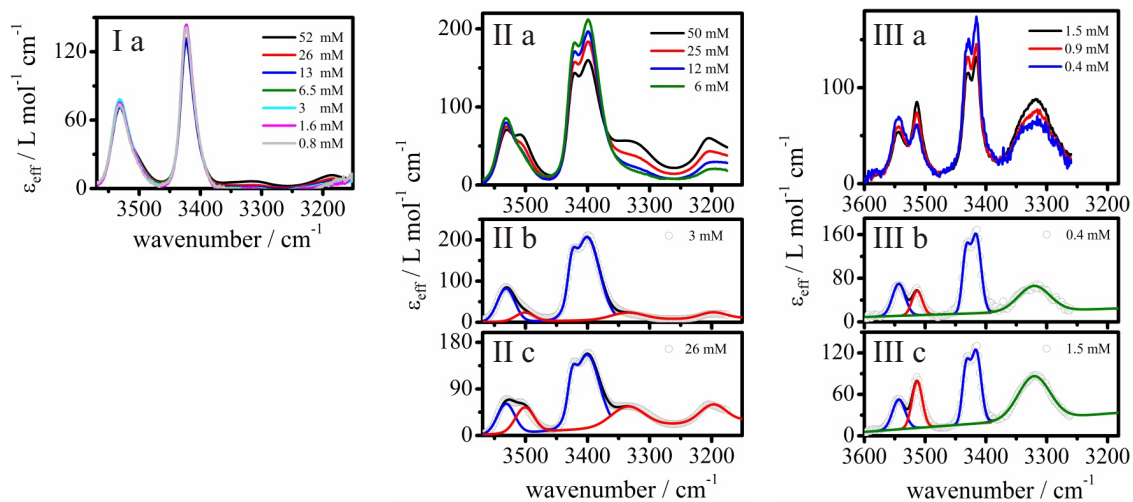


Fig. C.3: FTIR spectra and Gaussian band analysis of 2AP in CHCl₃ (Ia) and the 2AP...T base pair in CHCl₃ (IIa-c) and *n*-hexane (IIIa-c).

Figs. Ia - IIIa give an overview over the respective FTIR spectra. Figs. Ib,c - IIIb,c display selected spectra and their global fit results.

Ia: no self-association of 2AP was observable in the investigated concentration range. **IIa-b:** 2AP...T in CHCl₃: The globally determined value for the association constant was $K_{2AP...T} = (59.8 \pm 16.7) \text{ M}^{-1}$. **IIIa-b:** 2AP...T in *n*-hexane: The globally determined value for the association constant was $K_{2AP...T} = (1723 \pm 331) \text{ M}^{-1}$.

C.1.3 Fluorescence Decay Profiles

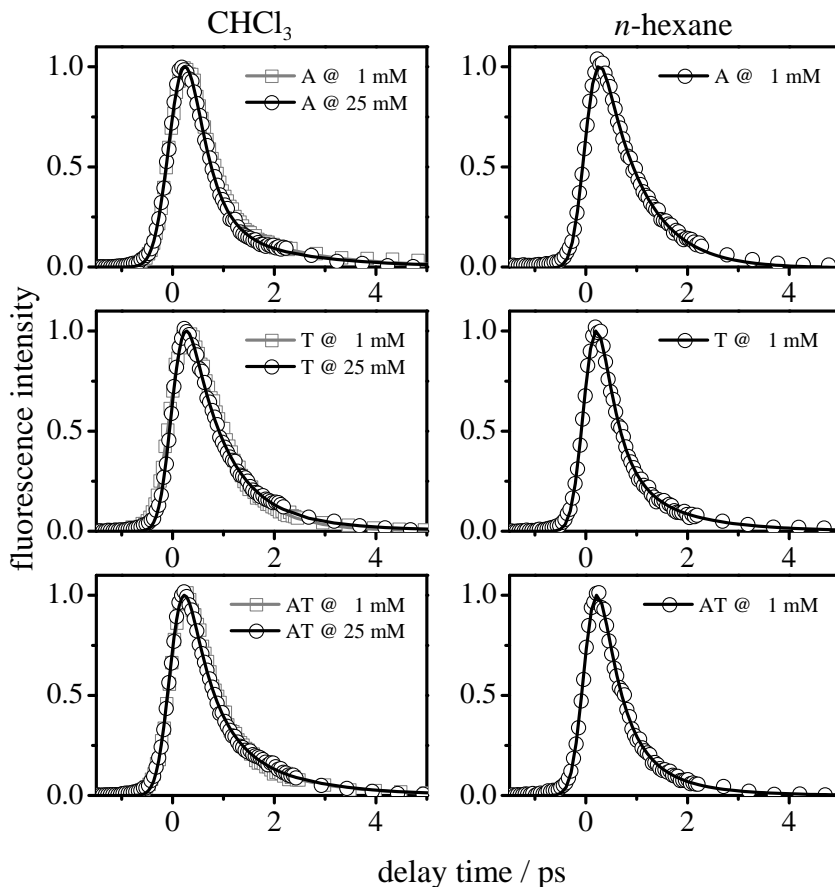


Fig. C.4: Fluorescence decay profiles of A, T and an equimolar A/T mixture in CHCl_3 (left) and n -hexane (right). No significant differences between the biexponential decay curves were obtained. The respective two time constants in CHCl_3 were of the order of several hundred femtoseconds ($\tau_A = 0.36(2)$ ps; $\tau_T = 0.69(5)$ ps; $\tau_{A\dots T} = 0.47(5)$ ps) and a few picoseconds ($\tau_{A,T,A\dots T} \approx 1.6(6)$ ps; 10 – 22%). This slightly changed to $\tau_A = 0.78(1)$ ps, $\tau_T = 0.34(10)$ ps and $\tau_{A\dots T} = 0.40(2)$ ps in n -hexane, where only T and $A\dots T$ share a picosecond component of $\tau_{T,A\dots T} = 1.1(3)$ ps (20%).

The sub-picosecond decay components determined for A and T closely resemble values found for both compounds in aqueous solution. The slower components (τ_2) are reminiscent of the dynamics in the gas phase [13] and attributed correspondingly to stepwise deactivation via the $n\pi^*$ states, which may take place in an aprotic solvent like CHCl_3 as it does in the gas phase, but not in H_2O .

Interestingly, the results for the $A\dots T$ base pair were virtually identical to those for the free nucleoside. Thus, there was no strong and unambiguous effect of the base pairing as was obtained for the $G\dots C$ WC pair [6, 9], although the same coupled electron-proton transfer deactivation mechanism was also proposed by theory [10]. The respective degrees of associations were $\beta_{A\dots T,1mM} = 8.8\%$ and $\beta_{A\dots T,25mM} = 54.8\%$ in CHCl_3 and $\beta_{A\dots T,1mM} = 36.2\%$ in n -hexane. We suggest two plausible explanations for this result: (a) Although $A\dots T$ complex formation was firmly established by FTIR, it may not be the WC complex that is formed under the described conditions. It is known that $A\dots T$ preferentially forms Hoogsteen pairs, but the electron-proton transfer mechanism is proposed to be active exclusively in the WC pair and was indeed excluded at least in non-WC forms of $G\dots C$ [14–16]. (b) If there is an effect of $A\dots T$ base pair formation on the excited state lifetime, it might be below our experimental time resolution of ≈ 200 fs.

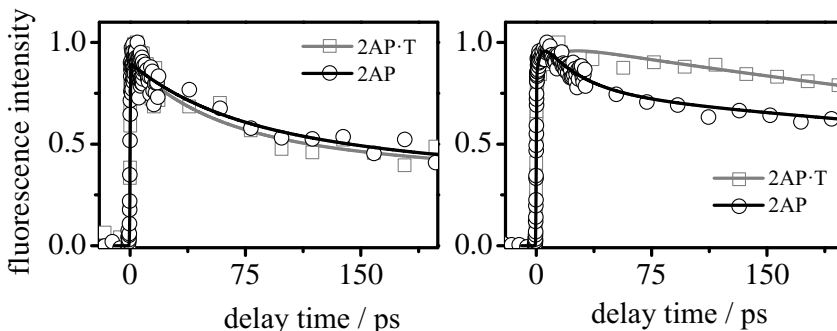


Fig. C.5: Fluorescence decay profiles of 2AP and 2AP...T in CHCl_3 at $\lambda_{fl} = 407$ nm for free 2AP and an equimolar mixture of 2AP with T (containing $(45 \pm 10)\%$ 2AP...T) after excitation at $\lambda_{pump} = 304$ nm (left) and 324 nm (right).

According to literature, the temporal fluorescence profiles of 2AP on the 1 – 150 ps time scale shown are dominated by solvation dynamics. We found different behaviors depending on the excitation wavelength: The higher excess energy in the 2AP at $\lambda_{pump} = 304$ nm gives an initial decay on the 100 ps timescale. In contrast, a slower initial rise is seen after excitation at $\lambda_{pump} = 324$ nm. The difference can be ascribed to solvation dynamics that contributes at the higher excitation energy ($\lambda_{pump} = 304$ nm). This contrasts with measurements on 2AP in H_2O , where vibrational relaxation was assumed to be insignificant [17]. For $\lambda_{pump} > 324$ nm and $\lambda_{fl} > 407$ nm the initial rise/decay of the profile is superimposed by a delayed, but rising time component, which indicates even more complex vibrational relaxation/solvation dynamics.

The mixture containing 2AP...T shows similar fluorescence profiles as free 2AP at the shorter excitation wavelength ($\lambda_{pump} = 304$), but the behavior becomes completely different for excitation near the origin ($\lambda_{pump} = 324$). Here, the initial picosecond rise is absent and a decay component on the ≈ 50 ps time scale appears instead which holds $\approx 30\%$ of the overall amplitude. We attribute this effect to 2AP...T dimer formation by H-bonding and emphasize that, although the change appears small at first glance, it is actually highly significant, since the 2AP...T fraction in the solution is $\leq 50\%$. A second set of fluorescence decay curves measured at $\lambda_{fl} = 350$ nm showed practically identical results.

C. 4 Discussion

These first results on 2AP...T hint at a competition between solvation dynamics, vibrational relaxation, and dynamics controlled by the intermolecular H-bridges of the 2AP...T base pair. The effects depend on the excitation wavelength and thus on the vibronic excess energy deposited in the 2AP molecule. Clearly, further fluorescence rise and decay experiments are needed at additional excitation and additional emission wavelengths to fully determine the solvation response function. It is also of interest to preferentially pump the T moiety at $\lambda_{pump} = 270$ nm, where 2AP shows little absorption. The present results indicate, however, that interpretations of fluorescence-time profiles of 2AP in DNA only on the basis of π -stacking interactions with neglect of 2AP...T base pairing may be too simple and that the effect of the H-bonds on the ensuing fluorescence dynamics cannot be neglected..

D Control Programs

D.1 Up-Conversion Program

D.1.1 Main Front Panel

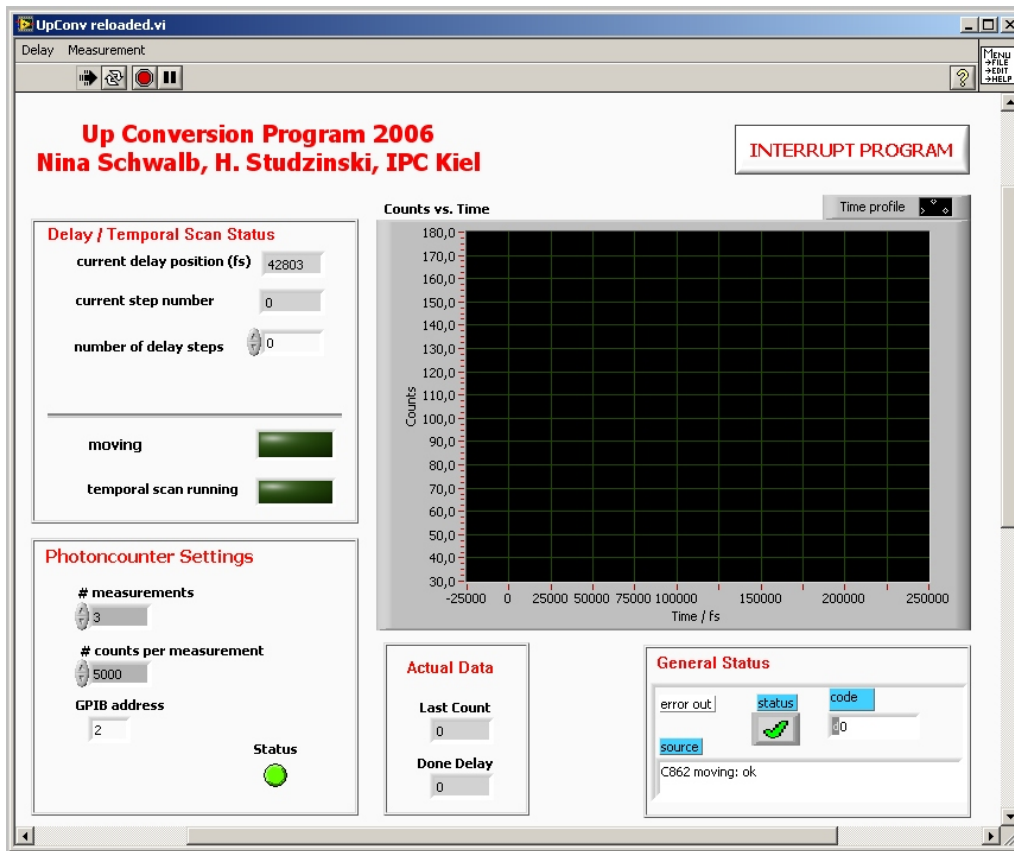


Fig. D.1: Main front panel of the up-conversion program. To start a measurement, the parameters of the photon counter, which are not directly set on the counter itself (see *Chapter 2*), can be chosen on the front panel: **# measurements** gives the number of measurements at one specific delay step that are averaged. **# counts per measurements** gives the duration of one measurement at a certain delay step (\equiv number of accumulated laser shots). The delay/temporal scan parameters on the front panel are indicators. Their value can be set in the runtime menu ‘Delay’ and ‘Measurement’.

D.1.2 Runtime Menu 'Delay'

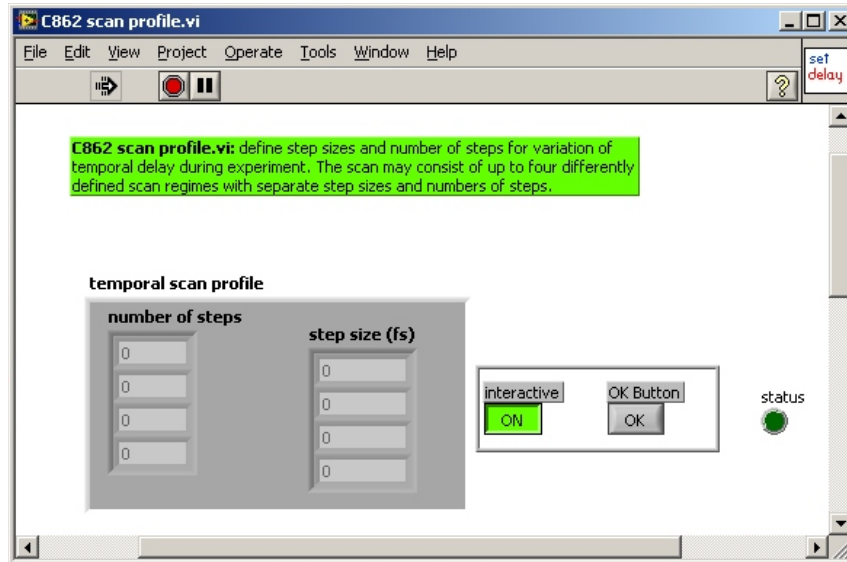
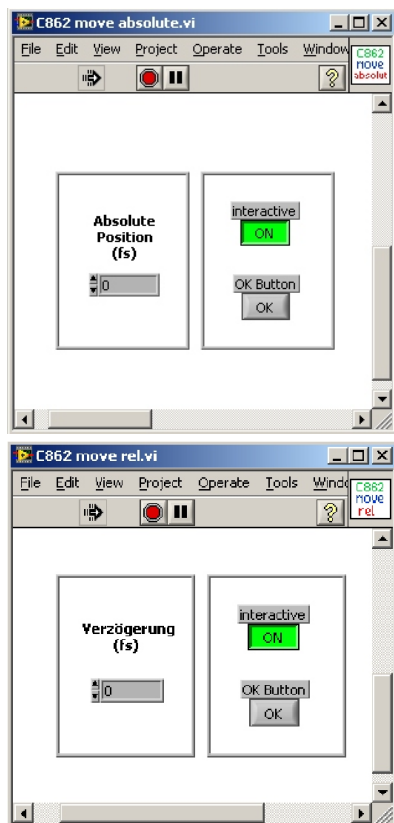


Fig. D.2: Runtime Menu 'Delay': *Set Temporal Scan Profile*: Allows to choose the number of steps and their size in femtoseconds. Up to four different delay sizes can be set.



Left Fig. D.3: Runtime Menu 'Delay': i) *Move Absolute*: allows to move the delay stage to the desired absolute delay position in femtoseconds; ii) *Move Relative*: allows to move the delay stage relative to the current position in femtoseconds.

D.1.3 Runtime Menu 'Measurement'

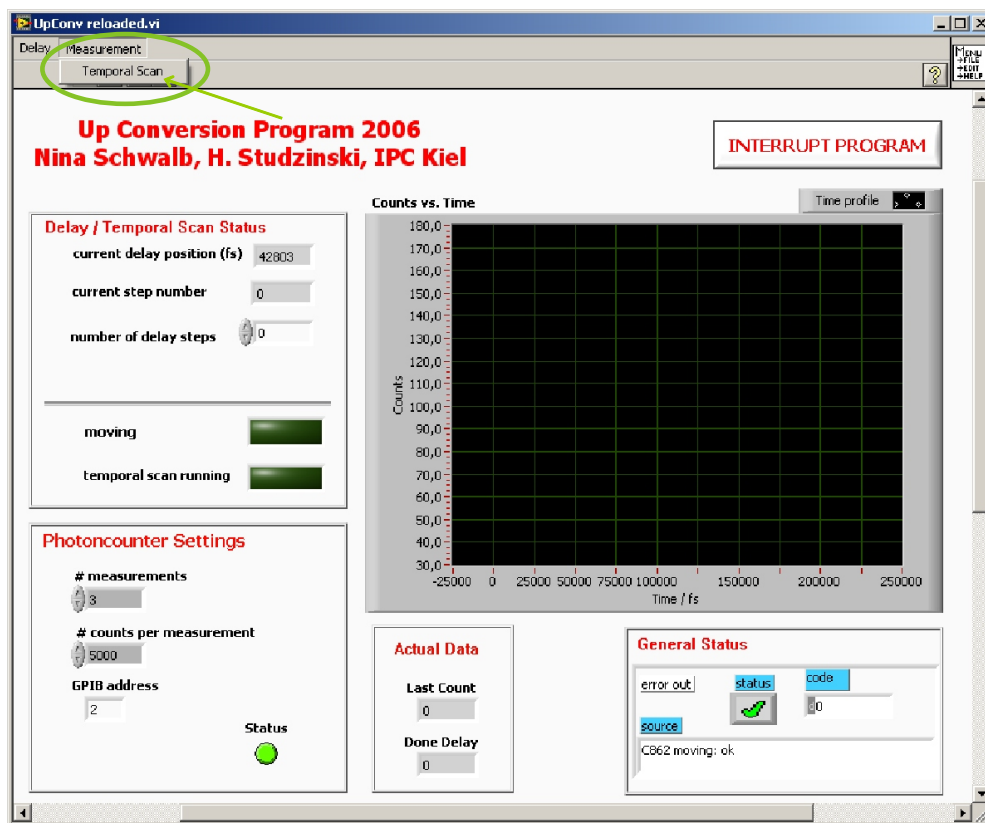


Fig. D.4: Runtime Menu 'Measurement'. The sub-menu *Temporal Scan* starts the experiment and the measured count rates are plotted vs. the respective current delay step.

D.1.4 Save Data Procedure

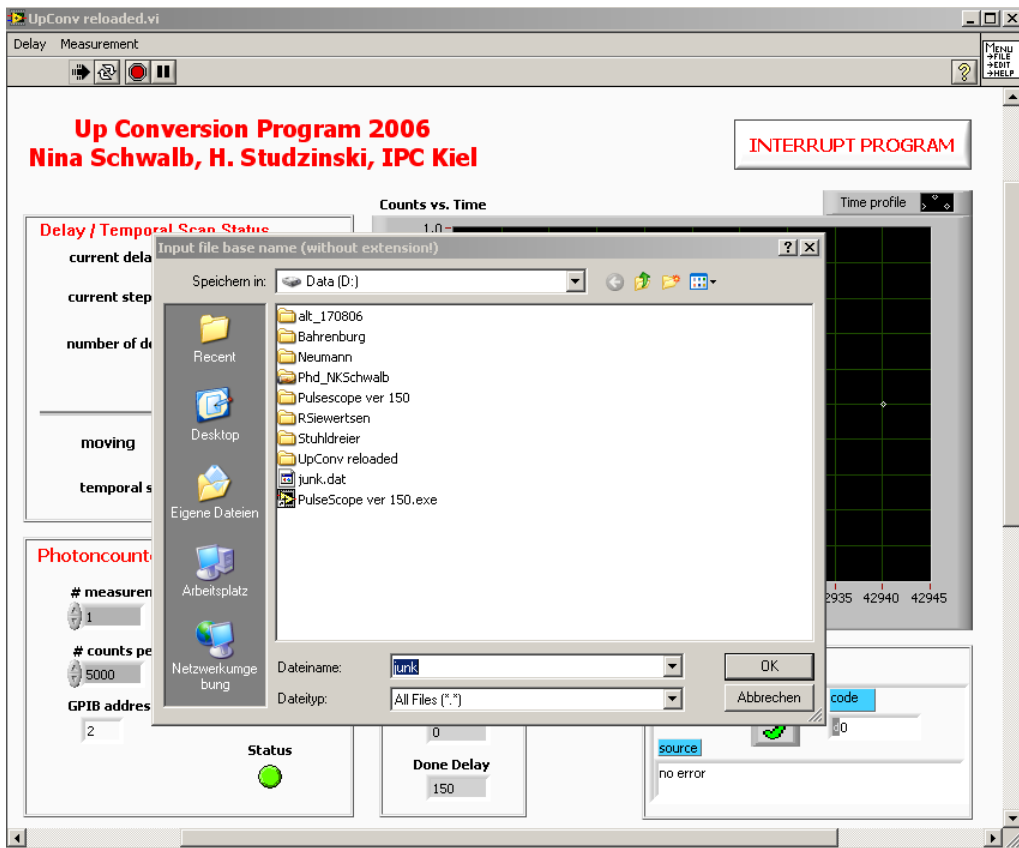


Fig. D.5: Save Data Procedure: When the measurement has finished the *Save Data Dialog* shows up. The default file name is 'junk'; the default file path is 'Data(D:)'. The file is saved in ASCII format. The file extension is automatically set to '.dat'. An email is sent to the operator, after a measurement has finished.

D.2 Kerr Gate Program

D.2.1 Main Front Panel

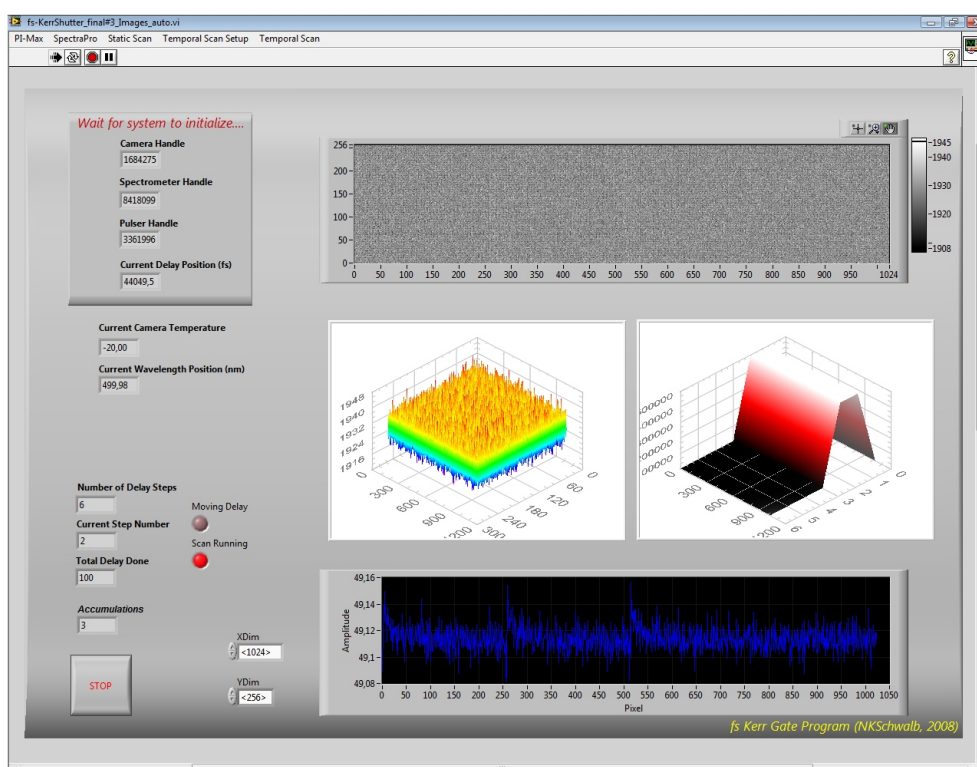


Fig. D.6: Main Front panel of the Kerr Gate Program. Once the program has been started, the operator has to wait for the system to initialize. It is completed, when numbers are displayed in the 'Handle section' on the left. The displays on the left of the front panel are indicators and the corresponding parameters have to be set in the runtime menu. The upper graph on the right of the front panel gives the 2D image of the 256×1024 CCD chip. The white scale denotes high intensity. The middle left graph displays the image in 3D. The bottom graph shows the camera spectrum, i.e., the binning of the ICCD image to a 1×1024 data array. The middle right graph is a 3D plot of the 1×1024 data array at each delay step in the temporal scan. It builds up online and finally gives the full transient spectra of the Kerr-gated sample spectrum (see 11.5).

D.2.2 Runtime Menu ‘PI-Max’

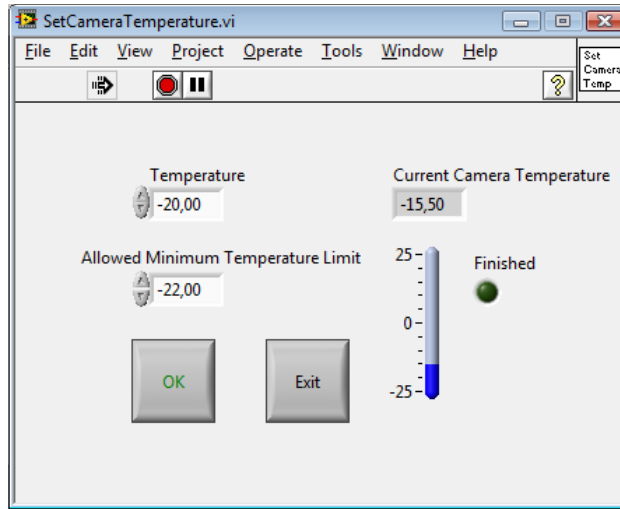


Fig. D.7: Runtime Menu ‘PI-Max’ *Set Camera Temperature*: Here, the camera temperature is set. A variance of $\pm 2^\circ\text{C}$ is allowed, which is a preset level on the camera mainboard. After the desired temperature is reached, the panel closes and passes the temperature value to the front panel.

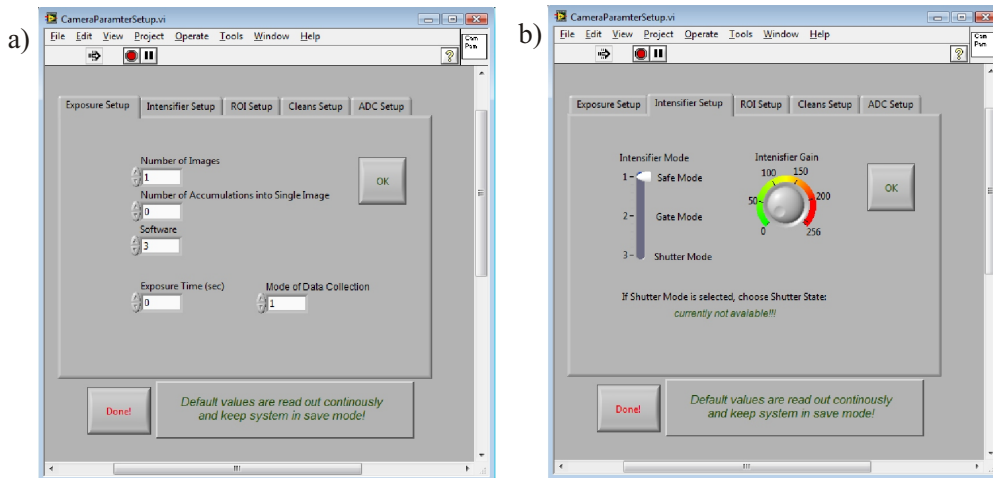
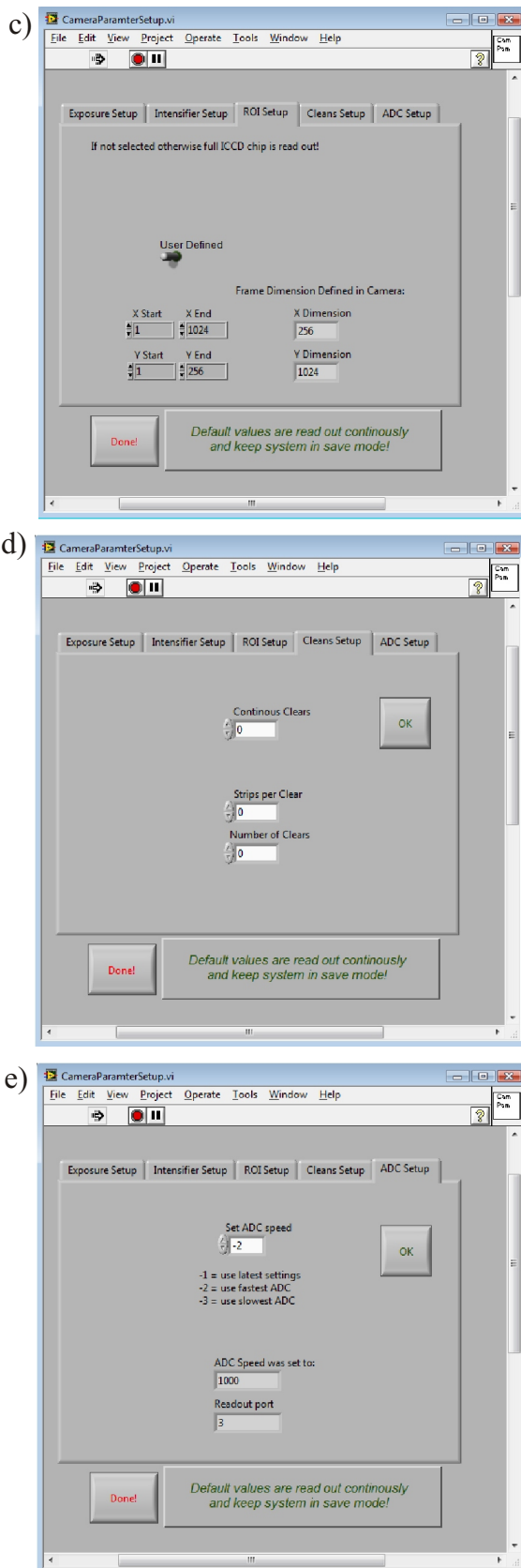


Fig. D.8: Runtime Menu ‘PI-Max’ *Set Camera Parameters*: All relevant experimental parameters of the ICCD camera are set in this menu: **a) Exposure Time Setup**: Settings for the *Number of Images* and *Accumulations* directly on the CCD chip or in the software; *Exposure time* \equiv number of accumulated laser shots per image; *Mode of Data Collection*: 1. Synchronous Focus Mode (Testing Mode): The camera is as fast as possible, but only the latest frame is used when LabView is ready to accept new data; 2. Synchronous NFrame Mode: The camera is as fast as possible and every frame is used (LabView has to keep up, otherwise an error occurs); 3. Asynchronous Mode: The camera takes pictures only when the system is ready to accept, i.e., when it is triggered by an (external) source. This mode was used in all experiments. **b) Intensifier Setup**: 1. Safe Mode: The photocathode is always off; 2. Gate Mode: The photocathode is controlled by a pulse generator; 3. Shutter Mode: The photocathode is on for the set exposure time and off during the readout; *Intensifier Gain*: The sensitivity of the intensifier can be enhanced from 1 – 80 counts per photoelectron (the range is in arbitrary units from 0 – 255).



Left Fig. D.9: Runtime Menu 'PI-Max' *Set Camera Parameters:* *c) Region of Interest (ROI) Setup:* If not chosen otherwise, the full 256×1024 pixel-sized CCD chip is read out. A user-defined readout of the x- and y-dimension can be set. Note that although only a user-defined part of the chip is used, the full chip is illuminated and can be damaged by too high light intensities. *d) Cleans Setup:* Clearing of charge from the CCD chip: *Continuous Clears:* Number of strips to clear continuously before looking if an external trigger has arrived (used in all experiments); *Strips per Clear* and *Number of Clears:* If not clearing continuously (i.e., if not working with external triggering), this defines the number of cleared strips and repeats of clears of the CCD chip. *d) ADC Setup:* It can be chosen between two A/D converts (16 bit) with 1 kHz or 1 MHz readout rate. Note that the faster converter gives a higher readout noise. The panel can be exit via 'Done'.

D.2.3 Runtime Menu ‘SpectraPro’

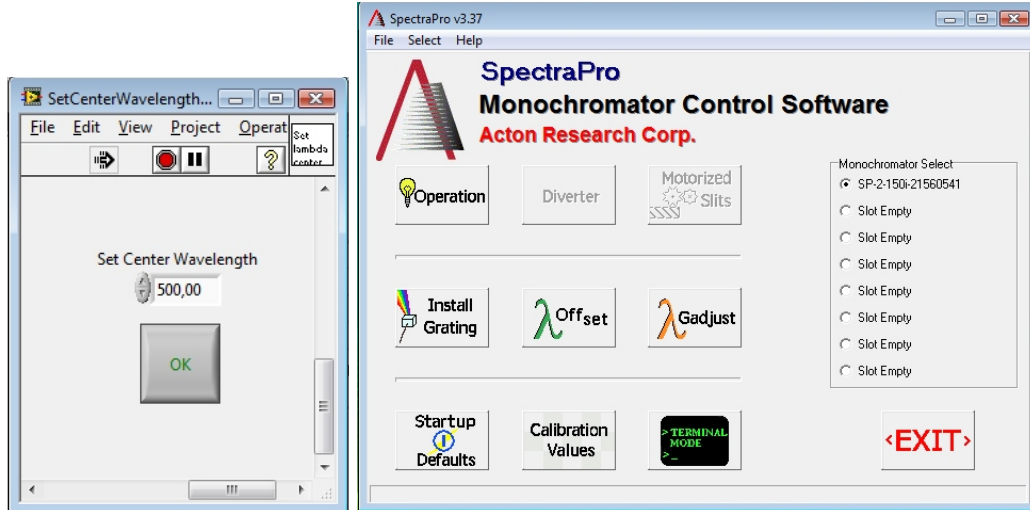


Fig. D.10: Runtime Menu ‘SpectraPro’: *Set Center Wavelength*: Allows to set the center wavelength of the Acton SpectraPro monochromator. To install and adjust new gratings, one has to use the SpectraPro software (right graph).

D.2.4 Runtime Menu ‘Static Scan’

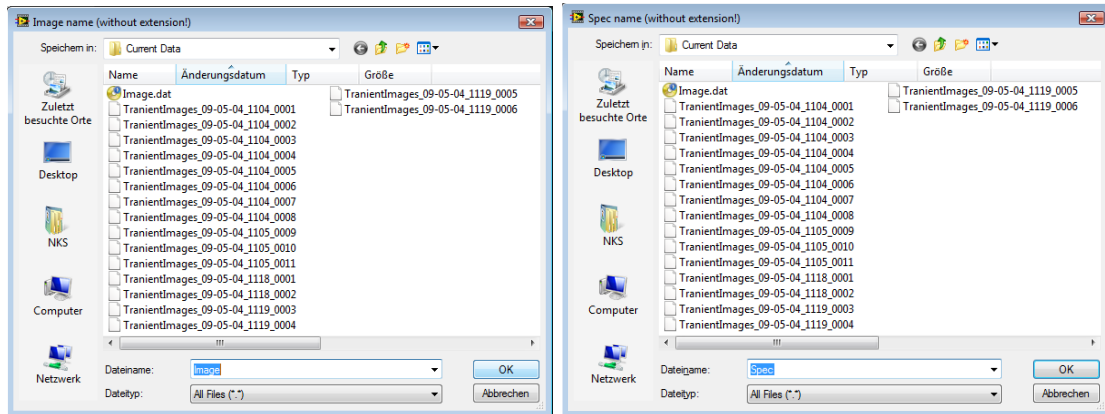


Fig. D.11: Runtime Menu ‘Static Scan’: *Start Static Scan*: This submenu starts a static scan. The collected images are displayed in the upper and middle left graph on the main front panel, the collected spectrum is shown in the bottom graph. After the measurement has been finished, a *Save Data Dialog* shows up. The default path is ‘E:\ Current Data’. The file is saved in ASCII format. First, the collected image is saved (default file name ‘Image’) and afterwards the operator is asked to save the spectrum (default file name ‘Spec’). The file extension is automatically set to ‘.dat’.

D.2.5 Runtime Menu ‘Temporal Scan Setup’

This menu includes the three important submenus ‘Set Temporal Scan Profile’, ‘Move Relative’ and ‘Move Absolute’.

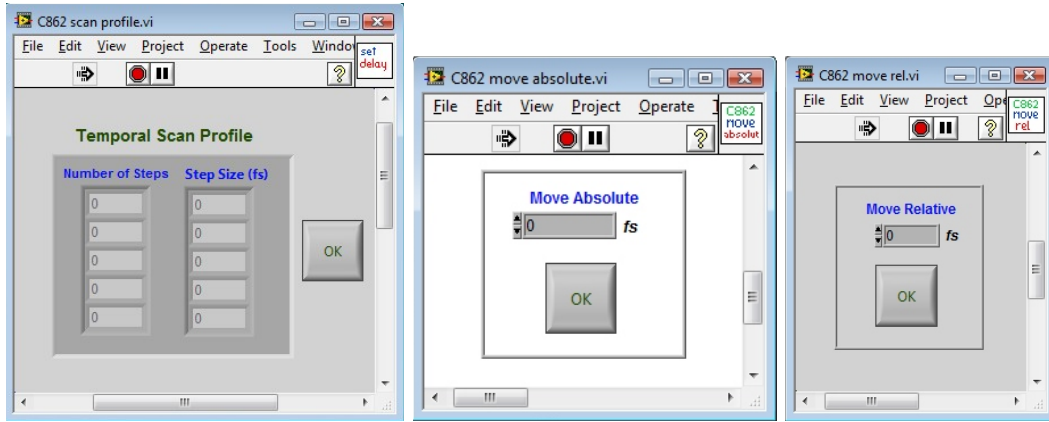


Fig. D.12: Runtime Menu ‘Temporal Scan Setup’. The main parameters to set are: (i) *Set Temporal Scan Profile*, which includes the number of steps and their size in femtoseconds. Up to five different delay sizes can be chosen; (ii) *Move Absolute*, which moves the delay stage to the desired delay position in femtoseconds; (iii) *Move Relative*, which moves the delay stage relative to the current position in femtoseconds.

D.2.6 Runtime Menu ‘Temporal Scan’

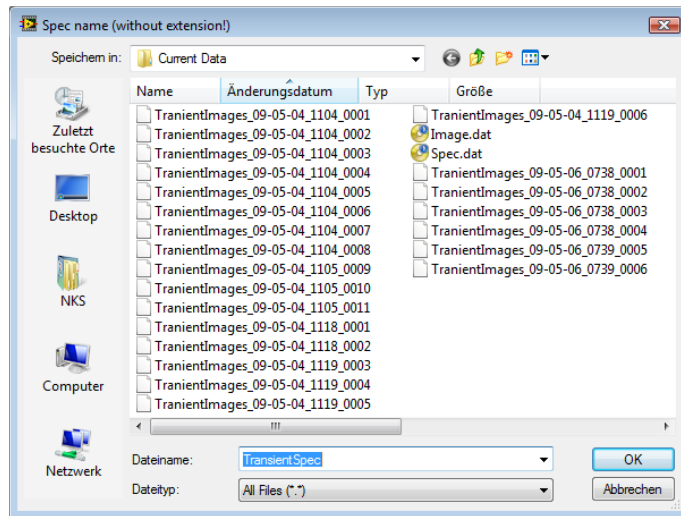


Fig. D.13: Runtime Menu ‘Temporal Scan’: *Start Temporal Scan*: This submenu starts a temporal scan. The collected images and spectra of the current delay step are displayed in the upper, middle left and bottom graph. The CCD images at each particular delay step are saved automatically in the ‘E:\ Current Data’ directory, including the image number (number of the current delay step), date and time in the file name. The middle right 3D graph on the main front panel summarized the transient spectra of each delay step. After the measurement has been finished, a *Save Data Dialog* shows up. The default path is ‘E:\ Current Data’. The file is saved in ASCII format and the file extension is automatically set to ‘.dat’. The data sheet is in matrix format: first row = delay steps; first column = CCD pixels (\equiv wavelength); all other entries = measured intensities. An email is sent to the operator, after a measurement has finished.

D.2.7 Shut-Down Procedure and Important Notes

Before quitting LabView, the system has to be shut down by pressing the stop button on the main front panel. This starts the shut down procedure for the camera, the camera controller and the delay stage. Before shutting down the computer, the MCP and then the camera/controller system have to be turned off. The same ordering is recommended for the start up procedure. Note that the MCP should be turned off, when it is not used in the experiment for a longer period. Finally, for measurements in the UV, you have to keep in mind that light leakage through the photocathode to the UV-sensitive MCP can occur. Further technical details and pdf manuals on the camera/controller system and the spectrometer can be found at <http://www.roperscientific.de/> and <ftp://www.roperscientific.com/>.

References and Notes

- [1] C. E. Crespo-Hernández, B. Cohen, P. M. Hare, B. Kohler, *Chem. Rev.* **104**, 1977 (2004).
- [2] V. A. Bloomfield, D. M. Crothers, I. Tinoco, *Nucleic Acids: Structures, Properties and Functions* (University Science Books, Sausalito, 2000).
- [3] C. R. Cantor, M. M. Warshaw, H. Shapiro, *Biopolymers* **9**, 1059 (1970).
- [4] M. M. Warshaw, C. R. Cantor, *Biopolymers* **9**, 1079 (1970).
- [5] T. Michalak, N. K. Schwalb, J. Gripp, F. Temps, *Spectrochim. Acta A* (submitted, 2009).
- [6] N. K. Schwalb, F. Temps, *J. Phys. Chem. A*, *submitted* (2009).
- [7] T. Michalak, N. K. Schwalb, J. Gripp, F. Temps, *manuscript in preparation* (2009).
- [8] P. Carmona, M. Molina, A. Lasagabaster, R. Excobar, A. B. Altabef, *J. Phys. Chem.* **97**, 9519 (1993).
- [9] N. K. Schwalb, F. Temps, *J. Am. Chem. Soc.* **129**, 9272 (2007).
- [10] S. Perun, A. Sobolewski, W. Domcke, *J. Phys. Chem. A* **110**, 9031 (2006).
- [11] L. Biemann, T. Häber, D. Maydt, K. Schaper, K. Kleinermanns, *J. Chem. Phys.* **128**, 195103 (2008).
- [12] T. Michalak, *Characterization of Cytisine and H-bonded Cytidine Dimers in Solution by FTIR Spectroscopy and Quantum Chemical Calculations* (Diploma Thesis, Christian-Albrechts-University, 2007).
- [13] C. Canuel *et al.*, *J. Chem. Phys.* **122**, 074316 (2005).
- [14] A. L. Sobolewski, W. Domcke, *Phys. Chem. Chem. Phys.* **6**, 2763 (2004).
- [15] A. L. Sobolewski, W. Domcke, C. Hättig, *Proc. Nat. Acad. Sci. USA* **102**, 17903 (2005).
- [16] A. Abo-Riziq *et al.*, *Proc. Nat. Acad. Sci. USA* **10**, 20 (2005).
- [17] S. K. Pal, J. Peon, A. H. Zewail, *Chem. Phys. Lett.* **363**, 57 (2002).

Danksagung

- An erster Stelle möchte ich meinem Doktorvater Herrn Prof. Dr. F. Temps für seine unermüdliche Unterstützung und Begleitung meiner Arbeit danken. Sein Engagement, seine Motivation und explizit die Schaffung eines hervorragenden Forschungsumfelds haben wesentlich zum Gelingen dieser Arbeit beigetragen. Ich hatte die Möglichkeit auf einem noch relativ jungen, spannenden und momentan intensiv erforschten Gebiet tätig sein zu dürfen. Meine Forschungsergebnisse konnte ich auf diversen nationalen und darüberhinaus auch auf internationaler Ebene präsentieren und in einschlägigen Fachjournals publizieren.
- Ganz besonders danke ich meinem F3-Praktikanten und Diplomanden Th. Michalak, der durch theoretischen Untersuchungen und statische FTIR-Experimente einen wesentlichen Beitrag zur Erforschung der Wasserstoffbrücken-gebundenen Basenpaare geleistet hat und geholfen hat, den enormen Syntheseaufwands bezüglich der untersuchten Nukleosid-Derivate zu reduzieren. In diesem Zusammenhang gilt mein Dank ebenso sehr Dr. J. Gripp, H.-M. Behrends und H. Neumann. Ebenso danke ich für die Mitarbeit von A. Westphal, Chr. Freudenhammer und R. Siewertsen als HiWis bzw. F3-Praktikanten, die an der Startphase dieses Projekts beteiligt waren.
- Außerdem gilt mein Dank J. Kleber, der ebenfalls über seine Diplomarbeit zum Grundlagenwissen über statische Fluoreszenzspektren von DNA Bausteinen beigetragen hat.
- Dr. H. Studzinski und Dr. K. Lass danke ich für geduldige Unterstützung meiner ersten Schritte in LabView.
- Dem gesamten derzeitigen und ehemaligen AK Temps danke ich für die schöne Zeit, den freundlichen Umgang und die gemeinsame 'Bewältigung des täglichen Wahnsinns'. Insbesondere danke ich allen Tippfehler-Suchenden (da dies mein ganz persönlicher Wahnsinn ist): Dr. H. Studzinski, Dr. S. Dziarzhyski, Dr. Th. Pancur, M. Stuhldreier, K. Röttger, J. Bahrenburg, J. Kleber.
- Für elektronisch/technischen Support danke ich dem Werkstatt-Team, K. Warns und U. Eggers, sowie Frau v. d. Heydt für die Hilfe bei allen organisatorischen Fragen.
- Der DFG danke ich für die finanzielle Unterstützung.

Curriculum Vitae

Nina Schwalb
Diplom-Chemiker

Dahlienweg 4a
48565 Steinfurt
Germany

Tel.: +49 431-880 2833 (office)
+491785515482

E-Mail: schwalb@phc.uni-kiel.de (office)
ninaschwalb@gmx.de

birth date 15.04.1982

birth place Steinfurt

Doctorate Studies

06/2009 Final PhD examination (thesis defence).

since 12/2005 **PhD student** in the group of Prof. Dr. F. Temps at the Institute of Physical Chemistry of Christian-Albrechts-University Kiel.

Thesis title: "Ultrafast Electronic Deactivation Dynamics in DNA Model Systems by Femtosecond UV Fluorescence Spectroscopy".

Collaborations:

since 2006 "Femtosecond IR Spectroscopy on Hydrogen-Bonded DNA Base Pairs" *Max-Born Institut für Nichtlineare Optik und Kurzzeitspektroskopie, Berlin* (Prof. Dr. Th. Elsaesser).

since 2007 "Femtosecond Time-resolved Fluorescence Spectroscopy on Antioxidants in Emulsions and Micellar Systems" *Institut für Lebensmitteltechnologie der Agrar- und Ernährungswissenschaftlichen Fakultät an der Christian-Albrechts-Universität zu Kiel* (Prof. Dr. K. Schwarz).

Education

11/2005 Final degree (Diplom-Chemiker), grade: **1.1**

Diploma student in physical chemistry in the group of Prof. Dr. F. Temps, University Kiel

Thesis title: „Zeitaufgelöste Femtosekunden-Fluoreszenzspektroskopie an N⁶,N⁶-Dimethyladenin“.

04/2005 – 07/2005	Student research assistant in the group of Prof. Dr. F. Temps: “Restructuring of the femtosecond laser lab and re-assembly of the fluorescence up-conversion experiment.”
10/2003 – 04/2005	Graduate student of chemistry at the University of Kiel, advanced studies in: <ul style="list-style-type: none"> • Physical Chemistry • Organic Chemistry of Carbohydrates
10/2003	Intermediate diploma in chemistry, grade: 1.0 .
10/2001 – 10/2003	Undergraduate student of chemistry at the University of Kiel.
06/2001	Abitur (university-entrance diploma), grade: 1.6
1992 – 2001	Gymnasium Arnoldinum Steinfurt (grammar school)
1988 – 1992	Graf-Ludwig-Grundschule Steinfurt (elementary school)

Awards & Grants

10/2008	Poster prize at <i>International Workshop on Ultrafast Chemical Physics</i> , Glasgow, Scotland.
08/2007	ACS Outstanding Student Poster Award, <i>234th ACS National Meeting, Boston MA, USA</i>
06/2007	PCCP poster prize, <i>Femtochemistry & Femtobiology 8, Oxford, GB</i> .
12/2006	Otto-Diels-Preis for best diploma 2005-2006, <i>GDCh Ortverband Kiel</i>
03/2004	Scholarship of the Dr. W. Hunke-Stiftung of the University of Kiel.

Teaching

since 12/2005	Mentoring/supervision of diploma and PhD students. Teaching assistant in lab courses for graduate students: Basic and Advanced Spectroscopy & Kinetics. Tutor for lectures in physical chemistry: Thermodynamics and Electrochemistry, Quantum Mechanics and Quantum Chemistry, Modern Spectroscopy.
10/2003 – 12/2005	Student teaching assistant in physical chemistry: lab courses for biologists, physicists and pharmacists.

Memberships

Deutschen Bunsen-Gesellschaft für Physikalische Chemie (DBG)
Gesellschaft Deutscher Chemiker (GDCh)
Jungchemikerforum (JCF) der GDCh

Other activities

Referee for the Journal of the American Chemical Society
Member of the committee for the appointment of professorship in physical and theoretical chemistry

Languages

English
French (basics)
Latin

Computer Skills

Programming Languages:

LabView, Fortran (basics)

Programs:

Mathematica, Origin, MS-Office, CorelDraw, ChemOffice, Latex,
Gaussian und Turbomole (basics)

Publications

Schwalb, Nina K.; Temps, Friedrich E. E.: "On the Structure and Photostability of Cytosine Self-Assemblies with Extended Hydrogen-Bonding Networks", **Journal of Photochemistry & Photobiology** **2009**, submitted.

Schwalb, Nina K.; Temps, Friedrich E. E.: "A Fourier-Transform Infrared, UV Absorption, and Femtosecond Fluorescence Study of the G Tetrad Motif of G-Quadruplex DNA", **Angewandte Chemie** **2009**, submitted.

Schwalb, Nina K.; Temps, Friedrich E. E.: "Ultrashort Excited Electronic State Lifetimes of Hydrogen-Bonded Guanosine and

Cytidine Containing Base Pairs in Solution“, **Journal of Physical Chemistry A** **2009**, submitted.

Michalak, Th., Schwalb, Nina K.; Temps, Friedrich E. E.: “A Combined FTIR and DFT Study of Hydrogen Bonded Complexes of Cytidine and N⁴-Ethylcytidine in Solution”, **Spectrochim Acta** **2009**, submitted.

Schwalb, Nina K.; Temps, Friedrich E. E.: “A Modified Four-State Model for the 'Dual Fluorescence' of N⁶,N⁶-Dimethyladenine derived from Femtosecond Fluorescence Spectroscopy“, **Journal of Physical Chemistry A** **2009**, accepted and in press.

Schwalb, Nina K.; Temps, Friedrich E. E.: “Modified Three-State Model for the 'Dual Fluorescence' of N⁶,N⁶-Dimethyladenine derived from Femtosecond Fluorescence Spectroscopy“, **Springer Series in Chemical Physics** **2008**, in press.

Schwalb, Nina K.; Temps, Friedrich E. E.: “Base sequence and higher-order structure induce the complex excited-state dynamics in DNA“, **Science** **2008**, **322(243)**.

Schwalb, Nina K.; Temps, Friedrich E. E.: “Ultrafast electronic relaxation in guanosine is promoted by hydrogen bonding with cytidine”, **Journal of the American Chemical Society** **2007**, **129(30)**.

Schwalb, Nina K.; Temps, Friedrich E. E.: “A femtosecond time-resolved investigation of dual fluorescence from N⁶,N⁶-dimethyladenine”, **Physical Chemistry Chemical Physics** **2006**, **8(44)**.

Pancur, Thomas; Schwalb, Nina K.; Renth, Falk; Temps, Friedrich E. E.: “Femtosecond fluorescence up-conversion spectroscopy of adenine and adenosine: experimental evidence for the $\pi\sigma^*$ state?”, **Chemical Physics** **2005**, **313(1-3)**.

in preparation:

Schwalb, Nina K.; Kleber, Joscha; Sönnichsen, Frank; Temps, Friedrich E. E.: “Ultrafast electronic Deactivation Dynamics in a Short Selfcomplementary DNA Oligomer Loop“, **Physical Chemistry Chemical Physics** **2009**.

Michalak, Th., Schwalb, Nina K.; Temps, Friedrich E. E.: “A Combined FTIR and DFT Study of Hydrogen-Bonded Guanosine Dimers and the Guanosine-Cytidine Watson-Crick Pair in Solution “.

Posters & Talks

- 2009
Schwalb, Nina K.: "Untersuchung der sequenzabhängigen Photostabilität von DNA-Strängen mittels Femtosekunden-UV-Fluoreszenzspektroskopie", **Bunsentagung**, Köln.
- Schwalb, Nina K.: "Ultrafast Electronic Deactivation Dynamics of DNA Model Systems", **invited talk, Prof. M. Bonn, AMOLF**, Amsterdam.
- Schwalb, Nina K.: "Untersuchung der sequenzabhängigen Photostabilität von DNA-Strängen mittels Femtosekunden-UV-Fluoreszenzspektroskopie", **Bunsentagung**, Köln.
- 2008
Schwalb, Nina K.; Temps, Friedrich E. E.: "The relevance of hydrogen-bonding dynamics in electronically excited DNA base pairs", **International Workshop on Ultrafast Chemical Physics**, Glasgow, Scotland.
- Schwalb, Nina K.; Temps, Friedrich E. E.: "Femtosecond time-resolved fluorescence spectroscopy of N^6,N^6 dimethyladenine: New explanation of the "dual fluorescence" dynamics from decay and rise time measurements at threshold", **Ultrafast Phenomena**, Stresa, Italy.
- Michalak, Th., Schwalb, Nina K.; Temps, Friedrich E. E.: "Characterization of guanosine and cytidine tautomers and their H-bonded dimers in solution by FTIR spectroscopy and quantum chemical calculations" **Bunsentagung** Saarbrücken.
- Michalak, Th., Schwalb, Nina K.; Temps, Friedrich E. E.: "Characterization of guanosine and cytidine tautomers and their H-bonded dimers in solution by FTIR spectroscopy and quantum chemical calculations" **10. Frühjahrssymposium des JungChemikerForums der GDCh** Rostock.
- 2007
Schwalb, Nina K.; Temps, Friedrich E. E.: "Ultrafast non-radiative deactivation dynamics of electronically excited nucleobases: Resolution of the gas vs. solution phase mystery", **234th ACS National Meeting**, Boston MA, USA .
- Schwalb, Nina K.; Temps, Friedrich E. E.: "Complementary hydrogen-bonding promotes ultrafast non-radiative electronic relaxation in DNA building blocks", **invited talk, Prof. Bern E. Kohler, Department of Chemistry, Ohio State University**, Columbus, OH, USA.
- Schwalb, Nina K.; Temps, Friedrich E. E.: "Hydrogen bonding promotes ultrafast non-radiative electronic relaxation in DNA building blocks", **Femtochemistry and Femtobiology 8**, Oxford, UK.
- Schwalb, Nina K.; Temps, Friedrich E. E.: "Femtosekunden Fluoreszenzspektroskopie an Wasserstoffbrücken-gebundenen Nucleobasen und kurzen selbst-komplementären DNA-Oligonukleotiden", **Bunsentagung** Graz, Austria.

2006

Schwalb, Nina K.; Temps, Friedrich E. E.: "Femtosecond time-resolved fluorescence spectroscopy on modified nucleobases"; invited talk, **Prof. J. Wachtveitl, Institut für Physikalische und Theoretische Chemie/Biophysik Universität Frankfurt.**

Schwalb, Nina K.; Temps, Friedrich E. E.: "Femtosekundenzeitaufgelöste Fluoreszenzspektroskopie an modifizierten Nucleobasen"; Im Rahmen der Preisverleihung für das beste Diplom 2005-2006, **GDCh Weihnachtsskolloquium Ortsverbands Kiel.**

Schwalb, Nina K.; Temps, Friedrich E. E.: "Femtosecond time-resolved fluorescence up-conversion measurements on nucleobase derivatives and H-bonded nucleoside dimers"; **Tulip Summer School III: "Modern Developments in Spectroscopy"**, Noordwijk, The Netherlands.

Schwalb, Nina K.; Temps, Friedrich E. E.: "Femtosekundenzeitaufgelöste Fluoreszenzspektroskopie von DNA-Basenderivaten und ihren Wasserstoffbrücken-gebundenen Dimeren"; **Bunsentagung Erlangen.**

Schwalb, Nina K.; Temps, Friedrich E. E.: "Femtosecond fluorescence up-conversion spectroscopy of DNA building blocks"; **SFB Begutachtung, Kiel.**

2005

Schwalb, Nina K.; Pancur, Th.; Temps, Friedrich E. E.: "Femtosecond time-resolved fluorescence decay profiles of adenine und N^6, N^6 -dimethyladenine"; **Bunsen Discussion Meeting, Göttingen.**

Workshops

Workshop des ISH-Themennetzwerks Biowirkstoffe: „New methods for the analysis of ROS and bioactive compounds“; **Tagungszentrum Salzau 2007.**

SFG-Workshop: *Summenfrequenz-Spektroskopie (SFG) als Messverfahren zur Analyse von Oberflächen und Grenzflächen*“; MPI für Kolloid- und Grenzflächenforschung, **Golm 2007.**

APE Praxis-Workshop: „Messung ultrakurzer Laserpulse“, APE Angewandte Physik & Elektronik GmbH, **Berlin 2006.**

The Lindau Nobel Laureate Meeting, **Lindau 2005.**

Kiel, 05/13/2009

King Schwett

